GEORG-AUGUST-UNIVERSITÄT
GÖTTINGEN

Fakultät für
Physik

Master's Thesis

Messung des Top-Quark-Paarproduktionswirkungsquerschnittes im Lepton + Jets Kanal am ATLAS Experiment bei $\sqrt{s} = 13$ TeV

Measurement of the top quark pair production cross section in the lepton + jets channel at the ATLAS experiment at $\sqrt{s} = 13$ TeV

prepared by

Kevin Moor

from Northeim

at the II. Physikalisches Institut

Thesis number:	II.Physik-UniGö-MSc-2019/02
Thesis period:	2nd April 2019 until 9th October 2019
First referee:	Prof. Dr. Arnulf Quadt
Second referee:	Prof. Dr. Ariane Frey

Zusammenfassung

Diese Arbeit stellt eine Messung des Wirkungsquerschnitts für die Produktion von Top-Quark-Paaren ($t\bar{t}$) im Lepton+Jets Kanal vor. Die Messung basiert auf Daten von Proton-Proton-Kollisionen bei einer Schwerpunktsenergie von $\sqrt{s} = 13$ TeV, die mit dem ATLAS-Detektor am LHC aufgenommen worden. Der volle Datensatz des „Run II“ (2015-2018), welcher einer integrierten Luminosität von $L_{\text{int}} = 139$ fb^{-1} entspricht, wird für die Analyse verwendet. Ereignisse mit genau einem Elektron oder Myon, mindestens vier Jets und entweder einem oder zwei b-tags werden ausgewählt und anschließend in drei disjunkte Signalregionen unterteilt. In jeder Region wird eine Variable ausgewählt, die eine geringe Sensitivität bezüglich Modellierungsunsicherheiten hat und gleichzeitig Trennung von Untergrundquellen ermöglicht. Um systematische Unsicherheiten zu beschränken, werden die Verteilungen dieser Variablen in einem Profile-Likelihood-Fit genutzt. Unter der Voraussetzung einer Top-Quark-Masse von $m_t = 172,5$ GeV wird mit einer Präzision von 4,3% ein gesamter Wirkungsquerschnitt von $\sigma_{\text{inc}}(t\bar{t}) = 829,7^{+35,3}_{-34,5}$ pb gemessen. Das Ergebnis stimmt sehr gut mit der Vorhersage des Standardmodells in nächst-zu-nächstführender Ordnung der QCD überein. Die gesamte Unsicherheit wird von systematischen Unsicherheiten (vor allem bezüglich der Modellierung) dominiert, wobei die statistische Unsicherheit 0,05% beträgt. Zusätzlich wird der Wirkungsquerschnitt in einem eingeschränkten („fiducial“) Phasenraum gemessen, der so definiert wird, dass er dem Phasenraum der ausgewählten Daten ähnlich ist und somit der experimentellen Akzeptanz entspricht. Das Ergebnis ist $\sigma_{\text{fid}}(t\bar{t}) = 110,5^{+4,3}_{-4,2}$ pb, was einer relativen Unsicherheit von 3,9% entspricht.

Abstract

This thesis presents a measurement of the top-quark pair production cross section in the lepton+jets channel using proton-proton collision data at a centre-of-mass energy of $\sqrt{s} = 13$ TeV recorded with the ATLAS detector at the LHC. The full Run II dataset (2015-2018), which corresponds to an integrated luminosity of $L_{\text{int}} = 139$ fb^{-1}, is analysed. Events with exactly one electron or muon, at least four jets, and either one or two b-tags are selected and subsequently grouped into three disjoint signal regions. In each region a suitable variable is chosen that has small sensitivity to modelling uncertainties and at the same time provides separation from background sources. In order to constrain systematic uncertainties, the distributions of the selected variables are exploited in a profile likelihood fit. Under the assumption of a top-quark mass of $m_t = 172.5$ GeV, the inclusive $t\bar{t}$ cross section is measured with a precision of 4.3% to be $\sigma_{\text{inc}}(t\bar{t}) = 829.7^{+35.3}_{-34.5}$ pb. The result is in very good agreement with the Standard Model prediction at next-to-next-to-leading order in QCD. The total uncertainty is dominated by systematic uncertainties, especially by those related to modelling, whereas the statistical uncertainty is determined to be 0.05%. In addition, the cross section is measured in a restricted (fiducial) phase space which is defined in such a way that it is close to that of the selected data and thus matches the experimental acceptance. The result is $\sigma_{\text{fid}}(t\bar{t}) = 110.5^{+4.3}_{-4.2}$ pb, corresponding to a relative uncertainty of 3.9%.

Contents

1. Introduction

During the last century, several elementary particles and corresponding interactions were observed, and thus a set of theories was developed for their description. Finally, this resulted in the so-called Standard Model (SM) of particle physics which combines the theory of electromagnetic and weak interaction, developed by Glashow, Weinberg, and Salam [1–4], with quantum chromodynamics (QCD), the theory of strong interaction between quarks and gluons [5–7]. Up to now, its predictive power was confirmed in several experiments, e.g. at the Large Electron Positron Collider (LEP), at the TEVATRON, and at the Large Hadron Collider (LHC). One of the most prominent predictions is the existence of the Higgs boson [8–10] which was discovered in 2012 in the ATLAS and the CMS experiment [11, 12]. However, the SM is not the final theory and has its limitations. One example is the missing description of the gravitational force and of dark matter. Besides that, neutrinos are described as massless in the SM which is not compatible with the observed neutrino flavour oscillations [13–15].

One very interesting particle in the SM is the top quark, which was discovered in 1995 in the DØ and the CDF experiment [16, 17]. The large mass, which is responsible for the very short lifetime, makes it very special compared to other quarks. As the only quark in the SM, it decays before forming bound states, which allows direct access to its properties via the decay products. Under laboratory conditions, top quarks are currently only produced in proton-proton collisions at the LHC. There, they are predominantly produced in pairs via the strong interaction. The measurement of the production cross section of top-quark pairs provides an essential test of higher order QCD calculation techniques. In addition, it allows to test several SM predictions related to the spin, the strong coupling to gluons, and the dependence of the cross section on the centre-of-mass energy. A precise measurement also allows to get sensitivity to the top-quark mass because the predicted cross section depends on it. Depending on the analysed final state, one also may be sensitive to contributions from particles beyond the Standard Model (BSM).

This thesis presents a first measurement of the inclusive and fiducial top-quark pair production cross section in the lepton+jets channel at $\sqrt{s} = 13$ TeV using the full ATLAS Run II dataset. Events with exactly one lepton (electron or muon), missing transverse

energy, and at least four jets with either one or two b-tags are analysed. Because of the large amount of recorded data, systematic uncertainties will limit the precision of the measurement. Therefore, a profile likelihood technique is utilised in order to extract the cross section and to constrain the uncertainties. Three orthogonal signal regions are defined and suitable variables are selected whose distributions are finally fitted simultaneously.

First, an introduction to the theoretical foundations of the SM is given in Chapter 2. The particle content and the fundamental interactions between them will be explained. A further focus will be on the properties of the top quark and an overview of previous cross section measurements will be given. Then, a short overview about the LHC and the ATLAS detector will be provided in Chapter 3. The used object definitions and the event selection will be described in Chapter 4. In addition, the signal and background estimation, needed for the measurement, will be detailed. The analysis strategy, especially the variable selection and the profile likelihood technique, will be outlined in Chapter 5. All systematic uncertainties that are considered in the measurement are summarised and explained in Chapter 6. Finally, the results for the inclusive and fiducial cross section are presented in Chapter 7, which is followed by a summary and an outlook in Chapter 8.

2. Theoretical Background

This chapter will present the main aspects of the Standard Model of particle physics[1]. The top quark will be described in more detail in Section 2.5, including its properties, production, and decay. Furthermore, an overview of previous $t\bar{t}$ production cross section measurements will be given.

2.1. Elementary Particles

The Standard Model of particle physics contains the entire knowledge of elementary particles and describes the fundamental interactions (electromagnetic, weak, and strong interaction) between them via quantum field theories. Gravitation (i.e. quantum gravity) is not included but is expected to become relevant only at very high energy scales. All particles are divided into two groups: fermions (half-integer spin) and bosons (integer spin). An overview of SM particles and their main properties is given in Figure 2.1. Fermions are further divided into quarks and leptons which are both grouped into three generations. The three lepton generations consist of the electron (e), the muon (μ), the tau lepton (τ), and their corresponding neutrinos (ν_e, ν_μ, and ν_τ). The neutrinos have no electric charge while the other leptons carry an electric charge of -1 (in units of the elementary charge). The three quark families consist of the up (u), the down (d), the charm (c), the strange (s), the top (t), and the bottom quark (b). The up-type quarks carry an electric charge of $+2/3$ and the down-type quarks a charge of -1/3. Fermions across the three generations have the same quantum numbers (e.g. electric charge, weak isospin) but differ in mass. Fermions in the first generation have the lowest while fermions in the third generation have the largest masses. Neutrinos are massless in the SM although recent experiments have shown that they have a (small) mass [13–15]. Up to now, only upper limits on the masses have been settled [19, 20]. For each particle there is an antiparticle which has opposite charges and handedness but is equal regarding the other particle properties. Fermions are the constituents of matter while stable matter is always built by fermions of the first generation. Due to the higher mass, fermions of the higher generations can

[1]This chapter is based on the MSc interim report.

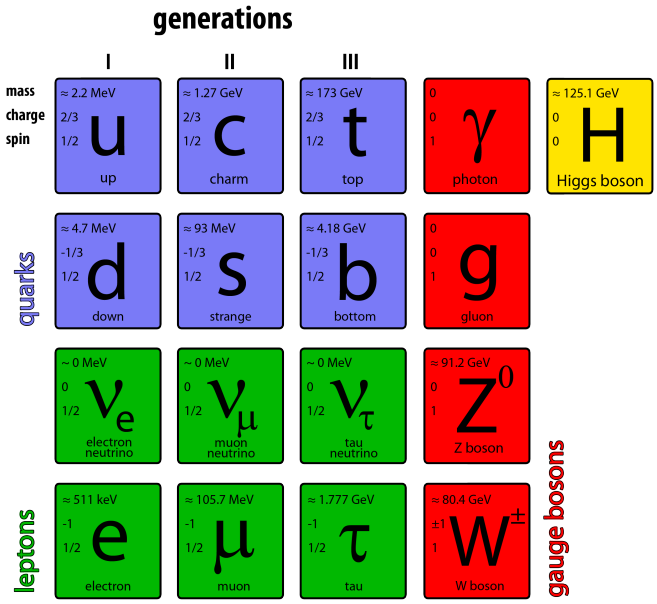

Figure 2.1.: Overview of all particles in the SM and their main properties. Mass values are taken from Ref. [18].

decay into fermions of lower generation. The second main group of elementary particles in the SM is formed by bosons, which have an integer spin. There is the photon (γ), the Z boson, the $W^{\pm}$ bosons, the gluons (g), and the Higgs boson (H). Apart from the Higgs boson (spin 0), all the other bosons (spin 1) are called gauge bosons and are the mediators of the fundamental interactions between particles. The photon is a massless boson and mediates the electromagnetic (EM) interaction. It couples to all particles which carry electric charge. Therefore, it can couple to charged leptons, quarks, but also to W bosons. Because the photon itself carries no electric charge, self-couplings do not exist. The gluon is also massless but mediates the strong interaction. Analogous to the EM interaction, the gluon couples to particles which carry so-called colour charge. There are three different colour charges: red, green, and blue. Additionally, there are also three anticolours (for antiparticles). Gluons themselves carry a combination of a colour and an anticolour charge and therefore they can couple to each other. There are only eight gluons in total because one of the nine colour combinations results in a non-existing colour singlet state. The only other particles which carry colour charge are the quarks. This is also the main difference between quarks and leptons: Leptons can only interact via the electromagnetic (apart from neutrinos) or the weak interaction while quarks can additionally interact via the strong interaction. The W and Z bosons are mediators of the weak force and are quite massive ($m_W = 80.379 \pm 0.012$ GeV, $m_Z = 91.1876 \pm 0.0021$ GeV [18]), in contrast to the other gauge bosons. All fermions can participate in the weak interaction. The

Higgs boson has, in contrast to the gauge bosons, a spin of 0. It carries no electric charge and is also massive ($m_H = 125.10 \pm 0.14$ GeV [18]). It does not mediate fundamental interactions but was introduced into the SM to explain the fact that W and Z bosons, but also fermions (via the so-called Yukawa coupling), are massive. The corresponding mechanism is called the Brout-Englert-Higgs mechanism and explains massive gauge bosons via electroweak symmetry breaking [8–10].

2.2. Local Gauge Invariance

The relativistic equation that describes the dynamics of a free spin 1/2 particle with mass m is the Dirac equation

$$i\gamma^\mu \partial_\mu \psi - m\psi = 0\,, \tag{2.1}$$

where γ^μ are the four-dimensional gamma matrices ($\mu = 0, 1, 2, 3$) and ψ is the spinor (consisting of four components) that describes the spin 1/2 particle. This equation also describes antifermions with the same mass. It can also be derived from the following Lagrangian density (using the Euler-Lagrange equation):

$$\mathscr{L} = i\overline{\psi}\gamma^\mu \partial_\mu \psi - m\overline{\psi}\psi\,, \tag{2.2}$$

where $\overline{\psi} = \psi^\dagger \gamma^0$ is the adjoint spinor. In this Lagrangian a kinetic as well as a mass term can be identified. The SM is a gauge theory which means that the quantum field theories (e.g. quantum electrodynamics (QED), describing the EM interaction) are locally gauge invariant. As an example, QED is based on a U(1) local gauge symmetry. This group describes local transformations of the form $\psi \to \psi' = e^{-iq\lambda(x)}\psi$. If the Lagrangian remains unchanged, a quantum field theory is called locally gauge invariant. To make the Lagrangian in Equation 2.2 gauge invariant, a massless vector field A_μ which couples to the spinor field has to be introduced. This gives the following Lagrangian:

$$\mathscr{L}_{\mathrm{QED}} = i\overline{\psi}\gamma^\mu D_\mu \psi - m\overline{\psi}\psi - \frac{1}{4}F_{\mu\nu}F^{\mu\nu}\,, \tag{2.3}$$

where the interaction $-q\overline{\psi}\gamma^\mu\psi A_\mu$ is contained in the covariant derivative $D_\mu = \partial_\mu + iqA_\mu$. This is the Lagrangian in QED describing the interaction between fermions (with charge q) and massless photons A_μ. The last term is the kinetic term for the gauge field, where $F_{\mu\nu} = \partial_\mu A_\nu - \partial_\nu A_\mu$ is the field strength tensor. Mass terms would spoil the symmetry again and are therefore forbidden. One can see that the existence of (massless) gauge

bosons which interact with fermions is a direct consequence of the insistence on local gauge invariance. In the case of Abelian gauge groups (like U(1)), there are no self-interactions among the gauge bosons. This is different in non-Abelian groups (SU(2) or SU(3)). As an example, quantum chromodynamics (QCD) is based on SU(3) symmetry, and because it is not Abelian, the corresponding gauge bosons (the gluons) can couple to each other.

2.3. Electroweak Unification

The theory of electromagnetic and weak interaction can be unified in the electroweak (EW) theory. This is known as the Glashow-Weinberg-Salam (GWS) model [1–4]. It is also a gauge theory requiring symmetry under local $\mathrm{SU(2)_L} \times \mathrm{U(1)_Y}$ transformations. Here, L refers to left-handed particles and Y refers to the weak hypercharge. The $\mathrm{SU(2)_L}$ is used because W bosons only couple to left-handed particles (and right-handed antiparticles). Therefore, the charged weak interaction is parity violating. To describe the electroweak interaction in a compact way, leptons and quarks are arranged in so-called left-handed weak isospin doublets χ_L. Here, the quantity weak isospin $\vec{T}$ is introduced: Upper components of the doublets have $T_3 = 1/2$, lower components $T_3 = -1/2$.

$$\begin{array}{ll} T_3 = +\frac{1}{2} & \left(\begin{array}{c} \nu_e \\ e^- \end{array} \right)_L, \left(\begin{array}{c} \nu_\mu \\ \mu^- \end{array} \right)_L, \left(\begin{array}{c} \nu_\tau \\ \tau^- \end{array} \right)_L, \left(\begin{array}{c} u \\ d' \end{array} \right)_L, \left(\begin{array}{c} c \\ s' \end{array} \right)_L, \left(\begin{array}{c} t \\ b' \end{array} \right)_L \\ T_3 = -\frac{1}{2} & \end{array}$$

W bosons do not couple to right-handed particles. Therefore, they get a weak isospin of zero and are arranged in right-handed singlets χ_R. The down-type quarks are marked ($'$) to emphasise that these are not the mass but the weak eigenstates. As an example, an up quark can couple to a down quark but also to a strange quark. This is due to the fact that the weak eigenstates are a mixture of quark mass eigenstates, which is described by the CKM matrix as follows [21, 22]:

$$\left(\begin{array}{c} d' \\ s' \\ b' \end{array} \right) = \left(\begin{array}{ccc} V_{ud} & V_{us} & V_{ub} \\ V_{cd} & V_{cs} & V_{cb} \\ V_{td} & V_{ts} & V_{tb} \end{array} \right) \left(\begin{array}{c} d \\ s \\ b \end{array} \right) . \tag{2.4}$$

The GWS theory requires local gauge symmetry under $\mathrm{SU(2)_L} \times \mathrm{U(1)_Y}$ transformations. Therefore, in total four gauge fields (representing four gauge bosons) have to be introduced: Three gauge fields W_μ^i for the $\mathrm{SU(2)_L}$ (coupling to T_i) and one gauge field B_μ for the $\mathrm{U(1)_Y}$ group (coupling to $Y = 2(q - T_3)$). The physical gauge bosons are finally

a mixture of these fields. The $W^{\pm}$ bosons can be described as $W^{\pm}_{\mu} = \frac{1}{\sqrt{2}}\left(W^1_{\mu} \mp iW^2_{\mu}\right)$. Due to the Higgs mechanism, the B_{μ} and the W^3_{μ} fields mix together according to

$$A_{\mu} = \quad B_{\mu}\cos\theta_W + W^3_{\mu}\sin\theta_W\,, \tag{2.5}$$

$$Z_{\mu} = -B_{\mu}\sin\theta_W + W^3_{\mu}\cos\theta_W\,, \tag{2.6}$$

where θ_W is called the Weinberg angle, A_{μ} is the massless photon, and Z_{μ} describes the Z boson.

2.4. Quantum Chromodynamics

Quantum chromodynamics is the quantum field theory describing the strong interaction. It is based on local gauge invariance under $\mathrm{SU(3)_C}$ transformations where C refers to the colour of gluons and quarks. The $\mathrm{SU(3)_C}$ has eight generators. Hence, to ensure that the QCD Lagrangian is local gauge invariant, eight gauge fields G^a_{μ} ($a = 1, .., 8$), corresponding to eight gluons, have to be introduced. Starting from the free Dirac Lagrangian for quarks, the QCD Lagrangian is constructed by replacing the space-time derivative by a covariant derivative, and by adding a kinetic term for the gluons:

$$\mathscr{L}_{\mathrm{QCD}} = \sum_f \bar{q}_f(i\gamma^{\mu}D_{\mu} - m_f)q_f - \frac{1}{4}G^a_{\mu\nu}G^{\mu\nu,a}\,. \tag{2.7}$$

Here, $G^a_{\mu\nu} = \partial_{\mu}G^a_{\nu} - \partial_{\nu}G^a_{\mu} - g_s f_{abc}G^b_{\mu}G^c_{\nu}$ and f_{abc} are the structure constants of the $\mathrm{SU(3)_C}$ describing the non-commutativity of the generators. The sum runs over all quark flavours. The covariant derivative is $D_{\mu} = \partial_{\mu} + \frac{ig_s}{2}\lambda_a G^a_{\mu}$, where λ_a are the Gell-Mann matrices (the SU(3) generators) and g_s is the strong coupling parameter. Because of the last term in the Lagrangian, self-interactions (as in the SU(2)) among gluons are possible. Finally, the gauge group of the SM is the combination of all groups: $\mathrm{SU(3)_C} \times \mathrm{SU(2)_L} \times \mathrm{U(1)_Y}$.

In the process of renormalisation, the coupling strength $\alpha = g^2/4\pi$ becomes a function of the energy scale of a process. Due to gluon self-interaction diagrams, the coupling strength of the strong interaction decreases with the energy scale Q^2 [23]:

$$\alpha_s(Q^2) = \frac{\alpha_s(\mu^2)}{1 + \alpha_s(\mu^2)\frac{11N_c - 2N_f}{12\pi}\ln\frac{Q^2}{\mu^2}}\,, \tag{2.8}$$

where $N_{c/f}$ is the number of colours or flavours and μ is an arbitrary scale at which α_s is known. For $N_c = 3$ and $N_f = 6$, α_s increases with smaller energies, i.e. larger distances. Therefore, particles carrying colour charge cannot be observed as free particles.

In QCD, this phenomenon is called colour confinement. For example, when two quarks are produced as a pair and are then separated, the potential energy between both quarks increases with the distance. At some point the energy is high enough to produce a quark-antiquark pair. This process is then iterated and ends with a whole bunch of colourless particles consisting of quarks. Such bound states are called hadrons. Hadrons consisting of a quark-antiquark pair are called mesons, and bound states of three quarks are called baryons. Whenever particles with colour charge are produced (quarks or gluons), one cannot observe them as free particles. Instead, one observes them finally as a bunch of hadrons, a so-called jet, in a particle detector.

2.5. The Top Quark

In 1973, Makoto Kobayashi and Toshihide Maskawa developed a theory [22] to explain the CP violation which had been observed previously in kaon decays. According to their theory, CP violation could only occur with at least three generations of quarks. At that time, only two generations had been known. After the discovery of the bottom quark in 1977 at Fermilab [24], the existence of the top quark as the weak isospin partner was expected, but due to the very high mass it took some time for the discovery. It was finally observed in 1995 at the Tevatron in the DØ and the CDF experiment in $p\bar{p}$ collisions [16, 17]. Today, top quarks are produced in huge numbers at the Lhc (see Section 3.1) allowing precise studies of their properties.

2.5.1. Top-Quark Properties

The top quark is currently the most massive known elementary particle. Its mass was measured in many experiments, especially in the Atlas and the Cms experiment. The world average is $m_t = 173.34 \pm 0.27$ (stat.) ± 0.71 (syst.) GeV [25] (Tevatron and Lhc combination). The high mass makes the top quark very interesting because it is close to the EW scale (246 GeV) and corresponds to a relatively high Yukawa coupling in the order of 1. This indicates that the top quark might play a special role in the electroweak symmetry breaking. Additionally, knowing the mass the SM can predict the decay width of the top quark. For a mass of $m_t = 173.3$ GeV and $\alpha_s(m_Z) = 0.118$, the predicted width at next-to-leading order (NLO) is 1.35 GeV [18, 26]. The Atlas collaboration measured $\Gamma_t = 1.76 \pm 0.33$ (stat.) $^{+0.79}_{-0.68}$ (syst.) GeV [27] at $\sqrt{s} = 8$ TeV, which is in agreement with the SM prediction. The high decay width is equal to a very short lifetime of $\tau = \hbar/\Gamma_t \approx 5 \cdot 10^{-25}$ s. This lifetime is much smaller than the typical hadronisation time $\mathcal{O}(10^{-23}$ s) for heavy quarks [28], which means that the top quark decays before it

forms hadrons. Measuring the decay products, one gets direct access to the properties of the top quark which makes it very special compared to other quarks. The electric charge is predicted by the SM to be +2/3. It was measured by the ATLAS collaboration at 7 TeV to be 0.64±0.02 (stat.)±0.08 (syst.) [29]. At the same time, alternative models predicting heavy quarks with charge -4/3 were excluded at more than 8σ significance level. This measurement was performed indirectly by measuring the charges of the top-quark decay products. The measurement of the production cross section of the $t\bar{t} + \gamma$ process would allow a direct measurement of the top-photon coupling, and thus of the electric charge.

2.5.2. Top-Quark Production

Top quarks can be produced for example in proton-antiproton collisions or in proton-proton collisions. Since top quarks are currently only produced (under laboratory conditions) at the LHC, the production of top quarks in pp collisions will be presented. There, top quarks are mainly produced in pairs ($t\bar{t}$), but also single top quarks can be produced via the electroweak interaction.

Top-Quark Pair Production

At the LHC, top-quark pairs are produced via the strong interaction. Protons, which are collided at the LHC, are not elementary particles. In the most simple static quark model, they are made of three so-called valence quarks: two up and one down quark (uud). These three quarks are in a bound state and can interact with each other via the strong interaction (exchange of gluons). The emitted gluons can also split into virtual quark-antiquark pairs. These quarks are called sea quarks. Thus, in a proton-proton collision there is no fundamental interaction between both protons. The constituents of the proton (quarks and gluons), also called partons, participate in the interaction. Therefore, top-quark pairs can be produced via quark-antiquark annihilation or via gluon fusion. In the first production channel, a quark and a corresponding antiquark annihilate into a gluon which then splits into a top-antitop quark pair. In the case of gg fusion, two gluons from the protons fuse into another gluon, or they exchange a virtual top quark and then emit a real $t\bar{t}$ pair. The four leading-order (LO) Feynman diagrams are shown in Figure 2.2.

Protons were collided with a centre-of-mass energy of $\sqrt{s} = 13$ TeV at the LHC during Run II. Since the partons carry only a certain fraction x of the proton four-momentum, the effective collision energy $\sqrt{\hat{s}}$ of the parton-parton interaction is lower. The momentum distribution of the partons inside the proton is described by so-called parton distribution functions (PDF) which can be measured in deep inelastic collision experiments, e.g. in

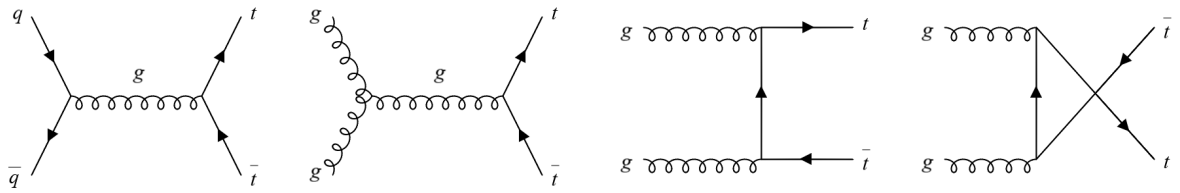

Figure 2.2.: The four leading-order Feynman diagrams for $t\bar{t}$ production in pp collisions: $q\bar{q}$ annihilation and gg fusion in the s-, t-, and u-channel (from left to right).

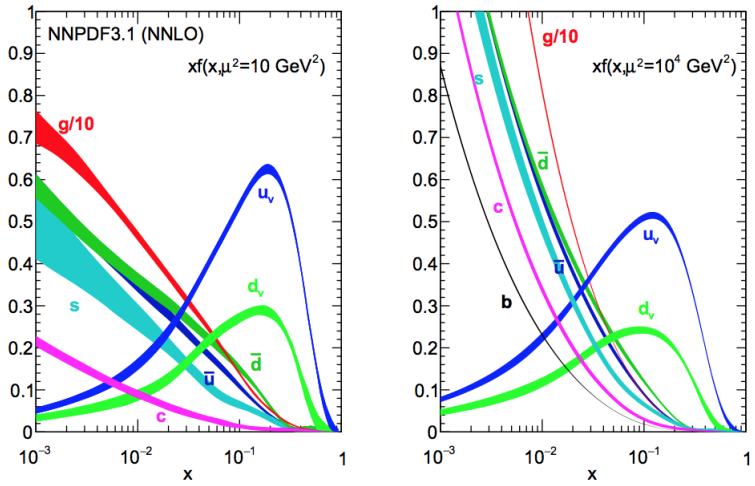

Figure 2.3.: The `NNPDF3.1` PDF set available in NNLO (next-to-next-to-leading order) accuracy [30]. The momentum density distribution of the momentum fractions x of the partons inside the proton are shown for two energy scales $\mu^2 = 10$ GeV^2 (left) and $\mu^2 = 10^4$ GeV^2 (right).

electron-proton collisions. Figure 2.3 shows an example for a PDF set. One can see that for high momentum fractions the valence quarks and for low momentum fractions the gluons highly dominate. To produce a real top-quark pair, it is required that $\sqrt{\hat{s}} > 2m_t$. Assuming that both partons carry the same fraction x, one gets $\sqrt{\hat{s}} = x\sqrt{s}$ and therefore $x > 2m_t/\sqrt{s}$. This means that the minimal required parton momentum fraction for top-quark pair production decreases with higher centre-of-mass energy. Thus, the production cross section $\sigma_{t\bar{t}}$ increases with the energy $\sqrt{s}$. It also means that the dominant production mechanism depends on it. As can be seen in Figure 2.3, the gluon contribution is dominant at lower x values and therefore gg fusion becomes more important at higher energies. This is the case at the LHC ($\sqrt{s} = 13$ TeV). At the $p\bar{p}$ collider TEVATRON ($\sqrt{s} = 1.96$ TeV), $q\bar{q}$ annihilation was the dominant process. That mode is disfavoured also at lower energies in pp collisions because the antiquark has to be a sea quark. However, the probability to find sea quarks with high fractions x (needed at lower energies) is very low.

To determine the $t\bar{t}$ production cross section, one has to calculate the cross section $\sigma_{ij\to t\bar{t}}$ for the interaction between the partons i and j, convolve it with the PDFs, and sum over all parton-parton combinations [31]:

$$\sigma_{t\bar{t}}\left(\sqrt{s}, m_t, \mu_{\mathrm{F}}, \mu_{\mathrm{R}}\right) = \sum_{i,j} \int \mathrm{d}x_i f_i(x_i, \mu_{\mathrm{F}}^2) \int \mathrm{d}x_j f_j(x_j, \mu_{\mathrm{F}}^2) \sigma_{ij\to t\bar{t}}\left(\sqrt{\hat{s}}, m_t, \mu_{\mathrm{F}}, \mu_{\mathrm{R}}, \alpha_s\right) .$$

This relation is called the QCD factorisation theorem. The PDFs $f_{i/j}$ are evaluated at the factorisation scale μ_{F}, and the renormalisation scale μ_{R} is introduced to deal with ultraviolet divergences in perturbative calculations. Both scales are set to the energy scale of the process, a common choice is $\mu_{\mathrm{F}} = \mu_{\mathrm{R}} = m_t$. Due to finite order of perturbative calculations, the calculated cross section will depend on these scales, although they are not physical.

Single Top-Quark Production

Top quarks can also be produced singly via the weak interaction. The LO Feynman diagrams for the different production modes (s-, t-, and Wt-channel) are shown in Figure 2.4.

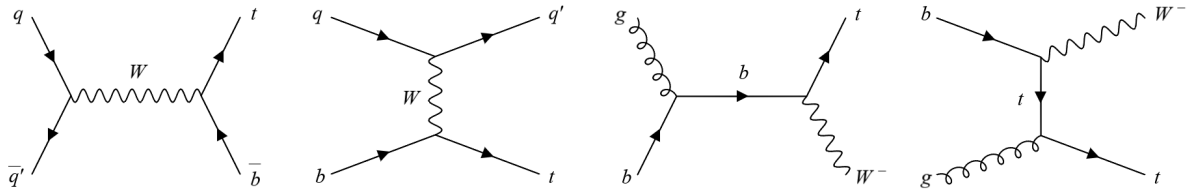

Figure 2.4.: Leading-order Feynman diagrams for single top-quark production: s-channel, t-channel, and associated production with a W boson (from left to right).

Single top-quark production was observed rather late at the Tevatron due to the higher amount of background compared to $t\bar{t}$ measurements. The combined cross section from DØ and CDF measurements in $p\bar{p}$ collisions at $\sqrt{s} = 1.96$ TeV is $\sigma_t = 2.25^{+0.29}_{-0.31}$ pb and $\sigma_{s+t} = 3.30^{+0.52}_{-0.40}$ pb for the t- and (s+t)-channel, respectively [32]. Now, also several measurements from the Atlas and Cms collaborations at $\sqrt{s} = 7,\ 8$, and 13 TeV were published. An overview of the latest results is given in Figure 2.5. Compared to CDF and DØ, Atlas and Cms have also measured Wt production. The Lhc combination gives $\sigma_{Wt} = 23.1 \pm 1.1$ (stat.) ± 3.3 (syst.) ± 0.8 (lumi.) pb at $\sqrt{s} = 8$ TeV, in agreement with the NLO + next-to-next-to-leading logarithmic (NNLL) prediction [33].

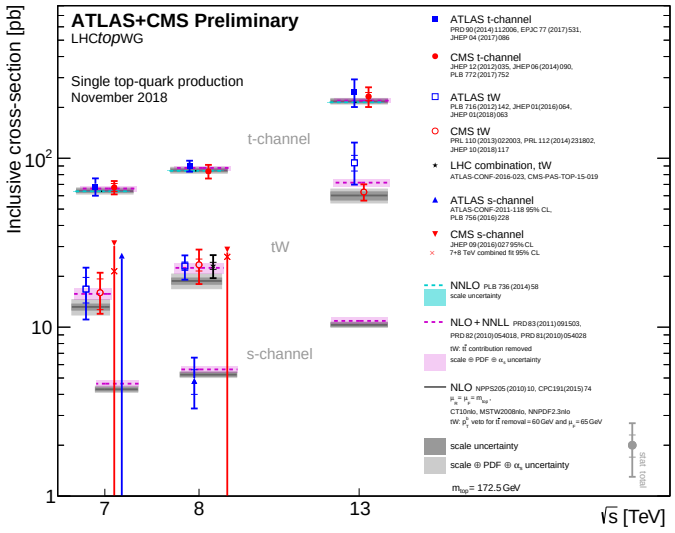

Figure 2.5.: Overview of LHC single top-quark production cross section measurements for different channels and centre-of-mass energies [34]. The measurements are compared to NLO and NLO+NNLL theoretical predictions. Measurements in the t-channel are additionally compared to NNLO calculations.

2.5.3. Top-Quark Decay

The top quark decays via the weak interaction into a down-type quark and a W boson. The probabilities of the three different decays are determined by the CKM matrix elements V_{td}, V_{ts}, and V_{tb}. Due to $|V_{tb}| \gg |V_{td}|, |V_{ts}|$ [18], the top quark decays in almost all cases into a (real) W boson and a bottom quark. The subsequent decay of the W boson determines the decay channel. W bosons either decay in a pair of charged lepton and neutrino (branching ratio $BR = 10.86 \pm 0.09\%$) or in a quark-antiquark pair ($BR = 67.41 \pm 0.27\%$) [18]. In top-quark pair events there are two W bosons, both decaying either hadronically or leptonically. Therefore, one distinguishes between the semileptonic (one leptonic and one hadronic W decay), the dileptonic (two leptonic W decays), and the hadronic decay channel (two hadronic W decays). Typically, tau leptons are not considered in the leptonic channels because they decay (often hadronically) within a particle detector and are not that easy to identify (compared to electrons and muons). The branching ratios of the $t\bar{t}$ decay channels are shown in Figure 2.6. Since different particles are detected in specific unique ways (see Section 3.2), different signatures in a particle detector are expected. Quarks cannot be observed as free particles because they hadronise and form jets. Neutrinos do not interact with the detector and remain undetected. Still, one can infer on the production of a neutrino in an event. In a proton-proton collision, the total transverse momentum before the collision is zero, and due to momentum conservation it has to be zero also after the collision. Therefore, if the sum of the transverse

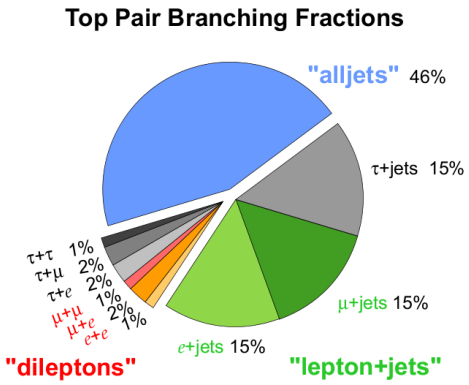

Figure 2.6.: The branching ratios of the different $t\bar{t}$ decay channels.

momenta of all detected objects is not zero, it means that there is at least one undetected particle in the event, e.g. a neutrino. In this context, one talks about missing transverse energy $E_{\mathrm{T}}^{\mathrm{miss}}$. Electrons and muons can be detected (rather) easily. In the following, they are simply called charged leptons (the τ is not considered). Thus, the following signatures are expected:

- Semileptonic Channel: one charged lepton, four jets (including two b-jets), $E_{\mathrm{T}}^{\mathrm{miss}}$
- Dileptonic Channel: two charged leptons, two b-jets, $E_{\mathrm{T}}^{\mathrm{miss}}$
- All-jets Channel: six jets (including two b-jets)

Here, b-jets refer to jets originating from the hadronisation of a bottom quark, which can be identified by specific algorithms (see Section 4.1.4). It has to be noticed that tau leptons, from leptonic W boson decays, can decay into an electron or a muon together with a neutrino, giving the same signature as in the semileptonic channel. Such decays will be included in the analysed events. The number of observed jets can also be higher due to the radiation of gluons in the initial or final state. Besides that, in a pp collision several other processes occur which give similar signatures in the detector. Such processes are called background processes. In the semileptonic channel (also called lepton+jets channel), the most important backgrounds arise from the production of single top quarks and also from the production of W bosons in association with jets. Since W bosons can decay leptonically, a very similar signature is observed. Another relevant background source is the so-called QCD multijet background. The reason is that jets or leptons within jets can be misidentified as leptons (so-called fake and non-prompt leptons). Another jet might not be reconstructed in the detector which leads to the observation of $E_{\mathrm{T}}^{\mathrm{miss}}$. To measure the $t\bar{t}$ production cross section, estimations of the different background contributions are needed (see Sections 4.2 and 4.3).

2.5.4. Previous Cross Section Measurements

The inclusive $t\bar{t}$ production cross section was first measured at the TEVATRON in $p\bar{p}$ collisions at $\sqrt{s} = 1.8$ TeV [35, 36]. More precise measurements were published later for $\sqrt{s} = 1.96$ TeV. The CDF and DØ combination is $\sigma_{t\bar{t}} = 7.60 \pm 0.41$ pb [37] which is in agreement with the SM prediction $7.35^{+0.28}_{-0.33}$ pb. At the LHC, the cross section was measured in pp collisions at different centre-of-mass energies. First measurements were performed at 7 TeV by ATLAS and CMS in the lepton+jets, the dilepton, and the all-jets channel. The LHC combination is $\sigma_{t\bar{t}} = 173.3 \pm 2.3$ (stat.) ± 7.6 (syst.) ± 6.3 (lumi.) pb, which corresponds to a precision of 5.8% and agrees with the SM prediction [38]. Also for $\sqrt{s} = 8$ TeV, several measurements were published. ATLAS measured in the lepton+jets channel $\sigma_{t\bar{t}} = 248.3 \pm 0.7$ (stat.) ± 13.4 (syst.) ± 4.7 (lumi.) pb [39] and in the dilepton channel $\sigma_{t\bar{t}} = 242.9 \pm 1.7$ (stat.) ± 5.5 (syst.) ± 5.1 (lumi.) pb [40], using 20.2 fb^{-1} of data. Other measurements were also made in the all-jets channel by CMS [41] and in the τ_h+jets channel by ATLAS [42]. The LHC combination in the dilepton channel (providing the highest precision) is $\sigma_{t\bar{t}} = 241.5 \pm 1.4$ (stat.) ± 5.7 (syst.) ± 6.2 (lumi.) pb with an uncertainty of 3.5% [43]. Most recent measurements at 13 TeV are shown in Figure 2.7. Both ATLAS and CMS published preliminary and also final results in different decay channels. The most precise published ATLAS result was achieved in the $e\mu$ channel with $\sigma_{t\bar{t}} = 818.8 \pm 8$ (stat.) ± 27 (syst.) ± 19 (lumi.) pb, using 3.2 fb^{-1} of data [44]. The preliminary result in the lepton+jets channel, obtained by analysing 85 pb^{-1} of data, is $\sigma_{t\bar{t}} = 817 \pm 13$ (stat.) ± 103 (syst.) ± 88 (lumi.) pb [45]. CMS achieved a similar precision in the dilepton channel [46]. In the lepton+jets analysis, a larger dataset (2.2 fb^{-1}) was used, resulting in a higher precision [47] than in the last preliminary ATLAS result.

An ATLAS measurement at 13 TeV in the lepton+jets channel using the full Run II dataset is still missing which gives the motivation to prepare such an analysis. The predicted cross section at 13 TeV is $\sigma^{\mathrm{SM}}_{t\bar{t}} = 831.76^{+19.77}_{-29.20}\,(\mathrm{scale})^{+35.06}_{-35.06}\,(\mathrm{PDF} + \alpha_s)$ pb for a top-quark mass of $m_t = 172.5$ GeV. It was calculated at NNLO in QCD including resummation of NNLL soft gluon terms with `Top++2.0` [48–54]. The factorisation and renormalisaton scales were set to $\mu_{\mathrm{F}} = \mu_{\mathrm{R}} = m_t$. The first uncertainty was evaluated by independently varying both scales by a factor of 2 (while not allowing them to differ more than a factor of 2 from each other). The PDF+α_s uncertainty was determined using the `PDF4LHC` prescription [55] with the `MSTW2008 68% CL NNLO` [56, 57], `CT10 NNLO` [58, 59], and `NNPDF2.3 5f FFN` [60] PDF sets. The midpoint of the envelope of the cross sections calculated with these three PDF sets is taken as the central prediction.

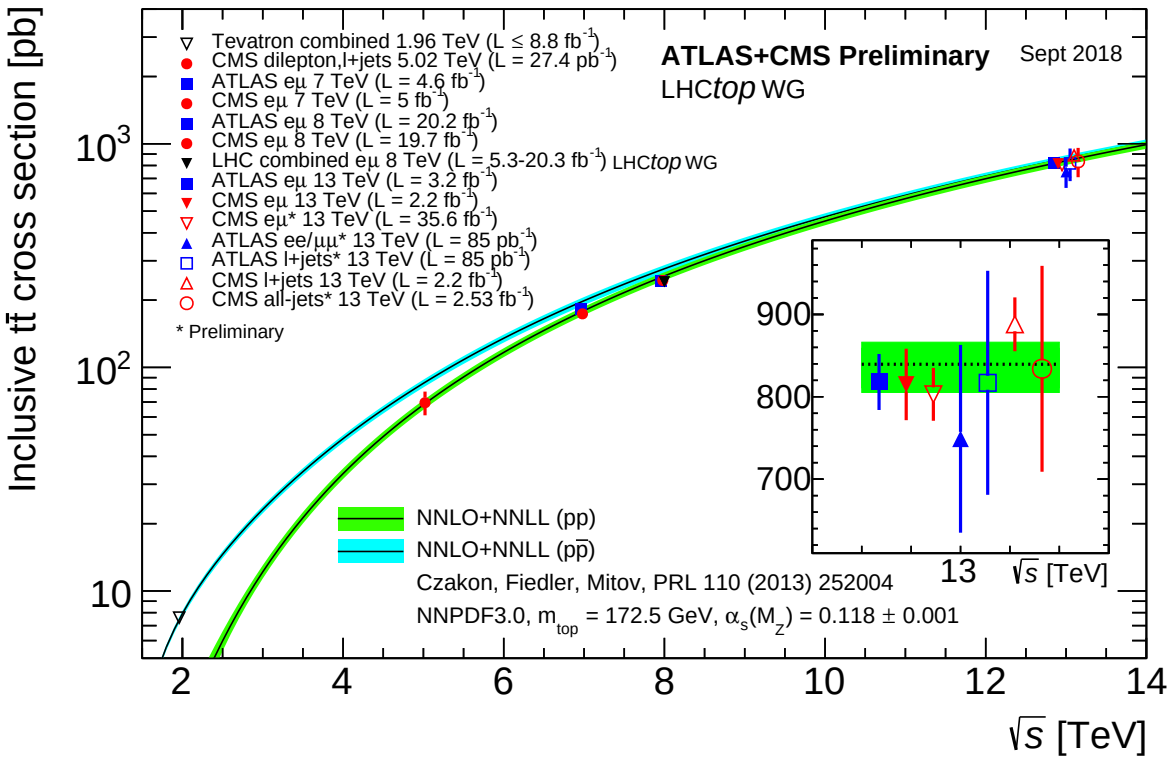

Figure 2.7.: Summary of LHC and TEVATRON $t\bar{t}$ cross section measurements at different centre-of-mass energies [34]. Measurements are compared to theory predictions calculated at next-to-next-to-leading order (NNLO) including resummation of next-to-next-to-leading logarithmic (NNLL) soft gluon terms with `Top++2.0`. Theory uncertainties include uncertainties due to the renormalisation and factorisation scale, the PDF, and α_s. Measurements and predictions assume $m_t = 172.5$ GeV.

3. Experimental Setup

In this chapter, the overall experimental setup will be described[1]. The Large Hadron Collider (LHC), which is currently the most powerful proton-proton collider in the world, will be presented in Section 3.1. Furthermore, the main setup of the ATLAS detector, located at the LHC, will be explained in Section 3.2.

3.1. The Large Hadron Collider

The Large Hadron Collider (LHC) is a superconducting, two-ring particle accelerator located at CERN (**C**onseil **e**uropéen pour la **r**echerche **n**ucléaire) in Geneva and is up to now the most powerful accelerator ever built. There, protons (and also heavy ions) are accelerated up to high energies and brought into collision. Figure 3.1 gives an overview of the CERN accelerator complex. The main component is a synchrotron (circular accelerator) with a circumference of 27 km, located about 100 m underground [61]. That tunnel already existed when the construction of the LHC started. Previously, it was used for the electron-positron collider LEP. The LHC is actually not a circular accelerator but consists of eight arcs and straight sections. There are two rings in the tunnel where protons are accelerated in opposite directions. Before they are injected into the beam pipes, they pass through a chain of accelerators [61], which is illustrated in Figure 3.1. First, they are injected into a linear accelerator (Linac 2) and are accelerated to an energy of 50 MeV. During this first acceleration, the protons are split into bunches. Then, they are injected into the Proton Synchrotron Booster (PSB). From there, the protons are led to the Proton Synchrotron (PS) with an energy of 1.4 GeV. Their energy is further increased to 25 GeV, and they are then injected to the Super Proton Synchrotron (SPS). Finally, the proton bunches pass to the LHC with an energy of 450 GeV, where they are accelerated to the desired energy. During Run I, the LHC operated at a centre-of-mass energy of $\sqrt{s} = 7$ TeV (2011) and at $\sqrt{s} = 8$ TeV (2012). For Run II (2015-2018), the energy was increased to 13 TeV. In the future, it is planned to increase it further to 14 TeV.

[1] This chapter is based on the MSc interim report.

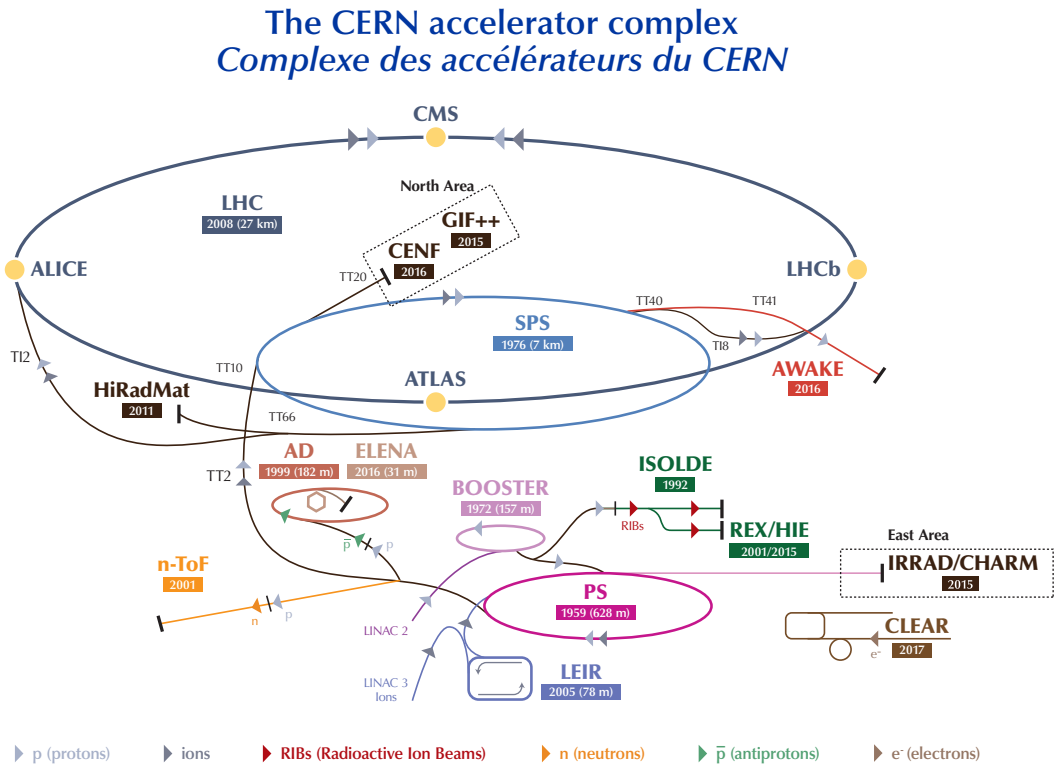

Figure 3.1.: Overview of the LHC and experiments. Protons pass several pre-accelerators before being injected into the main accelerator © CERN.

The proton bunches inside the LHC are bent and focused by superconducting magnets which are cooled down to -271.3 °C by liquid helium. 1232 dipole magnets, which are 15 m long each, are surrounding the beam pipe and keep the protons on a circular orbit. 392 quadrupole magnets (each 5-7 m long) are used to focus the bunches [61].

In total, there are four collision points with four main experiments: ALICE, ATLAS, CMS, and LHCb (see Figure 3.1). The ATLAS and CMS detectors are cylindrically symmetrical multi-purpose detectors, which means that they can be used for a variety of physics analyses. Main tasks are, among others, studies of the Higgs mechanism (the Higgs boson was observed in 2012 [11, 12]), studies of top-quark physics, and the search for signals from physics beyond the Standard Model (BSM), for example supersymmetry [62, 63]. They are also the biggest detectors at the LHC. The LHCb detector is an asymmetric detector. There, decays of B hadrons (which contain a bottom quark) are

studied for CP violation measurements and for the search for BSM physics [64]. ALICE mainly focuses on heavy-ion collisions. In these collisions, the production of a quark-gluon plasma is searched for [65]. Apart from these, there are also smaller experiments: TOTEM, MoEDAL, and LHCf [66–68].

3.2. The ATLAS Detector

The ATLAS detector (**A** **T**oroidal **L**HC **A**pparatu**S**) is one of the two largest particle detectors located at the LHC. It has a length of about 44 m and is 25 m in diameter. Additionally, it has an approximately cylindrical structure around the beam collision point and covers almost the whole solid angle around it. ATLAS measures, as almost every particle detector, the momenta and the electric charge of charged particles, their total energy, and tracks of particles and jets. By measuring the transverse momenta p_{T} of all objects in the final state, it is possible to measure the missing transverse energy. The presence of $E_{\mathrm{T}}^{\mathrm{miss}}$ in an event indicates the presence of a neutrino, which does not interact with the detector parts and thus remains undetected. The ATLAS detector consists of three main detector components: the inner detector, the calorimeter system, and the muon spectrometer. Additionally, it contains several toroidal and solenoidal magnets whose purpose is to bend charged particles (see Figure 3.2). The transverse momentum and energy resolution of the different detector components is given in Table 3.1.

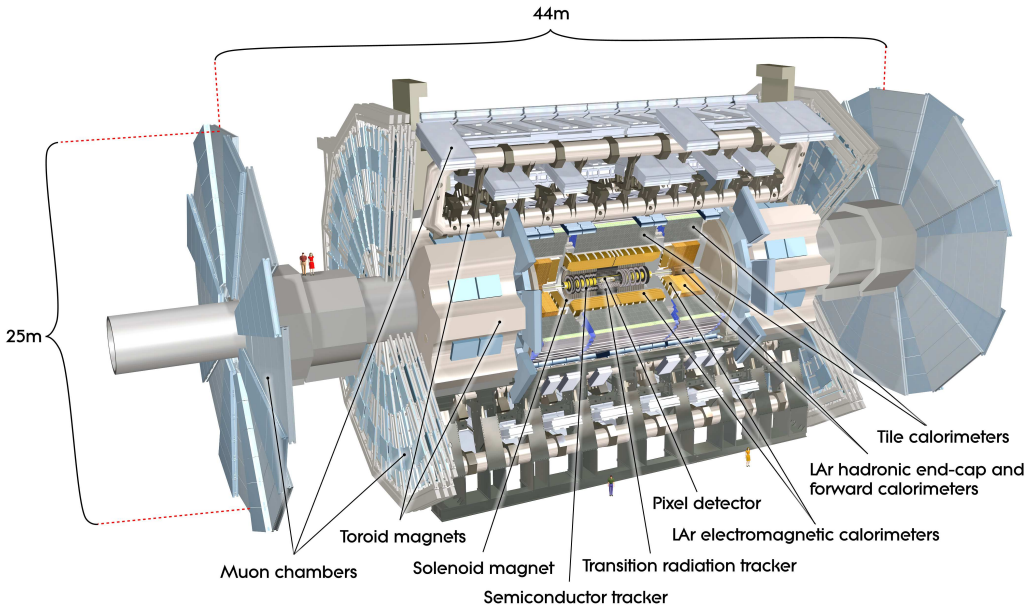

Figure 3.2.: Overview of the ATLAS detector together with all its subsystems © CERN.

Component	**Resolution**	**η coverage**
Inner Detector	$\sigma_{p_T}/p_T = 0.05\% \cdot p_T \oplus 1\%$	± 2.5
EM Calorimeter	$\sigma_E/E = 10\%/\sqrt{E} \oplus 0.7\%$	± 3.2
Hadronic Calorimeter		
- barrel and end-cap	$\sigma_E/E = 50\%/\sqrt{E} \oplus 3\%$	± 3.2
- forward	$\sigma_E/E = 100\%/\sqrt{E} \oplus 10\%$	$3.1 < \lvert\eta\rvert < 4.9$
Muon Spectrometer	$\sigma_{p_T}/p_T = 10\%$ at $p_T = 1$ TeV	± 2.7

Table 3.1.: Transverse momentum and energy resolution of the ATLAS detector components as well as their η coverage (see Equation 3.1). The units for p_T and E are in GeV [62].

3.2.1. The ATLAS Coordinate System

ATLAS makes use of a right-handed coordinate system. The origin is in the beam interaction point and the x-axis points from there to the centre of the LHC ring. The z-axis is in direction of the beam pipe and the y-axis shows upwards. Due to the symmetry, cylindrical coordinates are used, where ϕ is the angle along the plane transverse to the beam with respect to the x-axis and θ is the polar angle. Instead of the polar angle, typically the pseudorapidity is used:

$$\eta = -\ln\left(\tan\frac{\theta}{2}\right) . \tag{3.1}$$

The distance between two particles/objects in the $\eta - \phi$ plane is defined as

$$\Delta R = \sqrt{\Delta\eta^2 + \Delta\phi^2} . \tag{3.2}$$

3.2.2. The Inner Detector

The inner detector consists of three components which are cylindrically arranged around the beam pipe. It is immersed in a magnetic field of 2 T produced by a solenoid located between the tracking system and the calorimeter. Charged particles are bent because of the acting Lorentz force. By reconstructing their tracks, the electric charge and the momentum can be measured. An overview is given in Figure 3.3.

The most inner part is the ATLAS Pixel Detector. It consists of many silicon semiconductor pixels (in total about 80 millions) with a minimum size of 50 x 400 μm^2, arranged on three barrel layers and three discs on each end-cap. Ionisation induced by traversing electrically charged particles produces electron-hole pairs. By measuring the electrical signal, the location of the ionisation, and thus of the charged particles, can be measured.

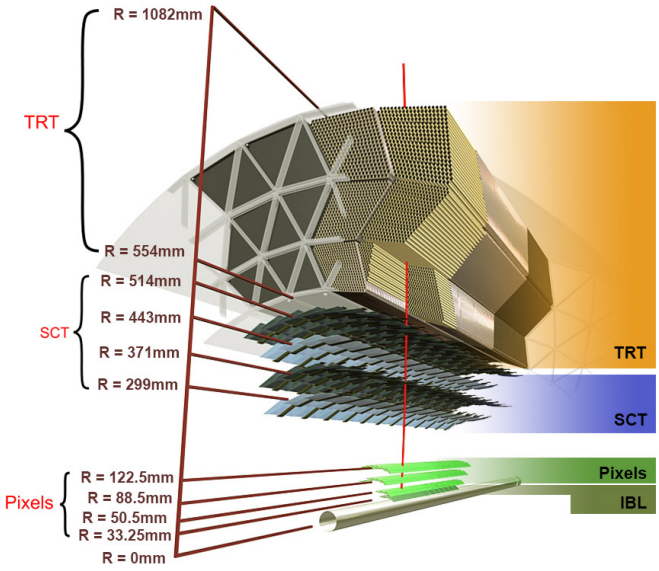

Figure 3.3.: Schematic view and detailed layout of the Inner Detector including the new IBL © Cern.

Thus, precise track reconstruction with a resolution of 14 x 115 μm^2 around the interaction point is possible. This is very important due to the high track density there. The Pixel Detector therefore plays a significant role in the reconstruction of primary and secondary vertices, the latter being useful information for b-tagging. After Run I, the Insertable B-Layer (IBL) was added to improve the b-tagging performance [69]. It has a distance of about 3.3 cm from the beam axis and consists of many silicon semiconductor pixels with a size of 50 x 250 μm^2.

The second component is the Semiconductor Tracker (SCT) which consists of four cylindrical barrels and in total 18 discs in the end-caps. The principle of track measurements is very similar to the Pixel Detector. But instead of pixels, the SCT consists of silicon microstrips with a width of 80 μm. In the direction transverse to the strips, a resolution of 17 μm is achieved.

The last component is the Transition Radiation Tracker (TRT). The main part consists of thin straw tubes with a diameter of 4 mm, which contain a 0.03 mm thin gold-plated tungsten wire in the centre. They are filled with a gas mixture of Xe, CO_2, and O_2. Traversing charged particles ionise the gas and the produced electrons undergo avalanche multiplication close to the wire. By measuring the signal, the position of the particle is determined. Additionally, the individual straw tubes are embedded in a radiator material. Highly relativistic particles can emit transition radiation when they cross the boundary between different materials. This can be used to distinguish electrons from pions.

3.2.3. The Calorimeter System

The Calorimeter system consists of the Electromagnetic and the Hadronic Calorimeter (see Figure 3.4). Its purpose is the measurement of the energy (and direction) of electrons, photons, and jets (i.e. hadrons), but also of the missing transverse energy. It is designed such that the mentioned particles deposit all their energy there and are stopped.

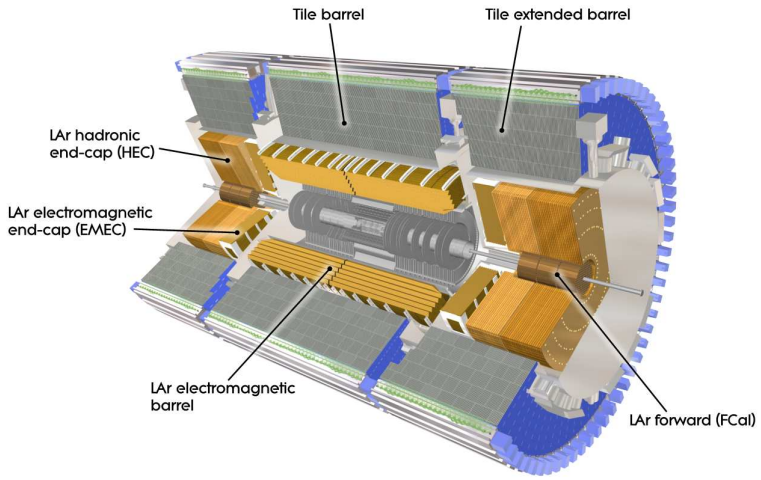

Figure 3.4.: Schematic view of the ATLAS Calorimeter System © CERN.

The Electromagnetic Calorimeter (ECAL) measures the deposited energy of electrons and photons. It is divided into a barrel part and two end-caps. Lead is used as absorber material while liquid argon (LAr) is used as the active medium. The ECAL is a sampling calorimeter which means that absorber and detector layers alternate. Electrons lose their energy via the emission of photons (Bremsstrahlung) in the absorber material. These photons can split into electron-positron pairs which subsequently again emit photons. All in all, a particle shower is created and the whole initial energy of the electron/positron is deposited. The energy deposition of an incoming photon works in a similar manner. The particles inside the shower ionise the LAr and the produced electrons and ions are collected to create a signal which is proportional to the initial particle energy.

The ATLAS Hadronic Tile Calorimeter is located behind the ECAL in the central region and measures the energy of hadrons. It is made of a barrel and two extended barrel parts. Steel is used as an absorber and scintillating tiles as an active medium. Hadronic particles deposit their energy and consequently light is emitted which is measured by photo-multipliers. On the contrary, the Hadronic End-Cap Calorimeter uses copper as absorber material and LAr as active medium. The last main part of the calorimeter system is the Forward Calorimeter. Again, LAr is used as active medium while copper/tungsten is the absorber material in the electromagnetic/hadronic component.

3.2.4. The Muon Spectrometer

Muons have a much larger mass than electrons (about 200 times larger) and therefore Bremsstrahlung is suppressed. Consequently, muons deposit only a very small fraction of their energy in the calorimeters and are not stopped there. Together with neutrinos, they are the only particles that can pass the calorimeters. However, in contrast to neutrinos, they can still be measured in the Muon Spectrometer (MS). It is made of about 4000 muon chambers and is immersed in a magnetic field produced by a toroidal magnet system. This system consists of a barrel toroid and two end-cap toroids producing a field with an average strength of 0.5 T and 1 T, respectively. Muons are bent in the magnetic field and by measuring their trajectories, their charge and momentum are determined. The MS consists of four parts (see Figure 3.5): Thin Gap Chambers (TGC), Resistive Plate Chambers (RPC), Monitored Drift Tubes (MDT), and Cathode Strip Chambers (CSC).

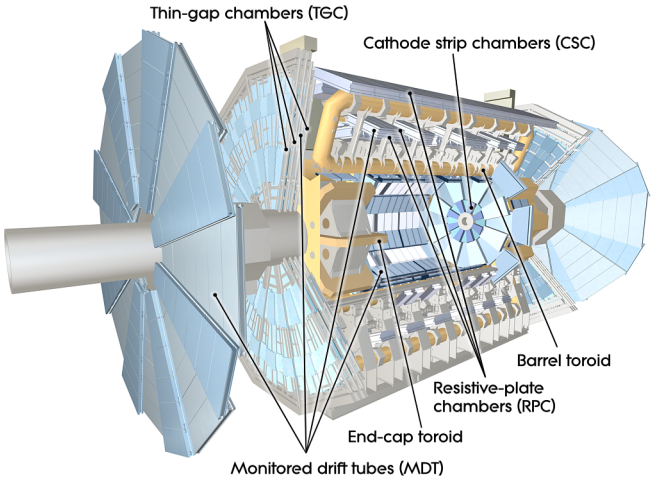

Figure 3.5.: Schematic view of the ATLAS Muon Spectrometer © CERN.

MDTs are used in the barrel and the end-cap parts to measure muon trajectories. They consist of several layers of drift tubes filled with an Ar-CO_2 mixture. Electrons from ionisation, induced by passing muons, are collected at the anodes to form the signal. The CSCs are multi-wire proportional chambers whose cathodes are split into strips perpendicular to the wires. They are located at the end-caps and provide precise measurements of muon coordinates in the forward region. The RPCs and TGCs deliver fast track information and are mainly used for triggering (Section 3.2.5). They are located at the barrel and the end-cap parts, respectively.

3.2.5. Trigger System

The collision rate at the LHC is very high (40 MHz). Additionally, at each bunch-crossing several *pp* collisions happen (pile-up). Therefore, it is not possible to record all the data. But this is not even necessary because most events are not interesting for physics analyses. Thus, a trigger system is used which selects interesting events and reduces the amount of data to be recorded to manageable sizes [70]. It is divided into two levels. The Level-1 trigger uses a small amount of information from the calorimeters and the muon spectrometer to look for example for muons with high transverse momentum. Subsequently, regions of interest are built. The number of bunch-crossings, which is further passed to the software-based high level trigger (HLT), is reduced from 40 millions to less than 100000. The HLT is able to access full event data and analyses the regions of interest defined by the Level-1 trigger. After deciding whether to keep the event or not, the recorded rate of events is further reduced to about 1 kHz.

4. Data Preparation

In this chapter, all relevant concepts and definitions needed to prepare the data for the $t\bar{t}$ cross section measurement are presented[1]. For the analysis, estimations of the contributions from all background sources and also from the signal ($t\bar{t}$) itself are needed. Sometimes, backgrounds can be estimated directly from the observed data, but more often so-called Monte Carlo (MC) simulations, based on the SM, are needed. Simulations are done in several steps. First, events are generated on parton level. In the next step, the parton showering and the hadronisation processes are modelled. Finally, the response of the ATLAS detector to the generated particles is simulated. MC events and data are then processed by the same reconstruction software which (among other things) applies object definitions, determines scale factors, and applies selection criteria.

4.1. Object Definitions

4.1.1. Electrons

Electrons are identified using a likelihood-based multivariate method which takes information on tracks and energy deposits into account [71]. Two different working points are used. For the signal selection, electrons are required to fulfil the `TightLH` criteria. In order to estimate the multijet background (see Section 4.3) from data, loose criteria (`MediumLH`) are applied on electrons. In both selections, electrons are required to have $p_{\mathrm{T}} > 25$ GeV and $|\eta_{\mathrm{cluster}}| < 2.47$ while candidates in the transition region between the barrel and the end-cap part of the ECAL ($1.37 < |\eta_{\mathrm{cluster}}| < 1.52$) are discarded. Tight electrons also have to fulfil the criteria of the `Gradient` isolation working point [72]. For loose electrons, no isolation criteria are required. Additionally, track-to-vertex association (TTVA) cuts are imposed. The transverse impact parameter has to fulfil $|d_0/\sigma(d_0)| < 5$ and the longitudinal impact parameter $|z_0 \sin(\theta)| < 0.5$ mm. Here, d_0 and z_0 refer to the transverse and longitudinal distance of closest approach between the track and the primary vertex.

[1] This chapter is based on the MSc interim report.

4.1.2. Muons

Muons are identified by the reconstruction of tracks in the inner detector and in the muon spectrometer [73]. Several quality criteria are imposed on the reconstructed tracks. Candidates are required to fulfil `Medium` identification criteria and to have $p_{\mathrm{T}} > 25$ GeV and $|\eta| < 2.5$. As for electrons, the `Gradient` isolation criteria and TTVA cuts are imposed. Muons have to fulfil $|d_0/\sigma(d_0)| < 3$ and $|z_0 \sin(\theta)| < 0.5$ mm. For the estimation of the non-prompt muon background, only the isolation requirements are dropped.

4.1.3. Jets

Jets are reconstructed from energy-deposit clusters in the calorimeter [74]. The anti-k_t algorithm [75] is used together with a radius parameter of $R = 0.4$. Jets are required to have $p_{\mathrm{T}} > 25$ GeV, $|\eta| < 2.5$, and are calibrated with the `EMTopo` scheme [76]. To suppress jets from pile-up, the Jet Vertex Tagger (JVT) is used [77]. As recommended, the JVT discriminant is required to be larger than 0.59 for jets with $p_{\mathrm{T}} < 120$ GeV and $|\eta| < 2.5$.

4.1.4. B-Tagging

Jets originating from the hadronisation of b quarks can be identified (b-tagged) by multivariate algorithms. B mesons (mesons containing b quarks) have a relatively long lifetime and thus can travel some distance before they decay. Therefore, one can observe so-called secondary vertices in b-jets which are displaced from the primary vertex in an event. Such information (and also other variables like the mass) is used by b-tagging algorithms. Here, b-jets are identified using the MV2c10 algorithm [78] which is a Boosted Decision Tree (BDT) combining the outputs from other tagging algorithms. In this analysis, scale factors for pseudo-continuous b-tagging are used, which means that several working points of different b-tagging efficiencies (60%, 70%, 77%, 85%) are calibrated and can be used.

4.1.5. Missing Transverse Energy

In the ATLAS collaboration, the magnitude of the missing transverse momentum is called missing transverse energy $E_{\mathrm{T}}^{\mathrm{miss}}$ (this is strictly speaking only true for massless particles). It is an indication for particles which have not deposited their energy in the detector. In the case of only one neutrino in the event, it can be assigned to its transverse momentum.

The missing transverse energy is determined by [79]

$$E_{x(y)}^{\text{miss}} = -\sum_{i\in\{\text{hard objects}\}} p_{x(y),i} - \sum_{j\in\{\text{soft signals}\}} p_{x(y),j}\,. \tag{4.1}$$

The first term includes all hard objects, i.e. reconstructed jets, electrons, and muons. The second term includes tracks and energy deposits in the calorimeters not associated to any reconstructed object.

4.1.6. Overlap Removal

To avoid double counting of final state objects, overlap removal is applied. A recommended and standard algorithm is used [80]. Overlap removal includes, among others:

- Electrons sharing a track with a muon are removed.
- If a jet has a distance of $\Delta R < 0.2$ to an electron, it is removed. If multiple jets are found within that distance, only the closest one is removed.
- If the distance between a jet and an electron is between 0.2 and 0.4, the electron is removed.
- Muons with a distance of $\Delta R < 0.4$ to a jet are removed if more than two tracks are associated to the jet. Otherwise, the jet is removed.

4.2. MC Samples

As already mentioned, simulations of signal and background processes are needed for a cross section measurement. In the lepton+jets channel, the relevant backgrounds are $W+$jets, single top quark, multijet, $Z+$jets, diboson (WW, WZ, ZZ), $t\bar{t}V$ ($V = W, Z$), and $t\bar{t}H$ production. Different MC generators are used for the simulation of the several processes. Heavy-flavour decays (for example decays of B mesons) in processes not generated with Sherpa [81] are simulated with Evtgen [82]. The response of the Atlas detector to particles is simulated with the Geant 4 framework [83, 84]. However, for the estimation of modelling uncertainties, alternative simulated samples are used which utilise the fast parametrisation `Atlfast-II` (AFII) of the detector response [85]. To simulate additional pp interactions in the same or nearby bunch-crossings (pile-up), a set of minimum-bias interactions is generated with Pythia 8 [86] and overlaid with the hard-scattering events. To ensure a matching of the pile-up levels, the number of additional pp interactions in the MC is finally reweighted to the distribution observed in data.

The nominal $t\bar{t}$ sample is simulated with the NLO matrix element (ME) generator Powheg-Box (v2) [87] which is interfaced to Pythia 8 for parton showering and hadronisation. The generator uses a top-quark mass of 172.5 GeV and the `NNPDF3.0NLO` PDF set [88]. The `A14` tune with the `NNPDF2.3LO` PDF set is applied [89]. The h_{damp} parameter, which controls the first gluon emission, is set to $1.5m_t$. The events are normalised to the NNLO+NNLL cross section (Section 2.5.4) which is 831.76 pb. However, the $t\bar{t}$ normalisation will be a free parameter in the fit (see Section 5.3). Since alternative $t\bar{t}$ samples are produced with fast detector simulation (AFII), the nominal $t\bar{t}$ AFII sample is also considered to ensure proper comparisons for modelling uncertainties.

Alternative $t\bar{t}$ AFII samples are used to describe the effect of modelling uncertainties. For hadronisation modelling studies, Powheg-Box (v2) with the `NNPDF3.0NLO` PDF set, interfaced to Herwig 7 [90, 91], is used. The top-quark mass and the h_{damp} parameter are set to the same values as in the nominal sample but the `H7UE` tune [91] is applied. Uncertainties related to initial/final state radiation (ISR/FSR) and the PDF, however, are all estimated by reweighting the nominal Powheg-Box + Pythia 8 AFII sample using dedicated MC event weights. The procedures will be detailed in Section 6.2.

Single top-quark production (s-, t-, and Wt-channel) is simulated with Powheg-Box (v2), using the `NNPDF3.0NLO` PDF set, interfaced to Pythia 8. The `A14` tune with the `NNPDF2.3LO` PDF set is applied and the top-quark mass is set to 172.5 GeV. In the nominal Wt sample, the diagram removal (DR) scheme is used to remove the overlap between the $t\bar{t}$ and Wt final state [92]. An alternative sample with the diagram subtraction (DS) scheme is used to estimate the effect of the choice of a specific scheme. Single top-quark AFII samples generated with Powheg-Box (v2) and interfaced to Herwig 7 are used to evaluate the uncertainty related to the parton shower and hadronisation modelling. The estimation of all other uncertainties is described in more detail in Section 6.2. The s- and t-channel samples are normalised to the NLO cross section [93, 94], while the Wt samples are normalised to the approximate NNLO prediction [95].

Events with Z or W bosons in association with jets are generated and showered with Sherpa (v2.2.1). The `NNPDF3.0NNLO` PDF set is utilised. The samples are normalised to the NNLO cross sections [96]. Events with two vector bosons (WW, WZ, ZZ) are generated and showered with Sherpa (v2.2.1 and v2.2.2). Again, the `NNPDF3.0NNLO` PDF set is used. The events are normalised to the NLO QCD cross sections [97].

The production of top-quark pairs together with a vector boson ($t\bar{t}W$, $t\bar{t}Z$) is simulated with MadGraph5_aMC@NLO [98] interfaced to Pythia 8. The `NNPDF3.0NLO` PDF set is used for the ME generation and the `A14 NNPDF2.3LO` tune is applied. The events are normalised to the predicted NLO QCD+EW cross sections [99].

Events with a top-quark pair in association with a Higgs boson ($t\bar{t}H$) are generated with POWHEG-BOX (v2) using the `NNPDF3.0NLO` PDF set. The showering and hadronisation are simulated with PYTHIA 8, and the assumed Higgs boson mass is 125 GeV. The events are normalised to the predicted NLO QCD+EW cross section [99].

Finally, all MC events are reweighted to improve the agreement with data with respect to several efficiencies, e.g. the trigger efficiency. The weights take into account the MC event weights, scale factors for the leptons, for pile-up, for the b-tagging, and the JVT efficiency. Because of different pile-up conditions during different data-taking periods, MC samples are split in three different campaigns for 2015+2016 (`mc16a`), 2017 (`mc16d`), and 2018 data (`mc16e`). An overview of all used datasets can be found in Appendix A. Distributions in each MC campaign are scaled to the integrated luminosity in the respective data-taking period (see Section 6.1.1).

4.3. Multijet Background

Events with multiple jets (also called QCD multijet background) can also mimic the signature of $t\bar{t}$ production in the detector. The reason is that jets could be falsely identified as a lepton, or a photon in a jet (e.g. from the decay of neutral pions) could fake a prompt electron via conversion. Additionally, leptons originating from the decay of heavy-flavour hadrons could also mimic prompt leptons, especially muons. As it is difficult to simulate such background sources, a data-driven approach is used based on the so-called matrix method [100]. The matrix method makes use of two lepton selections in data: loose and tight leptons (Sections 4.1.1 and 4.1.2). In general, in both selections there are real and also fake leptons. The numbers of reconstructed leptons in these regions (N^{loose} and N^{tight}) are given by

$$N^{\text{loose}} = N^{\text{loose}}_{\text{real}} + N^{\text{loose}}_{\text{fake}} , \tag{4.2}$$

$$N^{\text{tight}} = N^{\text{tight}}_{\text{real}} + N^{\text{tight}}_{\text{fake}} . \tag{4.3}$$

Introducing the real and fake lepton efficiencies ϵ_{real} and ϵ_{fake} (probabilities that loose real/fake leptons fulfil also tight criteria), one can write

$$N^{\text{tight}} = \epsilon_{\text{real}} N^{\text{loose}}_{\text{real}} + \epsilon_{\text{fake}} N^{\text{loose}}_{\text{fake}} . \tag{4.4}$$

Knowing these efficiencies and using the previous equations, one can estimate the number of fake leptons in the tight selection:

$$N_{\text{fake}}^{\text{tight}} = \frac{\epsilon_{\text{fake}}}{\epsilon_{\text{real}} - \epsilon_{\text{fake}}}(\epsilon_{\text{real}} N^{\text{loose}} - N^{\text{tight}}) \,. \tag{4.5}$$

The real and fake lepton efficiencies are measured in regions which are enriched in real or fake leptons. This is done centrally in ATLAS and is described in some more detail in Ref. [101]. The efficiencies are measured as a function of several variables like leading[2] jet p_{T}, lepton η, lepton p_{T}, or the distance between the lepton and the closest jet. Finally, to estimate the multijet background contribution, each event in the loose lepton selection in data is weighted with

$$w = \frac{\epsilon_{\text{fake}}}{\epsilon_{\text{real}} - \epsilon_{\text{fake}}}(\epsilon_{\text{real}} - \delta) \,, \tag{4.6}$$

where $\delta = 1$ if the respective event additionally passes the tight lepton criteria, and 0 otherwise. The used parametrisations of the efficiencies are summarised in Table 6.1 in Section 6.1.9.

4.4. Event Selection

The measurement of the $t\bar{t}$ production cross section is prepared to be performed in the lepton+jets channel. Therefore, events are selected according to the expected signature (see Section 2.5.3). ATLAS data measured between the years 2015 and 2018 at $\sqrt{s} = 13$ TeV is analysed, which corresponds to a total integrated luminosity of 139 fb^{-1}, measured with the LUCID-2 system [102]. The `AnalysisTop` [103] software (tag 21.2.53) is used for the event selection. All events have to pass data quality requirements by checking that they are contained in the luminosity blocks specified in the respective good run list (GRL). Additionally, each event is required to have a primary vertex with at least two matched tracks. The `GOODCALO` option is applied to remove events in which the LAr or the Tile calorimeter are in an error state. After the overlap removal, jet cleaning is applied using the `LooseBad` option. This removes events with fake jets originating from cosmic events, non-collision background, or fake signals due to detector noise.

Events are further required to pass single-lepton triggers which are summarised in Table 4.1 for each data-taking period. The presence of exactly one electron or muon with $p_{\text{T}} > 25$ GeV for 2015 data, $p_{\text{T}} > 27$ GeV for 2016 data, and $p_{\text{T}} > 28$ GeV for 2017 and

[2]The jet with the highest p_{T} among all jets in the event.

	2015	2016, 2017, 2018
Electron	HLT_e24_lhmedium_L1EM20VH HLT_e60_lhmedium HLT_e120_lhloose	HLT_e26_lhtight_nod0_ivarloose HLT_e60_lhmedium_nod0 HLT_e140_lhloose_nod0
Muon	HLT_mu20_iloose_L1MU15 HLT_mu50	HLT_mu26_ivarmedium HLT_mu50

Table 4.1.: The used single-lepton triggers for the different data-taking periods.

2018 data is imposed. In case there is a second lepton with $p_{\mathrm{T}} > 25$ GeV, the whole event is discarded. Finally, the selected lepton has to match the lepton that fired the trigger. In order to operate in the plateau region of the trigger efficiency, the offline lepton p_{T} cuts were set slightly higher for 2016-2018 data[3]. Additionally, at least four jets with $p_{\mathrm{T}} > 25$ GeV are required[4]. Because of the presence of b-jets in $t\bar{t}$ events, at least one jet of the selected ones has to be b-tagged by the MV2c10 algorithm with the 60% efficiency working point (WP). Pseudo-continuous b-tagging is used which provides scale factors allowing to use different b-tagging efficiency WPs in the later analysis. This was done previously to investigate the possible usage of the b-tag weight distributions in a neural network [104]. However, the final analysis does not make use of it. In order to suppress the multijet background, cuts on $E_{\mathrm{T}}^{\mathrm{miss}}$ and the transverse W boson mass are required. The latter is defined as

$$m_{\mathrm{T}}^{W} = \sqrt{2p_{\mathrm{T}}(\ell)E_{\mathrm{T}}^{\mathrm{miss}}[1 - \cos\Delta\phi(\ell, \vec{E}_{\mathrm{T}}^{\mathrm{miss}})]}\ , \tag{4.7}$$

where ℓ refers to the charged lepton in the event and $\vec{E}_{\mathrm{T}}^{\mathrm{miss}}$ is the missing transverse energy vector defined in Equation 4.1. For events with electrons, $E_{\mathrm{T}}^{\mathrm{miss}} > 30$ GeV and $m_{\mathrm{T}}^{W} > 30$ GeV is imposed, while for events with muons $E_{\mathrm{T}}^{\mathrm{miss}} + m_{\mathrm{T}}^{W} > 60$ GeV has to be fulfilled. These are typical cuts and similar values were also used for example in Ref. [105]. Since background contributions are rather small (see Tables 5.2 and 5.3), no further cut optimisation was performed.

[3]The p_{T} cut value was further increased for the 2017 and the 2018 data period, to account for different turn-on curves for the same triggers.

[4]Although only four jets are expected in the lepton+jets channel, the number of reconstructed jets can be higher due to initial or final state radiation of gluons.

5. Analysis Strategy

In this chapter, the analysis strategy will be presented[1]. The idea is to perform a binned maximum likelihood fit, using the distributions of one or more variables, to extract the $t\bar{t}$ cross section from data. The definitions of the used signal regions are given in Section 5.1, followed by the variable selection in Section 5.2. The setup of the profile likelihood fit, which is a binned maximum likelihood fit taking into account the effects of systematic uncertainties, will be described in detail in Section 5.3.

5.1. Signal Regions

After the event selection, the events are split according to the lepton flavour into the e+jets and μ+jets channels. This is done in order to check that signal and background components are properly modelled in both channels. At the same time, this splitting allows to perform fit consistency tests (see Section 7.3). In the actual fit, however, both channels will be combined[2]. The events are further split into four orthogonal signal regions which are defined by the jet and b-tag (60% WP) multiplicities. This allows to get some sensitivity to systematic uncertainties, for example uncertainties related to b-tagging or additional radiation. The definitions of the signal regions are summarised in Table 5.1, the event yields are given in the Tables 5.2 and 5.3.

Region	n_{jet}	$n_{b\text{-tag}}$	**Features**	**Usage**
SR1	≥ 4	1	largest background contribution	✓
SR2	4	2	expected signature (for LO production)	✓
SR3	≥ 5	2	gluon radiation	✓
SR4	≥ 4	≥ 3	$t\bar{t}$ + heavy-flavour jets production	✗

Table 5.1.: The definitions of the signal regions. The 60% b-tagging efficiency WP is used. The last column indicates which region is considered in the fit.

[1]This chapter is partially based on the MSc interim report and the ATLAS internal note (v0.6) [104].
[2]This is needed to avoid fit stability problems which occur in a simultaneous fit with many regions and systematic uncertainties.

	SR1	**SR2**	**SR3**	**SR4**
$t\bar{t}$	1680000 ± 80000	461000 ± 23000	457000 ± 23000	36300 ± 1800
Single top	118000 ± 18000	24000 ± 4000	17300 ± 2600	1460 ± 220
$W+$jets	150000 ± 70000	10000 ± 5000	8000 ± 4000	580 ± 280
$Z+$jets	36000 ± 17000	3200 ± 1500	2400 ± 1200	190 ± 90
Diboson	6800 ± 3300	590 ± 280	560 ± 270	53 ± 25
$t\bar{t}V$	5900 ± 600	730 ± 70	2270 ± 230	360 ± 40
$t\bar{t}H$	1640 ± 160	281 ± 28	1100 ± 110	670 ± 70
Multijet	140000 ± 70000	17000 ± 8000	14000 ± 7000	1600 ± 800
Total prediction	2140000 ± 130000	517000 ± 25000	503000 ± 25000	41200 ± 2000
Data	2104763	508387	510606	45551

Table 5.2.: Event yields in all four signal regions in the e+jets channel. Only statistical and normalisation uncertainties are shown.

	SR1	**SR2**	**SR3**	**SR4**
$t\bar{t}$	1940000 ± 100000	531000 ± 27000	526000 ± 26000	41400 ± 2100
Single top	137000 ± 21000	28000 ± 4000	19800 ± 3000	1650 ± 250
$W+$jets	200000 ± 100000	14000 ± 7000	10000 ± 5000	730 ± 350
$Z+$jets	33000 ± 16000	3100 ± 1500	2000 ± 1000	210 ± 100
Diboson	8000 ± 4000	720 ± 350	650 ± 310	58 ± 28
$t\bar{t}V$	6300 ± 600	800 ± 80	2480 ± 250	400 ± 40
$t\bar{t}H$	1730 ± 170	291 ± 29	1180 ± 120	720 ± 70
Multijet	69000 ± 35000	10000 ± 5000	8000 ± 4000	900 ± 400
Total prediction	2400000 ± 150000	588000 ± 29000	570000 ± 27000	46100 ± 2200
Data	2436093	592165	592644	52046

Table 5.3.: Event yields in all four signal regions in the μ+jets channel. Only statistical and normalisation uncertainties are shown.

SR1 gains from the highest number of events but also suffers from the largest background contributions (especially from $W+$jets). SR2 represents exactly the expected signature for LO $t\bar{t}$ production in the lepton+jets channel, while SR3 is sensitive to the radiation of gluons (initial or final state radiation). Since in $t\bar{t}$ events only two b-jets are expected, SR4 (at least three b-tags) is sensitive to the efficiency of misidentifying c-jets, originating mainly from $W \to cs$ decays, as b-jets. Besides that, this region suffers from the mismodelling of $t\bar{t}$ + heavy-flavour jets production. This is the reason for the large discrepancy between data and total prediction (see Tables 5.2 and 5.3). An excess of events in data was also reported previously in Ref. [106]. Thus, a dedicated systematic uncertainty would be needed to be assigned to this region. Because of the mismodelling and the fact that this region is a very small subset (with respect to event yields), SR4 is not considered in the analysis.

Control plots for basic kinematic variables are shown in Figures 5.1 and 5.2 for each of the three considered signal regions (see Table 5.1). The overall agreement between the data and the total prediction is good. However, the jet p_{T} and lepton p_{T} distributions are found to be slightly softer in data in some regions. One reason for that is the mismodelling of the top-quark p_{T} distribution in the MC simulation which was already observed in other analyses, e.g. in Ref. [107]. The reweighting of the top-quark p_{T} distribution to the NNLO QCD + NLO EW calculation at 13 TeV [108] indeed improves the agreement with data but cannot fix the mismodelling completely. The effect of the reweighting is presented in Appendix B. It will be considered as a systematic uncertainty (see Section 6.2.1) in order to account for the mismodelling.

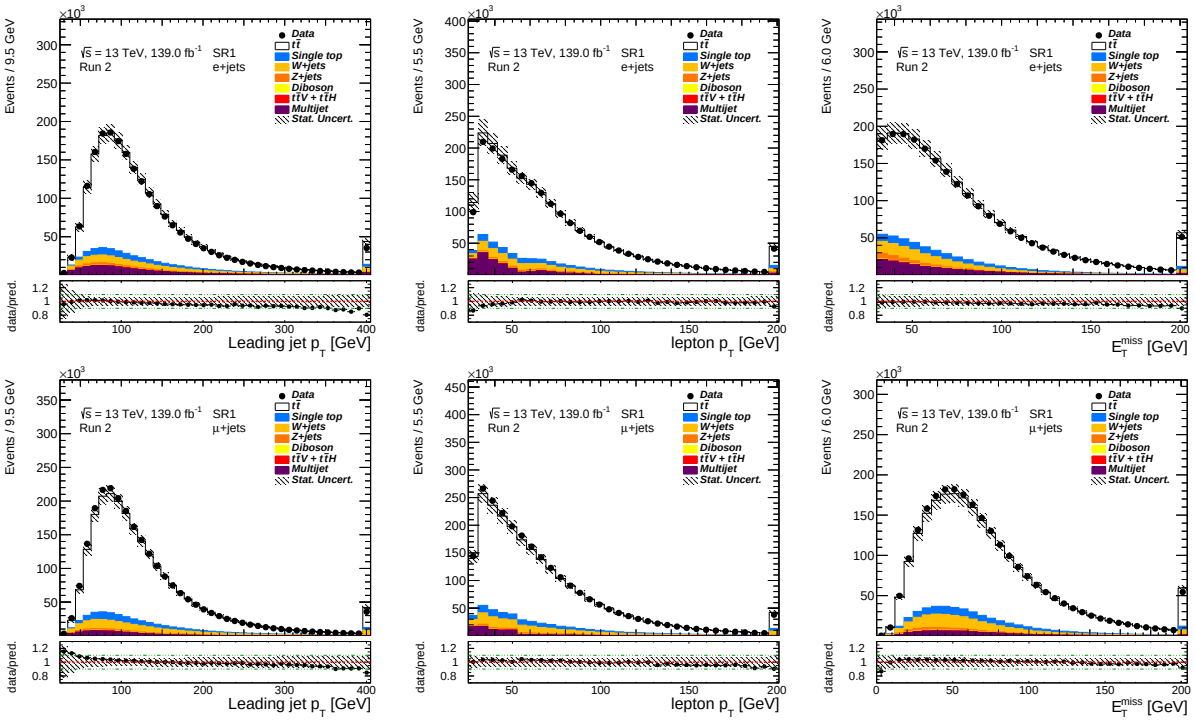

Figure 5.1.: Data/prediction plots for basic kinematic variables in SR1 in the e+jets (top) and the μ+jets channel (bottom). The hashed bands show the statistical and the normalisation uncertainty on each signal and background component. The first and last bin contain underflow and overflow events, respectively.

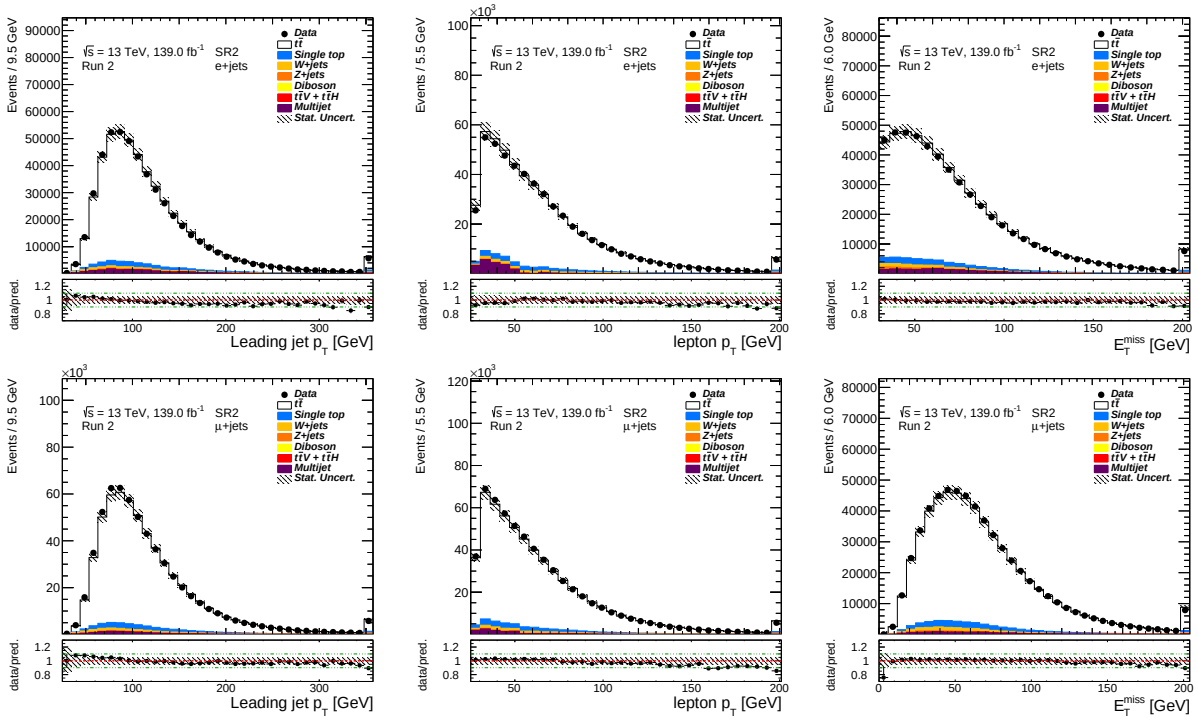

(a) SR2: e+jets (top) and μ+jets channel (bottom).

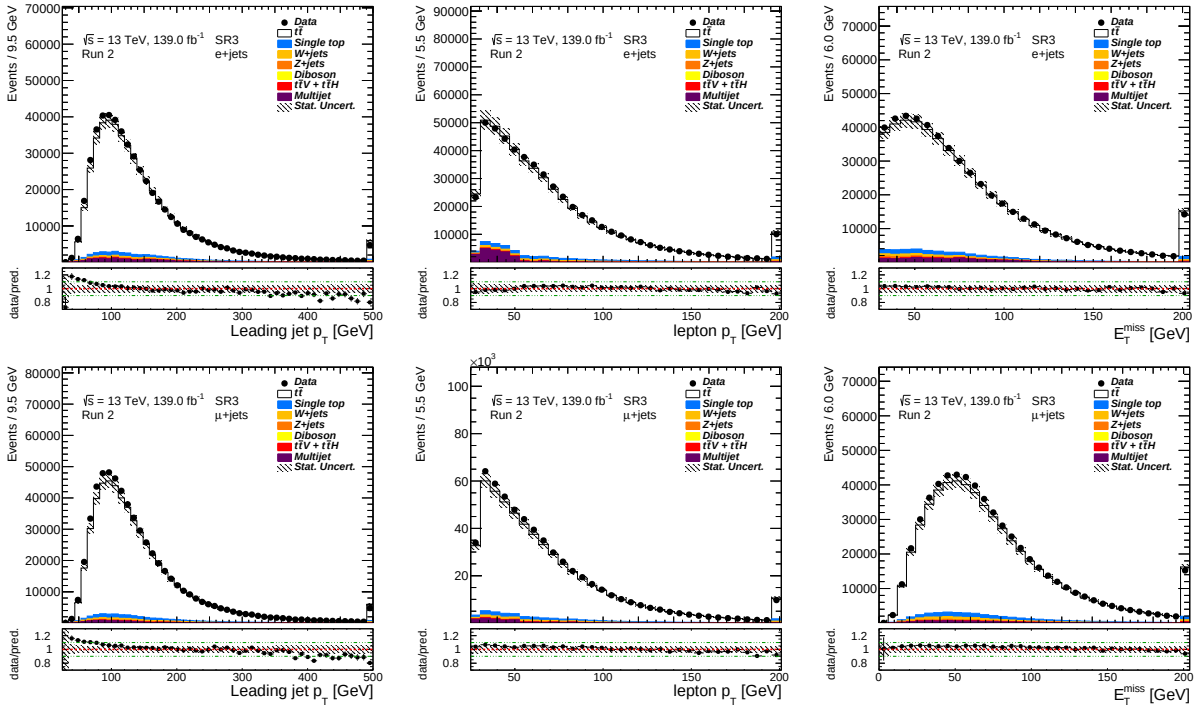

(b) SR3: e+jets (top) and μ+jets channel (bottom).

Figure 5.2.: Data/prediction plots for basic kinematic variables in SR2 (a) and SR3 (b). The hashed bands show the statistical and the normalisation uncertainty on each signal and background component. The first and last bin contain underflow and overflow events, respectively.

5.2. Variable Selection

5.2.1. Separation Power

In principle, variables that are used to extract and measure the signal in data are ideal if they provide separation power, i.e. they behave differently in signal and background events. In order to compare variables with respect to their separation potential, this separation power has to be defined first:

$$s^2 = \frac{1}{2} \sum_{i \in \text{bins}} \frac{\left(n_i^{\text{sig}} - n_i^{\text{bkg}}\right)^2}{n_i^{\text{sig}} + n_i^{\text{bkg}}} \,. \tag{5.1}$$

Here, $n_i^{\text{sig/bkg}}$ is the number of signal/background events in the respective bin of the normalised distribution. In the case that both distributions have no overlap, the above definition would give $s^2 = 100\%$, and if both distributions are the same, it would give $s^2 = 0\%$. One has to be careful because the actual separation value will depend on the chosen binning. Still, this definition helps to get an idea of the discrimination power of a specific variable.

5.2.2. Modelling and Data/Prediction Agreement

A cross section measurement with a badly modelled variable will not give a reliable result. Therefore, only variables which show a good agreement between data and prediction should be taken into account in the variable selection. Also, variables with a large $t\bar{t}$ modelling uncertainty (which is expected to be dominant) should not be considered. To quantify the discrepancy between the nominal and an alternative $t\bar{t}$ model, the following quantity is investigated for each potential variable:

$$D^2_{\text{alt}} = \frac{1}{2} \sum_{i \in \text{bins}} \frac{\left(n_i^{\text{nom}} - n_i^{\text{alt}}\right)^2}{n_i^{\text{nom}} + n_i^{\text{alt}}} \,, \tag{5.2}$$

which is motivated by the binned separation formula (Equation 5.1). Here, $n_i^{\text{nom/alt}}$ is the normalised number of events in bin i in the nominal or the alternative $t\bar{t}$ MC sample. If both distributions of the variable are the same, the discrepancy is zero. This makes the definition useful. The overall $t\bar{t}$ modelling discrepancy D^2 is finally described by the sum of D^2_{alt} over all alternative models. Details on all considered modelling comparisons are given in Section 6.2. Again, the exact discrepancy values D^2, which depend on the chosen binning, are of no relevance. What is important here is to get an idea of the

ranking of these values. This is merely used for the exclusion of variables that are not well suited for the fit. It is found that variables like jet p_{T}, H_{T} (scalar sum of all jet p_{T}), or invariant masses of jet pairs suffer from the largest discrepancy. This also agrees with the observation that their distributions have a rather bad data/prediction agreement. Therefore, such variables are excluded from the selection.

5.2.3. Final Choice

Finally, in each signal region a separate variable was selected. This was done by ordering all considered variables according to their separation power. Several variables, e.g. related to the distance between objects or the b-tagging, were taken into account (see Appendix C). As already mentioned, variables with a very large $t\bar{t}$ modelling discrepancy were discarded. Then, these ordered lists were checked and the first variable with a reasonable agreement between data and prediction was chosen. The selected set of variables, together with their separation power in different channels, is shown in Table 5.4. Their distributions are compared between the signal and the combined background in Figure 5.3. For comparison purposes, some exemplary variables with large modelling discrepancy values D^2 are additionally presented in Table 5.5.

Variable	**Region**	**e+jets**	**μ+jets**	**[#Bins, min, max]**
Aplanarity	SR1	1.0%	1.0%	[20, 0, 1]
m_{lj}^{min} [GeV]	SR2	3.2%	3.0%	[30, 0, 300]
$\Delta R_{bjj,\mathrm{max}\ p_{\mathrm{T}}}^{\mathrm{avg}}$	SR3	1.1%	1.2%	[50, 0, 5]

Table 5.4.: Separation power between signal and combined background of the selected variables for the fit. The shown values depend on the chosen binning.

The aplanarity of the jets, exploited in SR1, was found to have discriminating power already in previous analyses (e.g. in Ref. [39]). It is defined by $\frac{3}{2}\lambda_3$, where λ_3 is the smallest eigenvalue of the sphericity tensor

$$S^{\alpha\beta} = \frac{\sum_{i\in\mathrm{jets}} p_i^{\alpha} p_i^{\beta}}{\sum_{i\in\mathrm{jets}} |p_i|^2} \,. \tag{5.3}$$

Here, p_i^{α} is one of the three components of the ith jet momentum. The minimal lepton-jet mass m_{lj}^{min}, calculated as the smallest invariant mass among all lepton-jet pairs, is used in SR2. It is correlated with the mass of the lepton and the closest b-jet, which then again is correlated with the mass of the leptonically decaying top quark, thus explaining its separation power. An angular variable, denoted as $\Delta R_{bjj,\mathrm{max}\ p_{\mathrm{T}}}^{\mathrm{avg}}$, is exploited in SR3.

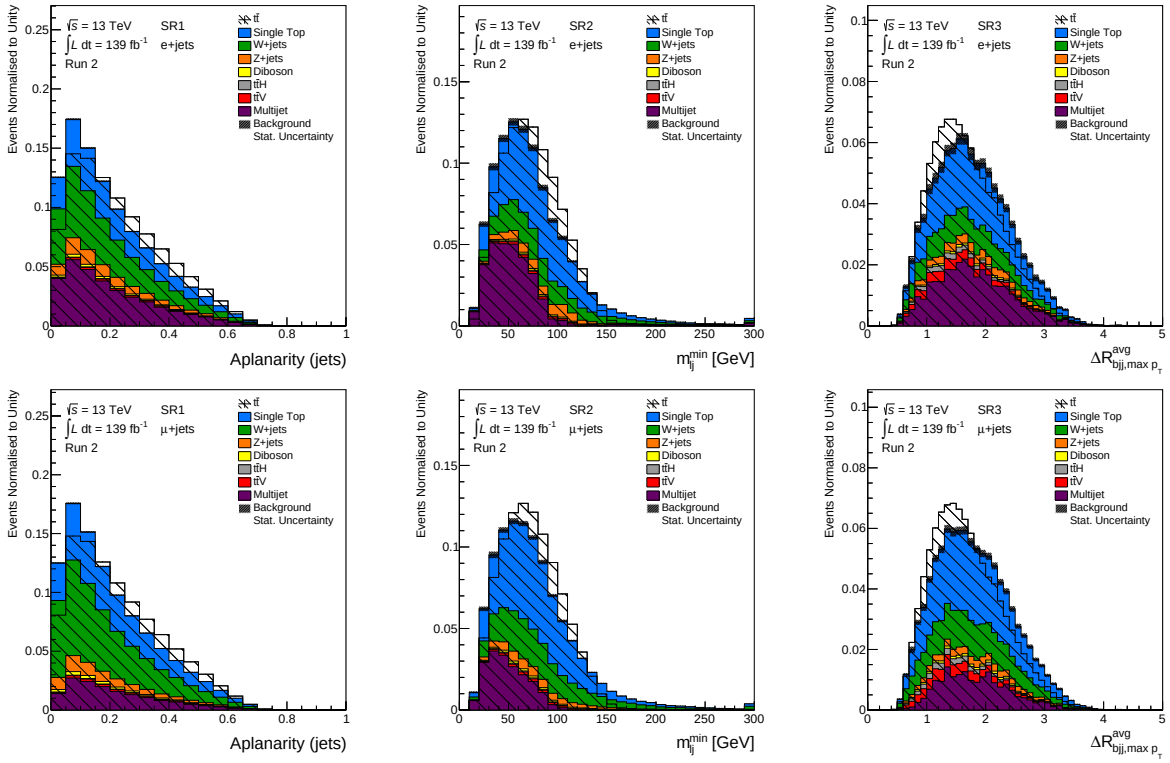

Figure 5.3.: Distributions of the selected variables in the e+jets (top) and the μ+jets channel (bottom). The $t\bar{t}$ and the combined background distributions are both normalised to unity. Only the statistical uncertainty on the total background contribution is shown. The first and last bin contain underflow and overflow events, respectively.

	e+jets			μ+jets			
Variable	**SR1**	**SR2**	**SR3**	**SR1**	**SR2**	**SR3**	**[#Bins, min, max]**
Aplanarity	0.7	0.9	1.3	0.7	0.8	1.0	[20, 0, 1]
m_{lj}^{min} [GeV]	1.8	1.1	2.6	1.6	0.8	2.2	[30, 0, 300]
$\Delta R_{bjj,\text{max } p_{\text{T}}}^{\text{avg}}$	1.4	3.6	2.6	1.3	3.2	2.5	[50, 0, 5]
Leading jet p_{T} [GeV]	8.1	5.1	11.6	7.7	4.9	10.7	[50, 25, 500]
H_{T} [GeV]	8.3	8.0	11.9	8.0	8.0	12.0	[50, 100, 1000]
m_{jj}^{min} [GeV]	13.0	8.9	13.0	13.1	9.1	10.9	[50, 0, 200]

Table 5.5.: Modelling discrepancy values D^2 (in units of 10^{-4}) of the selected variables and of some exemplary jet p_{T} related variables. The latter ones have the largest discrepancy in all regions which was the reason for their early exclusion in the variable selection.

It is defined as the average distance between the jets in the subsystem consisting of a b-jet and two other jets with maximum total p_{T} among all such three-jet permutations. The motivation here is the fact that this subsystem of jets is likely to originate from the hadronically decaying top quark, while in background events it is likely to be a random combination. Apart from that, $\Delta R^{\mathrm{avg}}_{bjj,\mathrm{max}\ p_{\mathrm{T}}}$ is an angular variable and therefore is expected to be less sensitive to the jet energy scale uncertainty as well as to ISR and FSR effects. Figure 5.4 shows the good agreement between the data and the total prediction for the three selected variables.

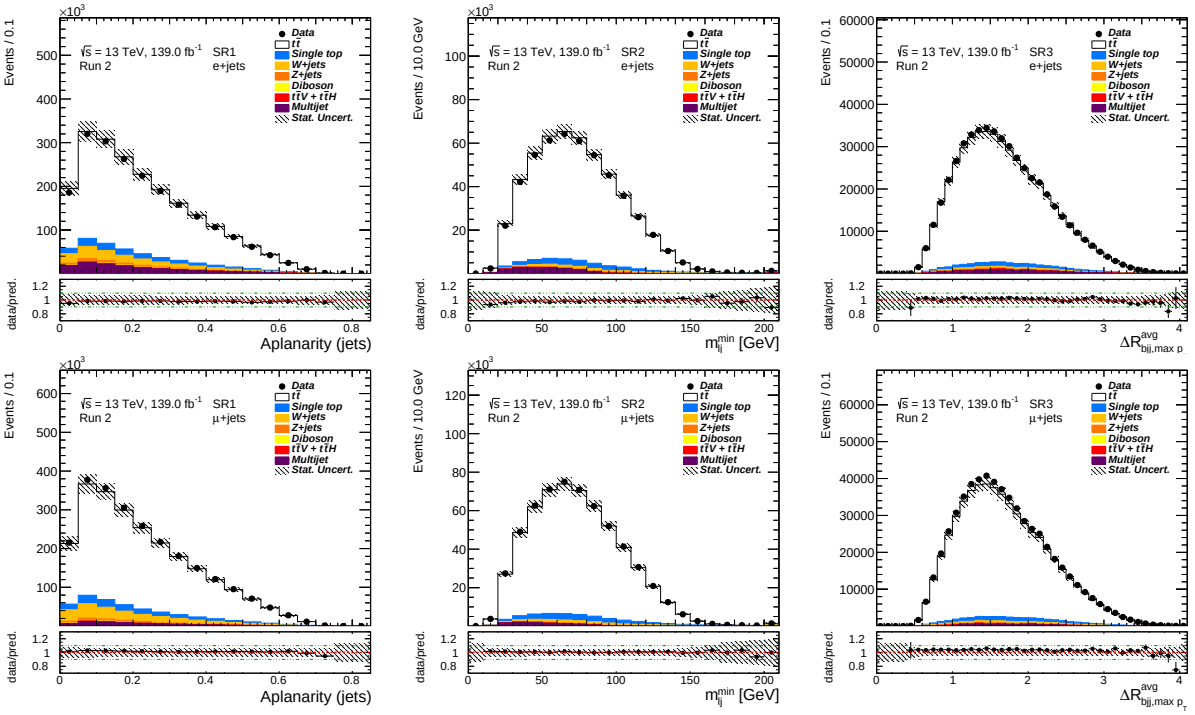

Figure 5.4.: Data/prediction plots for the selected variables in the e+jets (top) and the μ+jets channel (bottom). The hashed bands show the statistical and the normalisation uncertainty on each signal and background component. The first and last bin contain underflow and overflow events, respectively.

As one can see in Table 5.4, the discrimination power in SR1 and SR3 is not very large. However, it was finally found that in this analysis actually no gain is expected from the separation potential. The usage of a neural network was investigated previously [104] but the expected uncertainty on the $t\bar{t}$ cross section could not be improved. Still, variables with separation potential (even if it is not large) are in principle good candidates. Since the fit with the variables summarised in Table 5.4 already achieved a very good precision, no attempt was made to further optimise the variable selection.

5.3. Profile Likelihood Fit

The parameter of interest in the binned maximum likelihood fit will be the signal strength $\mu = \sigma_{t\bar{t}}/\sigma_{t\bar{t}}^{\mathrm{SM}}$ which is the ratio between the measured $t\bar{t}$ cross section and the SM prediction $\sigma_{t\bar{t}}^{\mathrm{SM}} = 831.76$ pb. To perform the fit, the `TRExFitter` software package [109] is used which includes the `Histfactory` tools [110]. It allows to define signal and also control regions which can be fitted simultaneously. Furthermore, it provides many features, for example smoothing of histograms, pruning, and symmetrisation of systematic uncertainties. `TRExFitter` combines all the given histograms to perform a profile likelihood fit. The likelihood is basically a product of Poisson probability terms for all the bins. The signal prediction is scaled by μ which will be extracted from the fit. Systematic uncertainties are incorporated into the likelihood function via nuisance parameters θ, where $\theta = 0$ corresponds to the nominal MC prediction and $\theta = \pm 1$ corresponds to the respective $\pm 1\sigma$ variation. The likelihood takes the following form:

$$L = \prod_{i \in \mathrm{bins}} \mathrm{Pois}(n_i | \mu \cdot s_i(\vec{\theta}) + b_i(\vec{\theta})) \times \prod_j C(\theta_j | \theta_j^0, \sigma_{\theta_j^0}) \,. \tag{5.4}$$

Here, n_i is the observed number of events in bin i, while s_i and b_i are the predicted numbers of signal and background events. The last term is the constraint term for the systematics, where θ_j^0 is the nominal value and $\sigma_{\theta_j^0}$ is the prior estimate for the uncertainty. Here, all the nuisance parameters (NPs) are constrained by a Gaussian prior term with $\theta_j^0 = 0$ and $\sigma_{\theta_j^0} = 1$. The $\pm 1\sigma$ variations of each systematic uncertainty need to be provided in form of histograms. Then, interpolation is used within `TRExFitter` in order to describe each systematic effect in a continuous way. For this purpose, each NP θ is split into a shape and a normalisation component. The shape effect is described via linear interpolation, while the normalisation effect is described via exponential interpolation. The exponential interpolation paired with the Gaussian prior term is equivalent to a log-normal constraint of the normalisation component of θ, which prevents negative event yields.

Additionally, it has to be considered that the MC histograms for background and signal prediction, which are used in the fit, can be affected by statistical uncertainties. To account for them, for each bin a common nuisance parameter γ_i is introduced which scales the total nominal MC prediction. Therefore, different from the previous nuisance parameters, the nominal value is $\gamma_i = 1$. A Poisson constraint term is used taking into account the total statistical uncertainty in the specific bin [110].

All the NPs ($\vec{\theta}$ and $\vec{\gamma}$) are treated as uncorrelated in the likelihood but correlations can be determined with the fit. The fit is performed by constructing the negative log-likelihood function which is subsequently minimised using algorithms implemented in `MINUIT` [111].

During the fit, all NPs and the parameter of interest (the signal strength μ) are allowed to vary. Here, μ is a free-floating parameter in the likelihood whereas the variations of NPs are limited by their respective constraint terms. Finally, if the post-fit value of a NP vary from the initial value, it means that the data has power to pull the NP. If the post-fit uncertainty is smaller than $\pm 1\sigma$, it means that the data has statistical power to constrain the corresponding systematic uncertainty.

6. Systematic Uncertainties

In this chapter, all systematic uncertainties considered in the analysis will be described[1]. The experimental uncertainties, which are identical for all simulated signal and background processes, will be explained in Section 6.1. Theoretical uncertainties, especially on $t\bar{t}$ modelling, will be discussed in Section 6.2. Since alternative MC samples are only available with fast detector simulation (AFII), they are always compared to the nominal AFII samples. The relative differences are then propagated to the nominal samples generated with full simulation in order to estimate the respective modelling uncertainty. Statistical uncertainties in the MC samples will be described in Section 6.3. Finally, the concept of pruning, smoothing, and symmetrisation of systematic uncertainties will be briefly summarised in Section 6.4.

6.1. Experimental Uncertainties

6.1.1. Luminosity

All simulated events in each MC campaign are scaled to the respective integrated luminosity in order to match the expected number of events. The integrated luminosity is 36.2 fb^{-1} for the combined 2015+2016 dataset, 44.3 fb^{-1} for the 2017 dataset, and 58.5 fb^{-1} for the 2018 dataset. The uncertainties are 2.1%, 2.4%, and 2.0%, respectively. The values are derived with methods described in Ref. [112] and by using the LUCID-2 detector for the luminosity measurements [102]. For the combined Run II dataset (139 fb^{-1}), the luminosity uncertainty is 1.7% [112].

6.1.2. Pile-Up

As described in Section 4.2, all MC samples are reweighted in order to match the level of pile-up observed in data [113]. Uncertainties related to the pile-up scale factors have to be propagated into the fit. An up and a down variation are provided.

[1]This chapter is partially based on the MSc interim report and the ATLAS internal note (v0.6) [104].

6.1.3. Jet Energy Scale

The jet energy scale (JES) and its uncertainty are derived from test-beam data, collision data, and MC simulation with methods described in Ref. [76]. Jets are calibrated in several stages. First, they are corrected to point back to the identified hard-scattering vertex. Then, an area-based pile-up subtraction is applied. The jet four-vector is then calibrated by applying p_{T} and η dependent corrections derived from simulation. Further corrections are applied to reduce the dependency of the energy measurement on the jet structure, energy leakage effects are also corrected. Finally, a residual correction is applied on jets in data. For the calibration, dijet, multijet, and vector boson+jets events are used, depending on the detector region and the jet p_{T}. The JES uncertainty is split into several categories: The in-situ calibration method, MC and detector simulation, modelling of pile-up effects, calorimeter response, jet flavour composition, jet flavour response, η intercalibration, b-jet energy scale, punch-through correction, and high-p_{T} jets [76]. The derived uncertainties are parametrised as a function of jet p_{T} and η. A reduction scheme is used which finally gives a set of 29 nuisance parameters (each with an up and a down variation).

6.1.4. Jet Energy Resolution

The jet energy resolution (JER) and its uncertainty are determined in dijet, multijet, and Z/γ+jet events as a function of jet p_{T} and η, using methods similar to those used in Refs. [114, 115]. The total uncertainty is described with 117 nuisance parameters. An eigenvector decomposition is used which results in a smaller set of 7 NPs. The uncertainties on the JER are then propagated by smearing the jets in the MC with a Gaussian distribution with $\sigma^2_{\mathrm{smear}} = (\sigma_{\mathrm{nom}} - \sigma_{\mathrm{NP}})^2 - \sigma^2_{\mathrm{nom}}$, where σ_{nom} is the nominal JER and σ_{NP} is the 1σ variation of the JER uncertainty component. Finally, if the JER in data is lower than in the MC, the respective difference is taken as an additional uncertainty. Thus, in total 8 NPs are taken into account for the JER uncertainty.

6.1.5. Jet Vertex Tagging

Scale factors are utilised in order to account for differences between the JVT efficiency in simulation and in data. They are derived in $Z(\rightarrow \mu^+\mu^-) + \mathrm{jets}$ events using the tag-and-probe method, similar as described in Ref. [77]. Both an up and a down variation are provided which are propagated to the distributions used in the fit.

6.1.6. B-Tagging

B-tagging algorithms need to be calibrated in order to achieve a match between the performances in simulation and in data. Therefore, corrective scale factors are derived from data [116–118]. The b-tagging and c-tagging efficiencies as well as the mistagging rates of light-flavour jets are measured and scale factors are calculated as the ratios between the efficiencies (or mistagging rates) in data and in simulation. In general, the scale factors depend on jet p_{T} and η. Their uncertainties are propagated into the analysis via 45 NPs for b-jets and 20 NPs for c- and light-flavour jets, respectively.

6.1.7. Electrons and Muons

Corrective scale factors are applied for electrons and muons in order to account for discrepancies between simulation and data with respect to reconstruction, isolation, identification, and trigger efficiencies. These corrections and their uncertainties are estimated using the tag-and-probe method with leptons from Z boson, W boson (only for electrons), and J/Ψ decays, as described in Refs. [72, 73]. The lepton scale factors also correct differences regarding the lepton momentum scale and resolution. The respective corrections are derived by investigating the invariant mass spectrum in $Z \to l^+l^-$ and $J/\Psi \to l^+l^-$ decays [73, 119]. For muons, uncertainties in the inner detector and the muon spectrometer are considered separately.

6.1.8. Missing Transverse Energy

Several terms enter the calculation of the missing transverse energy (see Equation 4.1). Therefore, uncertainties related to the reconstructed objects have to be propagated to the uncertainty on $E_{\mathrm{T}}^{\mathrm{miss}}$. The systematic uncertainty on the soft term is estimated in $Z \to \mu^+\mu^-$ events by exploiting the transverse momentum balance between this term and all reconstructed objects [79]. All these uncertainties are finally combined into the scale and resolution uncertainty of the missing transverse energy. The resolution component is further split into two subcomponents for the parallel and perpendicular projection of the $E_{\mathrm{T}}^{\mathrm{miss}}$ vector.

6.1.9. Multijet Background

As described in detail in Section 4.3, real and fake lepton efficiencies are used to estimate the multijet background from data. These efficiencies can be parametrised as a function of the leading jet p_{T}, lepton p_{T}, lepton η, etc. Table 6.1 presents the used parametrisations

in 1 b-tag (SR1) and 2 b-tag (SR2, SR3) regions, separately for the e+jets and μ+jets channels. The choice of a parametrisation was made by investigating basic kinematic distributions, e.g. the lepton p_{T}, leading jet p_{T}, or lepton η [104]. Parametrisations leading to either unphysical distributions or negative event yields were discarded. To estimate the uncertainty on the shape of the distributions used in the fit, an alternative parametrisation is utilised. Additionally, a normalisation uncertainty of 50% is applied, which is a typical conservative value and was also used previously in Ref. [105]. The shape and normalisation uncertainties are treated separately and are both decorrelated between all three regions as well as between e+jets and μ+jets events.

	1b, e+jets	**1b, μ+jets**	**2b, e+jets**	**2b, μ+jets**
nominal	$\Delta\phi$	$p_{\mathrm{T}}, \Delta\phi$	jet $p_{\mathrm{T}}, \Delta R$	$p_{\mathrm{T}}, \Delta\phi$
alternative	jet p_{T}	$\eta, p_{\mathrm{T}}, \Delta\phi$	jet p_{T}	η, jet $p_{\mathrm{T}}, \Delta\phi$

Table 6.1.: The nominal and alternative parametrisations of real and fake lepton efficiencies in different regions. Here, $\Delta\phi$ refers to the azimuthal angle between the lepton and the $E_{\mathrm{T}}^{\mathrm{miss}}$ vector, p_{T} and η refer to the lepton p_{T} and η, and ΔR is the distance between the lepton and the closest jet.

6.2. Theoretical Uncertainties

6.2.1. Top-Quark p_{T} Reweighting

The top-quark p_{T} is mismodelled in the $t\bar{t}$ MC simulation (only NLO precision) which results in a mismodelling of the jet and lepton p_{T} distributions (see Section 5.1). As described in Appendix B, the reweighting to the NNLO QCD + NLO EW calculation slightly improves the agreement with data. The effect of this reweighting on the $t\bar{t}$ sample is added as a systematic uncertainty in order to take the mismodelling into account. To ensure that there is no double counting of uncertainties, all distributions used to evaluate the $t\bar{t}$ modelling and PDF uncertainties are reweighted to match the NNLO top-quark p_{T} distribution on MC truth level. They are then compared to the distributions in the reweighted Powheg-Box + Pythia 8 AFII sample (for reasons of simplicity, only called *nominal* in the following) for the uncertainty estimation.

6.2.2. Parton Showering and Hadronisation

To evaluate the uncertainty on the parton shower and hadronisation modelling in the $t\bar{t}$ simulation, the nominal sample which uses Pythia 8 is compared to an alternative

sample using HERWIG 7. The ME generator in both samples is POWHEG-BOX. The same procedure is also applied for the single top-quark background and a separate NP is added to the fit. To avoid too large constraints, this source of uncertainty is split into several components for $t\bar{t}$ events. The resulting uncertainty on the shape of the used distributions in the fit is treated as uncorrelated between all three regions. The uncertainty on the normalisation, however, is split into two uncorrelated components. The first component takes into account the acceptance uncertainty of 2.1%, and the second component represents the migration of events between the three regions (while dropping the overall acceptance effect). The motivation for keeping the normalisation effects correlated is the fact that the acceptance is mainly determined by the p_{T} cuts which are identical in all three regions. The migration effect is considered separately to prevent the propagation of its large constraint to the acceptance uncertainty.

6.2.3. Initial State Radiation (ISR)

In order to estimate the uncertainty originating from ISR modelling in the $t\bar{t}$ simulation, three variations are taken into account and are introduced as separate nuisance parameters into the fit. One NP represents the up and down variations of the `Var3c` parameter of the `A14` tune [89] which are obtained by reweighting the nominal $t\bar{t}$ sample. This reweighting corresponds to a variation of the strong coupling considered in ISR (α_s^{ISR}). Both variations are symmetrised and added as one systematic uncertainty. The two other considered uncertainties are estimated from the variations of the renormalisation and factorisation scales, $\mu_{\mathrm{R}} \times (2, 0.5)$ and $\mu_{\mathrm{F}} \times (2, 0.5)$, with respect to their nominal values. They are also obtained by a reweighting procedure. Again, both the up and the down variation of each of the two scales are symmetrised and are finally added as two separate systematic uncertainties. The described strategy is also used for the single top-quark background and three separate NPs are added to the fit.

6.2.4. Final State Radiation (FSR)

The impact of the $t\bar{t}$ FSR modelling uncertainty is evaluated by reweighting the nominal $t\bar{t}$ sample. The two variations $\mu_{\mathrm{R}}^{\mathrm{FSR}} \times 0.5$ and $\mu_{\mathrm{R}}^{\mathrm{FSR}} \times 2$ are considered. This reweighting corresponds to a variation of the strong coupling considered in FSR (α_s^{FSR}). Both variations are symmetrised and are added as one systematic uncertainty. The same procedure is also applied to estimate the FSR uncertainty in the single top-quark background. Again, the respective uncertainty is described with a separate NP in the fit.

6.2.5. PDF Uncertainties

PDF uncertainties for the $t\bar{t}$ signal are evaluated using the `PDF4LHC15` error set which consists of 30 NPs [120]. Again, internal reweighting of the nominal $t\bar{t}$ sample is used. It is reweighted to the `PDF4LHC15` central prediction as well as to its error set, and the symmetrised uncertainties are propagated to the distributions of the variables used in the fit. The PDF uncertainties for the single top-quark background are neglected because of their small impact.

6.2.6. Single Top Wt-Channel

One of the largest modelling uncertainties for single top-quark production originates from the modelling of the Wt-channel. The main LO production mode on partonic level is $gb \to tW^-$. Main NLO corrections arise, for example, from $gg \to tW^-\bar{b}$ where one gluon splits into a virtual $b\bar{b}$ pair. But such diagrams can also be interpreted as LO $t\bar{t}$ production where the $\bar{t}$ immediately decays into $W^-\bar{b}$. Their contributions are relatively large and cause problems in perturbative calculations. Therefore, the $t\bar{t}$ diagrams need to be removed. Two techniques have been developed. The diagram removal (DR) scheme removes the diagrams at amplitude level, and the diagram subtraction (DS) scheme subtracts the diagrams at the level of matrix elements [121]. The Wt sample with the DR scheme is used as the nominal sample and the relative difference between the DR and the DS sample is taken as a symmetrised systematic uncertainty.

6.2.7. $W+$jets CKKW Scale

Within Sherpa, parton showers and matrix elements are matched to each other using the CKKW scheme [122] with a default scale of 20 GeV. MC event weights are used to reweight the $W+$jets events to a scale of 15 and 30 GeV. In order to estimate the uncertainty due to the chosen scale, the symmetrised effect of both variations is propagated to the nominal distribution. Only the impact on the shape is taken into account.

6.2.8. $W+$jets Resummation Scale

To evaluate the uncertainty originating from the chosen scale for the resummation of soft gluon emission in the $W+$jets simulation, the scale (also called QSF parameter) is varied by a factor of 0.5 and 2 via reweighting. The symmetrised effect of both variations is propagated to the nominal distribution. Only the impact on the shape is taken into account.

6.2.9. $W+$jets Renormalisation and Factorisation Scale

To estimate the uncertainty due to missing higher order corrections in the $W+$jets background simulation, six variations of the renormalisation and factorisation scale are provided: $(\mu_{\mathrm{R}}, \mu_{\mathrm{F}}) \times (0.5, 0.5), (1, 0.5), (0.5, 1), (2, 1), (1, 2), (2, 2)$. MC generator event weights are used to create $W+$jets distributions for each of the six scenarios. Finally, the envelope of the six distributions (with respect to the nominal distribution) is determined. The difference between the envelope and the nominal distribution is symmetrised and the resulting effect on the shape is taken as a systematic uncertainty.

6.2.10. MC Background Normalisation

Normalisation uncertainties are assigned to all MC background distributions in order to take into account the theoretical uncertainties on the predicted cross sections as well as the uncertainties on the acceptances. For the single top-quark background, acceptance effects are already taken into account in the modelling uncertainties. Therefore, the uncertainty on the predicted cross section is used. The total uncertainty (PDF+α_s and QCD scale uncertainties) on the cross section for the s-channel is 3.9%, for the t-channel 4.2%, and for the Wt-channel it is 5.4% [93–95]. To be conservative, the largest uncertainty of 5.4% is applied on the total single top-quark contribution.

For the $W+$jets background, no alternative generators are available for the estimation of the acceptance uncertainty. Instead, the effect on the normalisation originating from the variation of the CKKW, QSF, and renormalisation/factorisation scales is considered. This results in an uncertainty of 45.2% in SR1, 42.5% in SR2, and 50.5% in SR3. The uncertainty is finally decorrelated between the 1 b-tag (SR1) and 2 b-tag (SR2, SR3) regions in order to account for differences in the flavour composition.

The theoretical cross section uncertainty for $t\bar{t}Z$ production is 12.0%, for $t\bar{t}W$ it is 13.3%, and for $t\bar{t}H$ it is 9.9%. These values include uncertainties resulting from scale variations as well as PDF+α_s uncertainties [99]. For the estimation of acceptance uncertainties, alternative generators are needed which are not available for the $t\bar{t}V$ processes. But since these backgrounds are very small, the normalisation uncertainty will not have any impact on the measurement. Based on the quoted values, a normalisation uncertainty of 13.3% is assigned to the combined background $t\bar{t}H$+$t\bar{t}V$ (denoted as $t\bar{t}X$).

The remaining backgrounds (diboson, $Z+$jets) are also combined (other background). Due to the similarity between $Z+$jets and $W+$jets events, and the fact that the diboson background has a very small contribution, the found values for the $W+$jets uncertainty are also utilised here. Based on these values, a normalisation uncertainty of 50% is applied.

6.3. Monte Carlo Statistical Uncertainties

MC statistical uncertainties originate from the fact that only finite numbers of generated events are used to create the histograms for the fit. As already described in Section 5.3, they enter the fit as nuisance parameters for each individual bin which are shared among signal and background sources [123]. In contrast to the other NPs for systematic uncertainties, they are constrained with a Poisson prior distribution and are decorrelated among different bins [110].

6.4. Pruning, Smoothing and Symmetrisation

To reduce the complexity and increase the speed and stability of the fit, pruning is applied which removes systematics with negligible effects. Systematic uncertainties which have an effect smaller than 0.05% on the normalisation are only considered for the shape effect. Uncertainties with an effect smaller than 0.1% on the shape[2] are only considered for the normalisation effect. If both, the shape and the normalisation effect are small, the systematic uncertainty is removed for the respective distribution. MC statistical uncertainties are removed from the fit in case the uncertainty in the specific bin is lower than 0.1%. Smaller threshold values were also tested but no impact on the expected cross section uncertainty was observed. To remove the effect of statistical fluctuations in the provided systematic uncertainties, the smoothing option within `TRExFitter` is used. Uncertainties which are estimated via reweighting (PDF, b-tagging, ...) are not smoothed. The exceptions are the uncertainties on the multijet and the $W+$ jets shape, which suffer a lot from statistical fluctuations. Also, the distributions used to estimate the FSR uncertainties (via reweighting) are smoothed because some events have very large weights and thus introduce statistical fluctuations into the distributions. The smoothed distributions are finally utilised to describe the respective uncertainties. For uncertainties where both the up and the down variation are provided, two-sided symmetrisation is used[3]. This means that in each bin i the systematic uncertainty is described by $(n_i^{\text{up}} - n_i^{\text{down}})/2$. If either only the up or the down variation is available (shower modelling, JER, ...), one-sided symmetrisation is applied. In this case, the mirrored distribution of the given up/down variation is used to describe the down/up variation. All described systematic uncertainties, including the number of NPs that are left after applying the pruning, are summarised in Table 6.2.

[2] This means that the pure shape effect in each bin is below this threshold.

[3] The symmetrisation helps to prevent kinks in the interpolation. This ensures that the interpolation effect is differentiable which is an important requirement for a successful minimisation procedure.

Systematic Uncertainty	Components	Effect	After Pruning
Physics Objects			
Electrons	7	SN	6
Muons	15	SN	4
Jet energy scale	29	SN	16
Jet energy resolution	8	SN	8
Jet vertex tagging	1	SN	1
Missing transverse energy	3	SN	3
b-tagging efficiency	45	SN	42
c-tagging efficiency	20	SN	18
light-flavour jet mistagging rate	20	SN	14
Background Model			
Single top normalisation	1	N	1
Single top DR/DS scheme	1	SN	1
Single top shower & hadronisation	1	SN	1
Single top ISR modelling	3	SN	3
Single top FSR modelling	1	SN	1
$W+$jets normalisation	2	N	2
$W+$jets CKKW scale	1	S	0
$W+$jets resummation scale	1	S	0
$W+$jets $\mu_{\mathrm{R}}, \mu_{\mathrm{F}}$ variation	1	S	1
$t\bar{t}X$ normalisation	1	N	1
Other background normalisation	1	N	1
Multijet normalisation	6	N	6
Multijet shape	6	S	5
Signal Model			
Top-quark p_{T} reweighting	1	SN	1
$t\bar{t}$ ISR modelling	3	SN	3
$t\bar{t}$ FSR modelling	1	SN	1
$t\bar{t}$ shower & hadronisation	5	SN	5
$t\bar{t}$ PDF	30	SN	17
Other			
MC statistics	37	per bin	31
Pile-up reweighting	1	SN	1
Luminosity	1	N	1

Table 6.2.: Overview of all systematic uncertainties included in the fit. Each component in each category is represented by one nuisance parameter. Some systematics only effect the shape (S) or the normalisation (N) of the distributions, others effect both. In contrast to that, the NPs representing the MC statistical uncertainty only effect one specific bin. The table also shows how many NPs are left in each category after the pruning.

7. Results

In this chapter, the results of the fit will be presented. As already described in Section 5.1, the electron and muon channels are combined. The pre-fit distributions of the used variables in all signal regions are shown in Figure 7.1. These distributions with the shown binning directly enter the fit[1]. As one can see, the agreement between the total prediction and the data is very good in SR1 and SR2. Only in SR3 the agreement is slightly worse. However, the overall discrepancy is related almost only to the normalisation and not to the shape. All systematic uncertainties remaining after the applied pruning (see Table 6.2) are taken into account in the shown uncertainty bands.

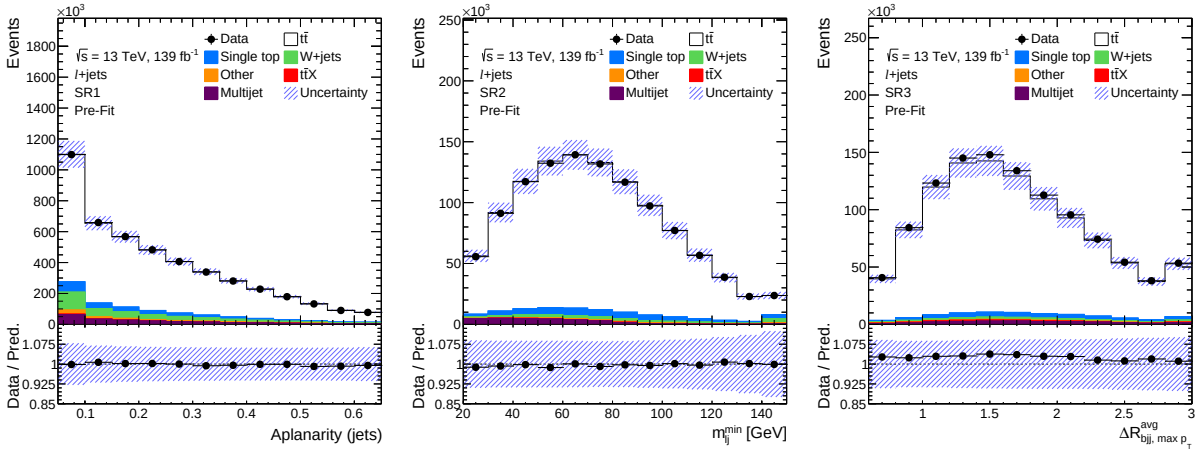

(a) SR1 *(b)* SR2 *(c)* SR3

Figure 7.1.: Pre-fit distributions of the chosen variables for the fit in all three signal regions. Electron and muon channels are combined. The total uncertainty (stat. + syst.) is shown. The first and last bin contain underflow and overflow events, respectively.

[1]The binning was slightly changed compared to previous plots in order to reduce extreme constraints and pulls of nuisance parameters.

7.1. Asimov Fit

Before fitting the observed data, the fit configuration has to be validated. A very useful test is the so-called Asimov fit where the combination of the predicted background and signal, assuming a signal strength of $\mu = 1$, is used as pseudo data. The nominal distributions are used to create this dataset, i.e. all the NPs are set to zero. One important check is to make sure that the fitted value of μ corresponds to the input value. Furthermore, the post-fit values (pulls) of all NPs have to be close to zero in the Asimov fit. Their post-fit uncertainties, however, can be smaller than their pre-fit uncertainties because the data can potentially constrain the related systematic uncertainty. When fitting this pseudo dataset, one can indeed extract the input signal strength. The result is $\mu = 1.000^{+0.043}_{-0.042}$, which corresponds to an expected uncertainty of 4.3%. This is the total uncertainty, i.e. it includes both the statistical and the systematic uncertainty. The post-fit values of the NPs are shown in Figure 7.2 and are all centred around zero, as they should be. No significant constraints are observed for the experimental uncertainties. However, some modelling uncertainties are constrained, especially the $t\bar{t}$ FSR and the parton shower uncertainties. This was investigated and it was found that these constraints mainly originate from the shape variation and not from the acceptance effect, because the latter one is strongly correlated with the signal strength. Furthermore, the potential migration of events between the three signal regions can cause additional constraints. Histograms showing the effects of $t\bar{t}$ modelling uncertainties on the distributions of the fit variables can be found in Appendix D. Considering these effects and the large statistical power of the fit, the constraints on modelling uncertainties can be understood. They arise because the uncertainties are very large, and probably too conservative, and do not originate from artificial features of the fit.

In order to check the fit stability, the likelihood scan of the signal strength μ is shown in Figure 7.3a. It is created by iterating over several values of μ and performing the fit to Asimov data while μ is held constant. The resulting (minimised) negative log-likelihood value is plotted for each fit after subtracting the value obtained in the minimum. The likelihood curve has a very smooth and parabolic shape which provides proof that the fit configuration is very stable and the results are reliable. Furthermore, the values of μ where the negative log-likelihood changes by 0.5 with respect to the minimum agree very well with the obtained uncertainties in the actual fit.

To get an idea which NPs have the largest impact on the fitted signal strength, their ranking is investigated, which is shown in Figure 7.3b. In the ranking procedure the fit is performed four times for each NP. In each of the four fits, the respective NP is set constant to either $\hat{\theta} \pm \sigma_{\theta_0}$ (pre-fit impacts) or $\hat{\theta} \pm \hat{\sigma}_\theta$ (post-fit impacts), where $\hat{\theta}$ is

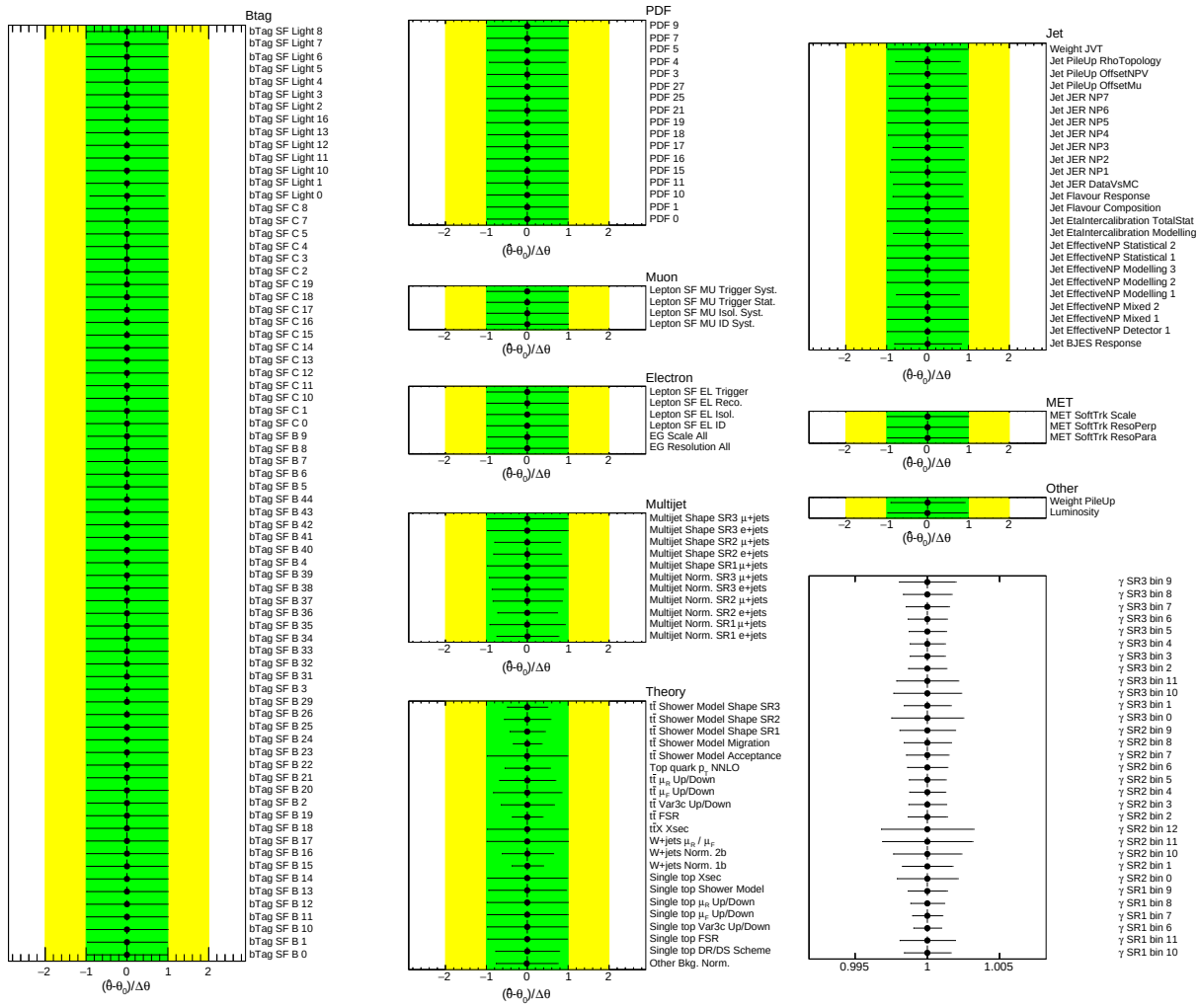

Figure 7.2.: Pulls and constraints of all nuisance parameters in the Asimov fit. The green band represents the 1σ region, corresponding to the prior uncertainty, the yellow region shows the 2σ environment. The black dots represent the post-fit values of the NPs, the black lines their post-fit uncertainties.

the corresponding post-fit value and σ_{θ_0} and $\hat{\sigma}_\theta$ are the pre- and post-fit uncertainties. For the γ NPs (which reflect MC statistical uncertainties), only the post-fit impacts are evaluated because there is no proper estimation of their pre-fit uncertainties. In the Asimov fit there is no difference between the pre- and the post-fit value of a NP (apart from negligible differences due to numerical precision). This will be different in the fit to data. The pre-fit impacts are finally calculated as the two differences between the actual fitted value $\hat{\mu}$ and the values obtained in the fits where θ is fixed to $\hat{\theta} \pm \sigma_{\theta_0}$. Similarly, the post-fit impacts are calculated as the respective differences to the values of μ obtained in the fits where θ is fixed to $\hat{\theta} \pm \hat{\sigma}_\theta$. From the NP ranking it can be inferred that the uncertainty on μ is dominated by the $t\bar{t}$ parton shower uncertainties affecting

the overall and relative normalisations. Here, the acceptance uncertainty has a slightly larger impact than the migration component. The third-ranked NP is related to the luminosity uncertainty which is expected because it is directly anti-correlated with the signal strength. This can be seen in the NP correlation matrix in Appendix D. Further significant impacts arise from other $t\bar{t}$ modelling uncertainties related to the top-quark p_{T} and the `Var3c` parameter. The uncertainty on the JVT efficiency also has a non-negligible impact on the measurement which can be expected considering the relatively large amount of jets present in the signal regions. Another highly ranked impact originates from the uncertainty on the misidentification of light-flavour jets as b-jets. The sensitivity can be explained by the relatively large $W+$jets background contribution in SR1 and the presence of gluon-induced jets in SR3. All in all, it can be concluded that the uncertainty on the signal strength is dominated by $t\bar{t}$ modelling uncertainties.

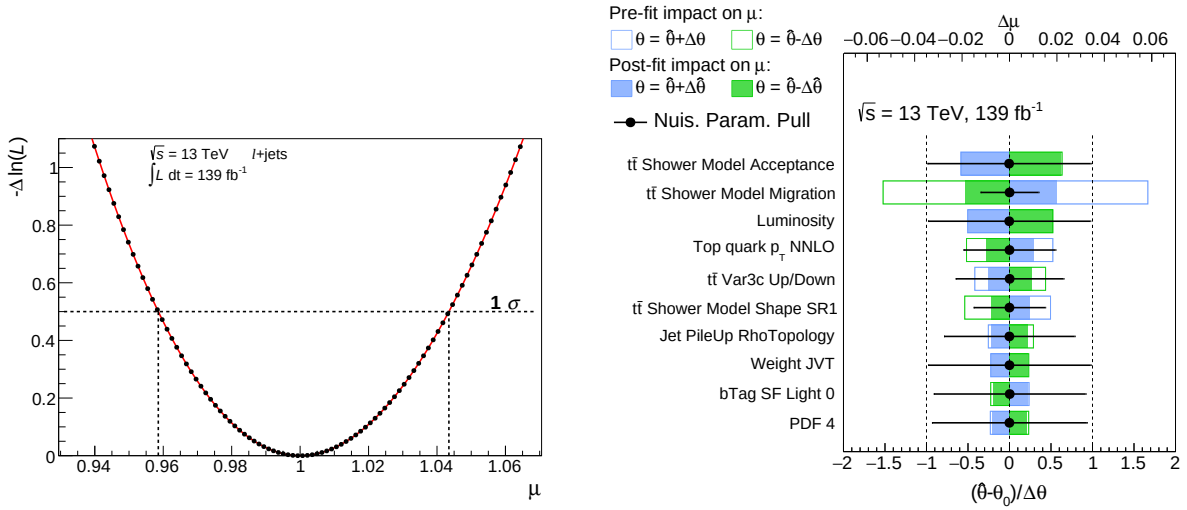

(a) Likelihood scan *(b)* Ranking

Figure 7.3.: The likelihood scan of the signal strength μ and the ranking plot showing the impact of each NP on μ in the Asimov fit. There, the empty/full boxes show the pre-/post-fit impacts while the black dots/lines represent the post-fit values/uncertainties of all NPs. Only the 10 NPs with the highest post-fit impacts are displayed.

7.2. Fit to Data

The fit configuration, that was tested on pseudo data in the previous section, is used to fit the observed full Run II data in order to extract the signal strength and thereby the cross section. Pre-fit plots showing the comparison between the prediction and the data

in each of the three signal regions are shown in Figure 7.1. The pulls of all NPs, obtained when fitting these three distributions simultaneously to the data, are shown in Figure 7.4.

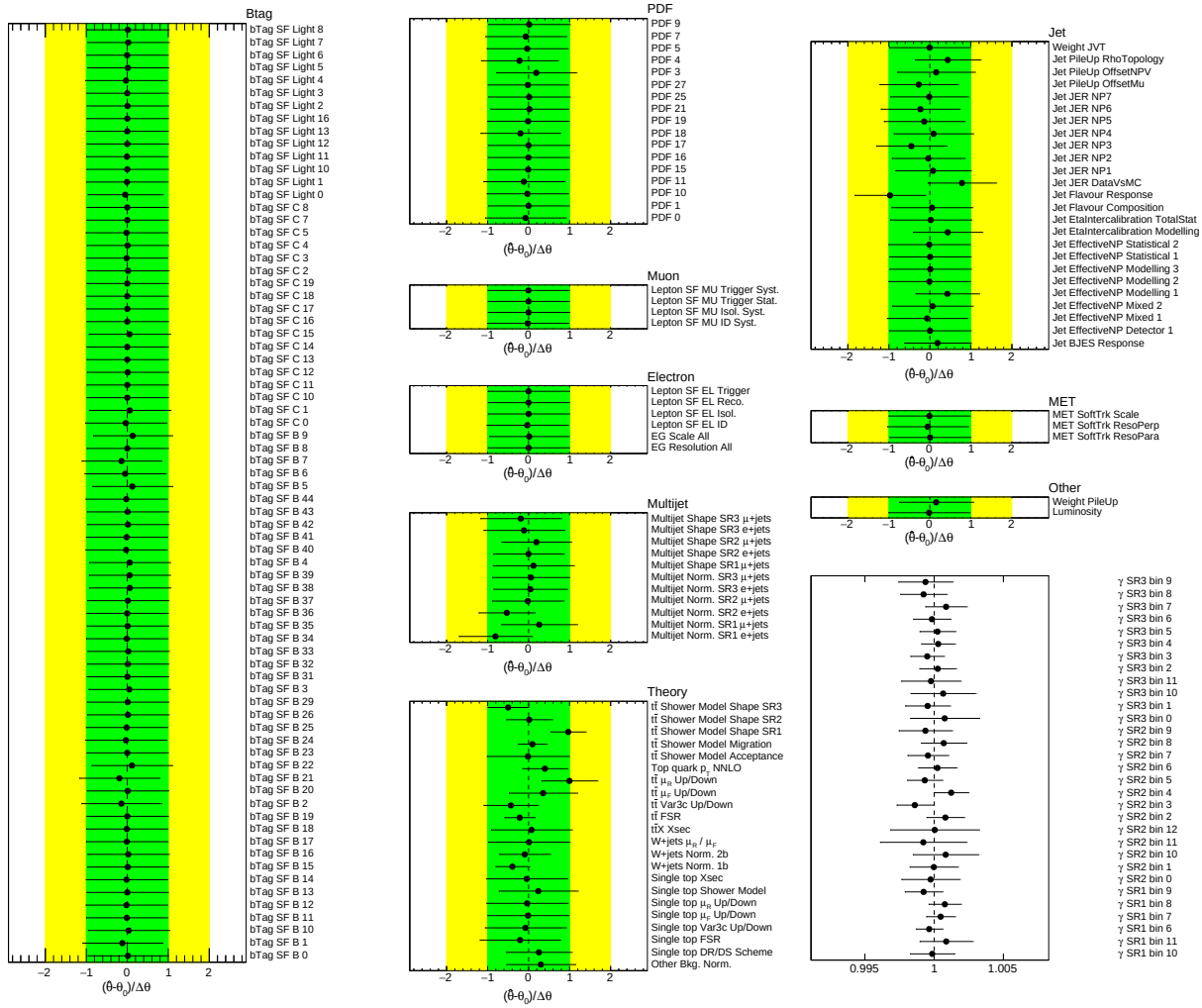

Figure 7.4.: Pulls and constraints of all nuisance parameters when fitting the observed data. The green band represents the 1σ region, corresponding to the prior uncertainty, the yellow region shows the 2σ environment. The black dots represent the post-fit values of the NPs, the black lines their post-fit uncertainties.

All in all, only few pulls are observed which are not very large and are still within the respective 1σ bands. The constraints on the uncertainties are very similar to the ones in the Asimov fit (Figure 7.2). The NPs with the largest pulls are related to the parton shower and hadronisation uncertainty on the shape in SR1, the renormalisation scale uncertainty in the $t\bar{t}$ simulation, the jet flavour response, and the fake-electron background normalisation uncertainty in SR1. No significant pull of the NP representing the top-quark p_{T} reweighting is observed which is expected because the used variables are

not sensitive to the p_{T} mismodelling (see Appendix B). It is important to make sure that these pulls are indeed able to compensate for differences between the prediction and the data. Therefore, histograms illustrating the effects of these four uncertainties on the total prediction (signal+background) are investigated (see Figure 7.5). The effect of the $t\bar{t}$ parton shower uncertainty on the shape, together with the data/prediction discrepancy, is shown in Figure 7.5a. The data seems to follow the shape of the 1σ variation in SR1 which explains the observed pull in this region. Figure 7.5b presents the effects of the variation of μ_{R} in $t\bar{t}$ events. These histograms help to understand the observed pull because the data clearly prefers the shape of the 1σ variation in SR3. Thus, this pull can compensate the shape discrepancy in this region while the normalisation discrepancy is compensated by the pull of the NP representing the jet flavour response uncertainty (see Figure 7.5c). However, this pull also significantly changes the normalisation in SR1, but the effect is then again counterbalanced by the pull of the multijet background normalisation NP for e+jets events in SR1 (see Figure 7.5d). In summary, it can be stated that the obtained pulls are consistent with the observed discrepancies with data before the fit.

The post-fit event yields are given in Table 7.1 and the post-fit distributions of the used variables are shown in Figure 7.6. Comparing them to the pre-fit distributions in Figure 7.1, one can observe that the agreement with data is significantly improved. Also, the total uncertainty is heavily reduced after the fit. The reason is that, different from the pre-fit uncertainties, the constraints and especially the correlations (see Appendix D) of all NPs, obtained from the fit to data, are exploited in the post-fit uncertainties. All in all, the model used in the fit is able to describe the data within the uncertainties.

The results can be further validated by investigating post-fit distributions of variables which were not used in the fit. They are obtained by propagating all the constraints and pulls of the NPs, as well as the fitted signal strength μ, to the respective distributions. Pre- and post-fit distributions of the leading jet and the lepton p_{T} are shown in Figures 7.7 and 7.8. Although they were not considered in the fit, the pulls of the NPs and the fitted signal strength improve their agreement with data partially, especially in SR1. The agreement in SR2 and SR3 is almost unchanged. However, this is not surprising considering the much larger statistical power of SR1 compared to the other regions. Besides that, the used variables are not sensitive to p_{T} mismodelling and thus the pulls of the NPs are actually not expected to account for these effects. To investigate the impact on the cross section, a pseudo dataset was created in which the fourth jet p_{T} distribution in SR2 (which also shows a non-negligible post-fit discrepancy) is reweighted to the distribution in data [104]. However, no significant impact on the $t\bar{t}$ cross section was observed when fitting this pseudo dataset. All in all, this validates that the fit results are reasonable.

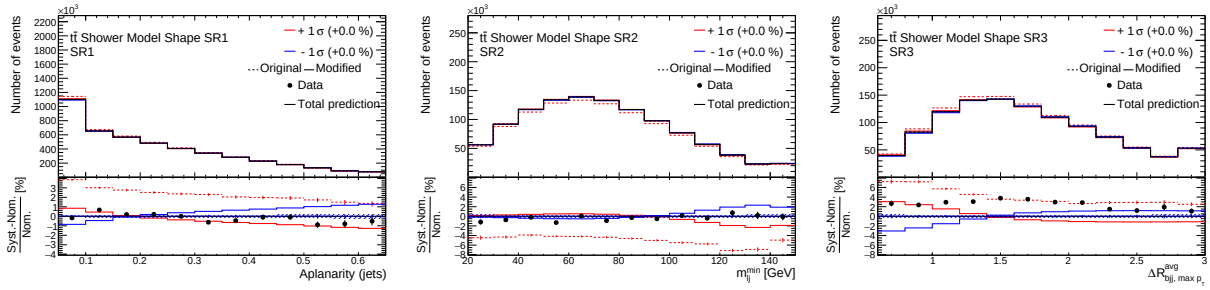

(a) $t\bar{t}$ parton shower & hadronisation shape uncertainty

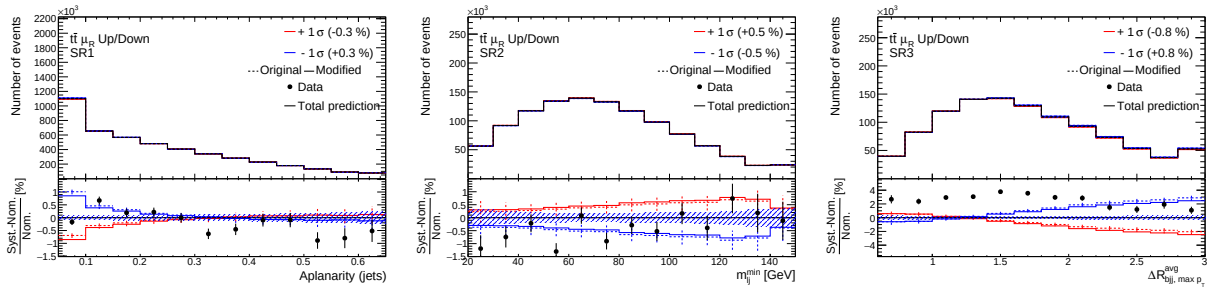

(b) $t\bar{t}$ μ_{R} variation

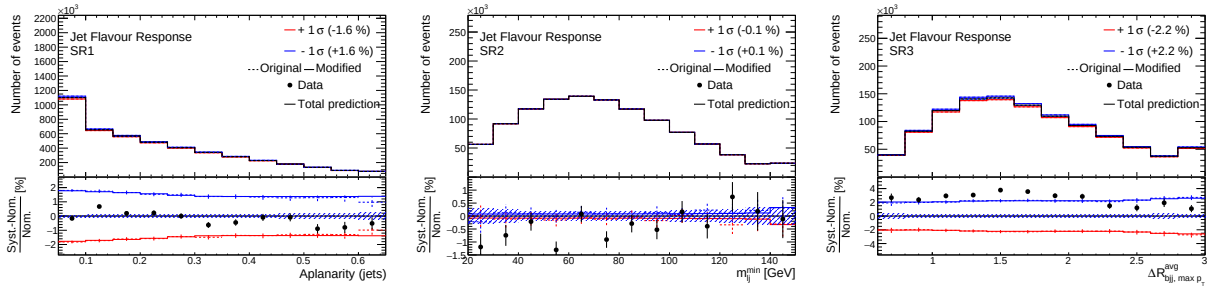

(c) Jet flavour response uncertainty

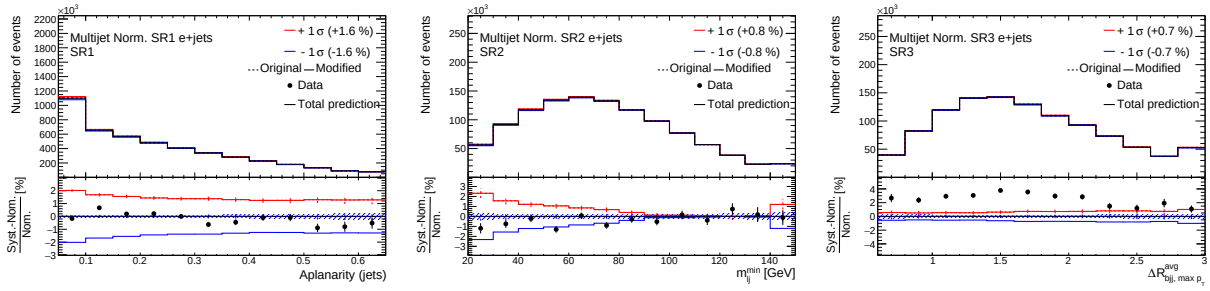

(d) Multijet background (e+jets) normalisation uncertainty

Figure 7.5.: The effects of the most pulled nuisance parameters on the total prediction in SR1, SR2, and SR3 (from left to right). Here, lines coloured in red/blue present the $\pm 1\sigma$ effect. The dotted/solid lines show the effect before/after smoothing, symmetrisation, and the removal of the normalisation effect (only done for shape uncertainties). The hashed bands represent the MC statistical uncertainties while the black dots show the discrepancy between the data and the (nominal) total prediction.

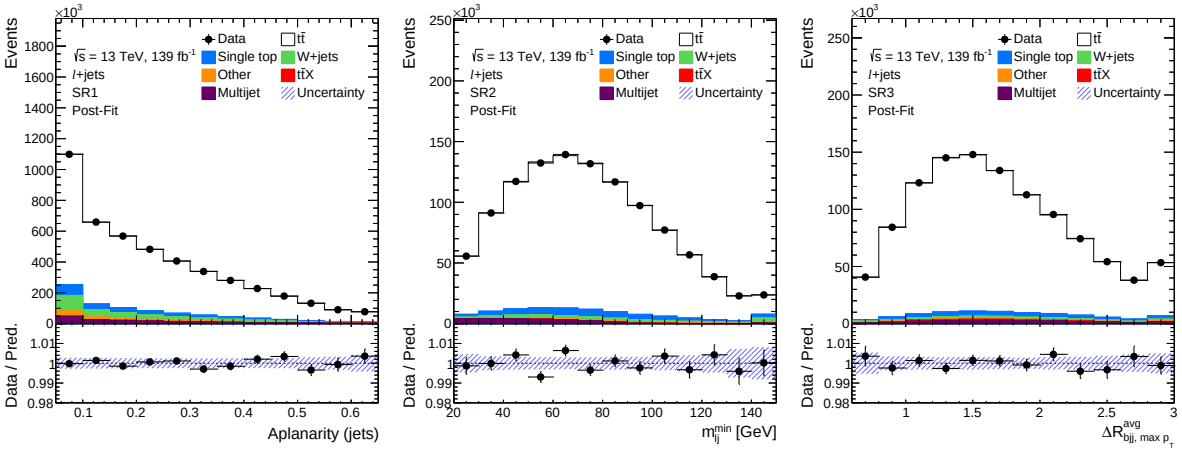

(a) SR1 *(b)* SR2 *(c)* SR3

Figure 7.6.: Post-fit distributions of the chosen variables for the fit in all three signal regions. Electron and muon channels are combined. The total uncertainty (stat. + syst.) is shown. The first and last bin contain underflow and overflow events, respectively. The $t\bar{t}$ contribution is scaled to the measured cross section.

	SR1	**SR2**	**SR3**
$t\bar{t}$	3690000 ± 60000	991000 ± 7000	1011000 ± 9000
$W+$jets	300000 ± 70000	24000 ± 6000	18000 ± 6000
Single top	263000 ± 25000	51000 ± 6000	37000 ± 6000
Multijet	160000 ± 60000	23000 ± 5000	23000 ± 7000
$t\bar{t}X$	16000 ± 2100	2080 ± 280	7500 ± 1000
Other	100000 ± 40000	9000 ± 4000	7300 ± 2800
Total	4541000 ± 11000	1100600 ± 2500	1103300 ± 2600
Data	4540856	1100552	1103250

Table 7.1.: Post-fit event yields for all signal/background sources in each signal region. The component $t\bar{t}X$ summarises contributions from $t\bar{t}H$, $t\bar{t}W$, and $t\bar{t}Z$, while contributions from diboson and $Z+$jets production are summarised as the other (remaining) background. The shown uncertainties include both statistical and systematic uncertainties. Very good agreement between the data and the total prediction is achieved.

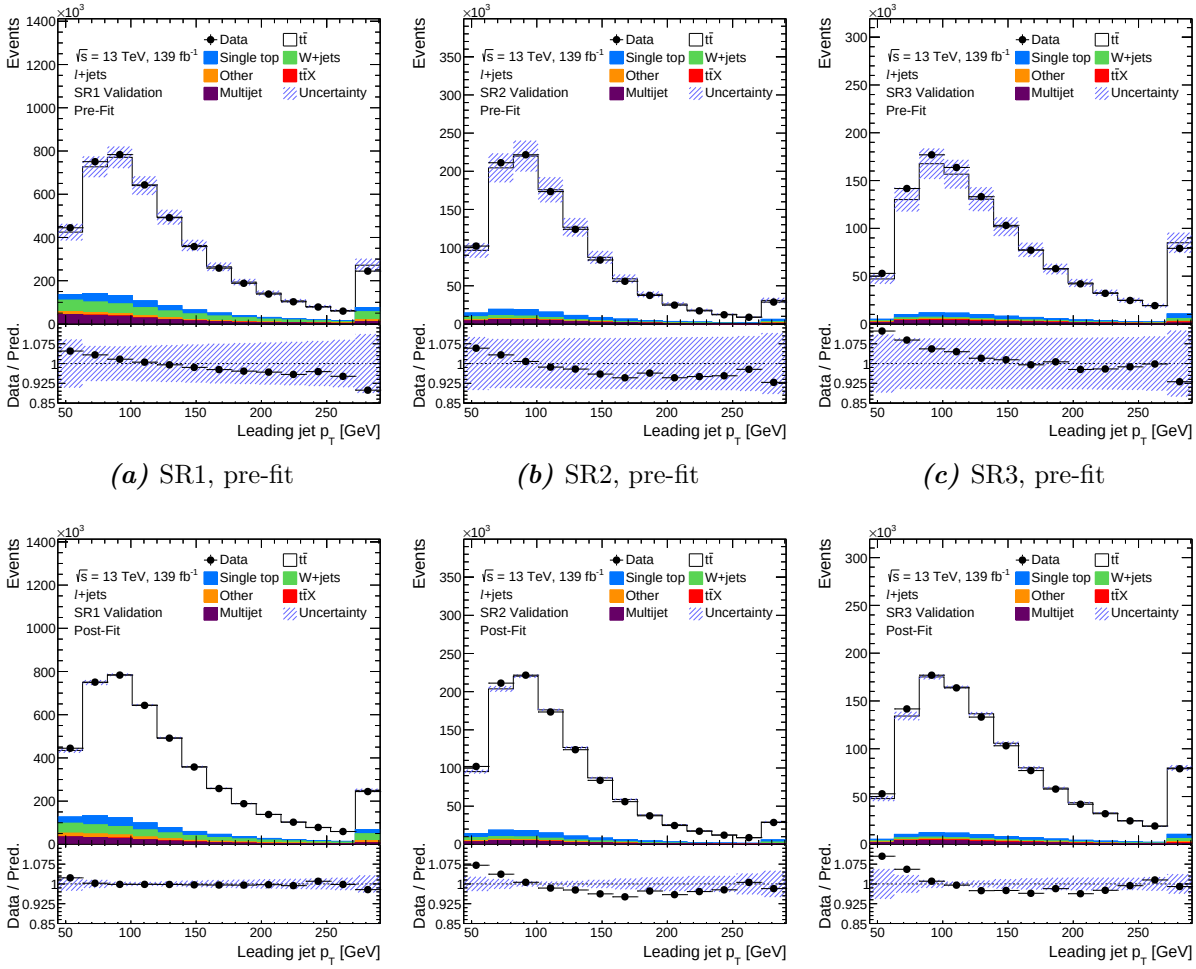

(a) SR1, pre-fit ***(b)*** SR2, pre-fit ***(c)*** SR3, pre-fit

(d) SR1, post-fit ***(e)*** SR2, post-fit ***(f)*** SR3, post-fit

Figure 7.7.: Pre- and post-fit distributions of the leading jet p_{T} in all three signal regions. Electron and muon channels are combined. The total uncertainty (stat. + syst.) is shown. The first and last bin contain underflow and overflow events, respectively. The $t\bar{t}$ contribution is scaled to the measured cross section.

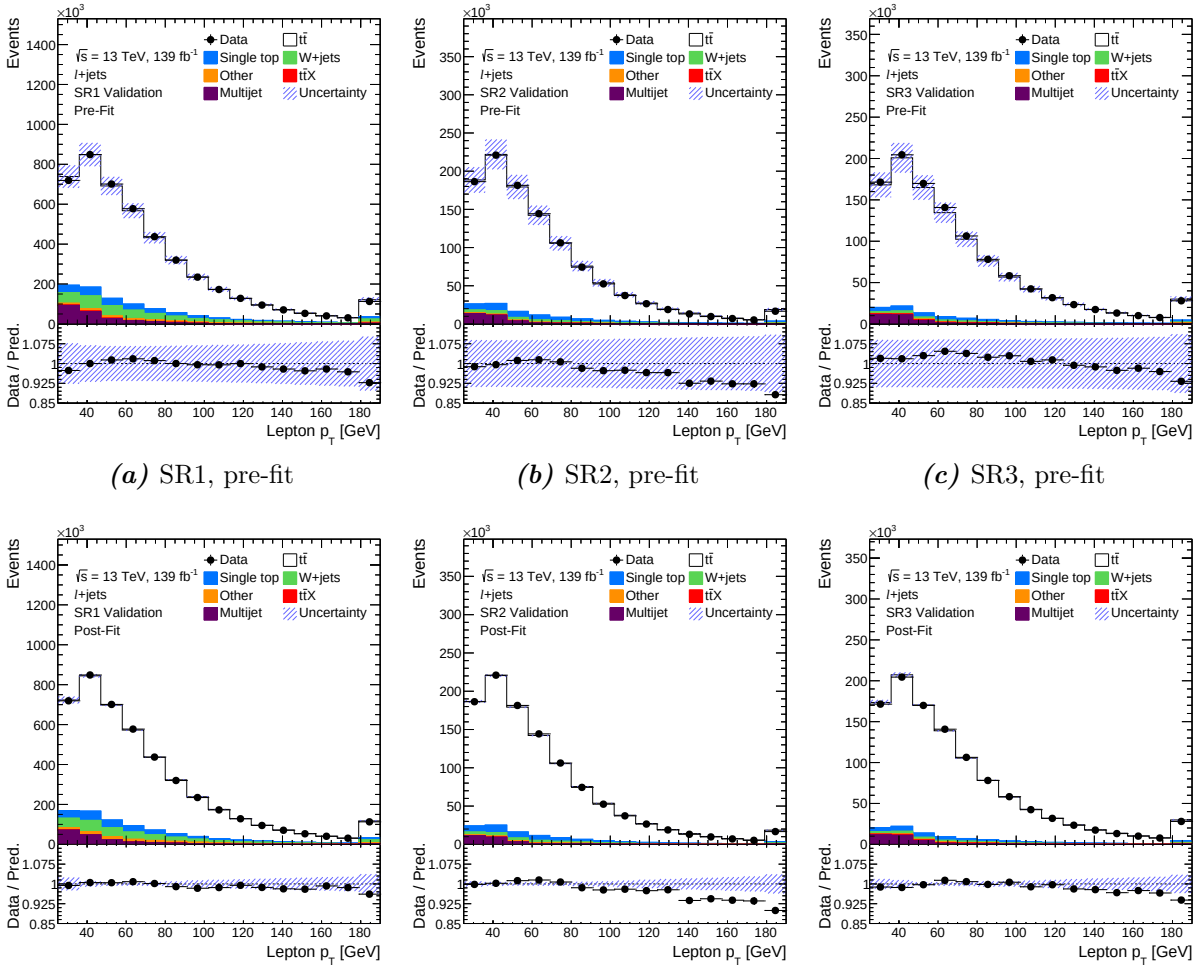

(a) SR1, pre-fit *(b)* SR2, pre-fit *(c)* SR3, pre-fit

(d) SR1, post-fit *(e)* SR2, post-fit *(f)* SR3, post-fit

Figure 7.8.: Pre- and post-fit distributions of the lepton p_{T} in all three signal regions. Electron and muon channels are combined. The total uncertainty (stat. + syst.) is shown. The first and last bin contain underflow and overflow events, respectively. The $t\bar{t}$ contribution is scaled to the measured cross section.

Finally, the measured signal strength in the observed data is

$$\mu = 0.9975^{+0.0424}_{-0.0415}\,. \tag{7.1}$$

Here, the total uncertainty is quoted which is directly obtained from the profile likelihood fit. Multiplying the signal strength with the SM prediction $\sigma_{t\bar{t}}^{\mathrm{SM}} = 831.76$ pb, the measured $t\bar{t}$ cross section is determined to be

$$\sigma_{t\bar{t}} = 829.7^{+35.3}_{-34.5}\ \mathrm{pb} = 829.7 \pm 0.4\ (\mathrm{stat.})\ ^{+35.3}_{-34.5}\ (\mathrm{syst.})\ \mathrm{pb} \tag{7.2}$$

with a total uncertainty of 4.3%. The quoted statistical uncertainty is obtained by repeating the fit while all NPs are set constant to their post-fit values. The pure systematic uncertainty is then estimated by subtracting the statistical uncertainty in quadrature from the total uncertainty. It can be concluded that the measurement is completely dominated by systematic uncertainties. The likelihood scan of the cross section ($\mu \times \sigma_{t\bar{t}}^{\mathrm{SM}}$) is shown in Figure 7.9a. As in the Asimov fit, the log-likelihood curve is parabolic and smooth which validates that the fit is stable and the results and uncertainties are reliable. The ranking of nuisance parameters (Figure 7.9b) is very similar compared to the ranking in the Asimov fit (Figure 7.3b). The relative order slightly differs which is not surprising because the post-fit values are different which in principle can change the impacts.

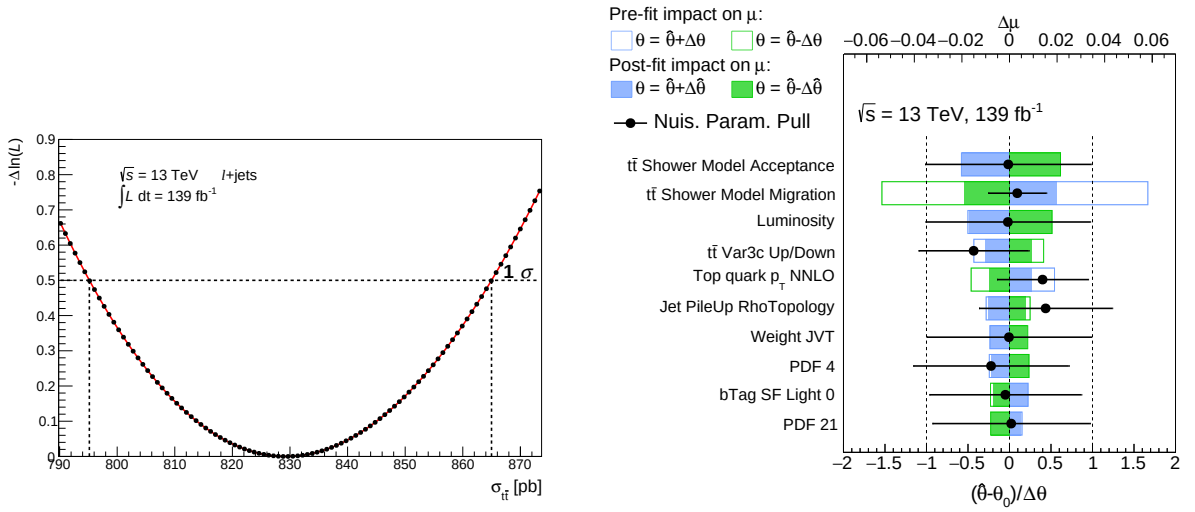

(a) Likelihood scan *(b)* Ranking

Figure 7.9.: The likelihood scan of the cross section and the ranking plot showing the impact of each NP on the signal strength μ in the fit to data. There, the empty/full boxes show the pre-/post-fit impacts while the black dots/lines represent the post-fit values/uncertainties of all NPs. Only the 10 NPs with the highest post-fit impacts are displayed.

The breakdown of systematic uncertainties on the measured cross section is given in Table 7.2. As already indicated by the nuisance parameter ranking, the uncertainty is dominated by $t\bar{t}$ modelling (especially parton shower modelling) and the luminosity uncertainty. Other significant uncertainties are related to the jet reconstruction, the MC background modelling, and the flavour tagging.

Category	$\frac{\Delta\sigma_{t\bar{t}}}{\sigma_{t\bar{t}}}$ [%]	
Signal modelling		
$t\bar{t}$ shower/hadronisation	+3.1	−2.8
$t\bar{t}$ scale and PDF variations	+2.0	−1.8
Background modelling		
MC background modelling	+1.5	−1.4
Multijet background	+0.8	−0.8
Detector modelling		
Jet reconstruction	+1.9	−1.9
Luminosity	+1.9	−1.7
Flavour tagging	+1.2	−1.4
$E_{\mathrm{T}}^{\mathrm{miss}}$ + pile-up	+0.5	−0.4
Muon reconstruction	+0.5	−0.3
Electron reconstruction	+0.2	−0.4
Simulation stat. uncertainty	+0.8	−0.6
Total systematic uncertainty	+4.3	−4.2
Data stat. uncertainty	+0.05	−0.05
Total uncertainty	+4.3	−4.2

Table 7.2.: The contributions of systematic uncertainties, grouped into categories, to the uncertainty on the measured cross section. The impact of each category is evaluated by performing the fit while all NPs in the respective category are fixed to their post-fit values. The uncertainty in this fit is then subtracted in quadrature from the total uncertainty in order to estimate the contribution.

7.3. Consistency Checks

To make sure that the obtained result for the signal strength (or the cross section) is stable, several consistency tests are performed. For these tests, the fit is repeated using only data recorded in the 2015+2016 (together with `mc16a` MC), the 2017 (with `mc16d` MC), or the 2018 period (with `mc16e` MC). The proper luminosity uncertainties (Section 6.1.1) in the different periods are taken into account. In addition, the fit is repeated using either data (and simulated data) related to the e+jets or the μ+jets channel. All the performed fits are independent of each other. The results are summarised in Figure 7.10. The first row

refers to the nominal fit (Section 7.2), i.e. full Run II data is used and events from both lepton channels are combined inside the same histograms, which results in the smallest uncertainty among all presented fits. The central value is almost independent of the data period, whereas there is a small difference between both lepton channels. However, this is consistent with the observed deficit of events in the e+jets channel and the observed excess of events in the μ+jets channel in SR1 and SR2 (see Tables 5.2 and 5.3). In summary, it can be said that all results are in very good agreement with each other demonstrating the stability of the main result presented in Section 7.2.

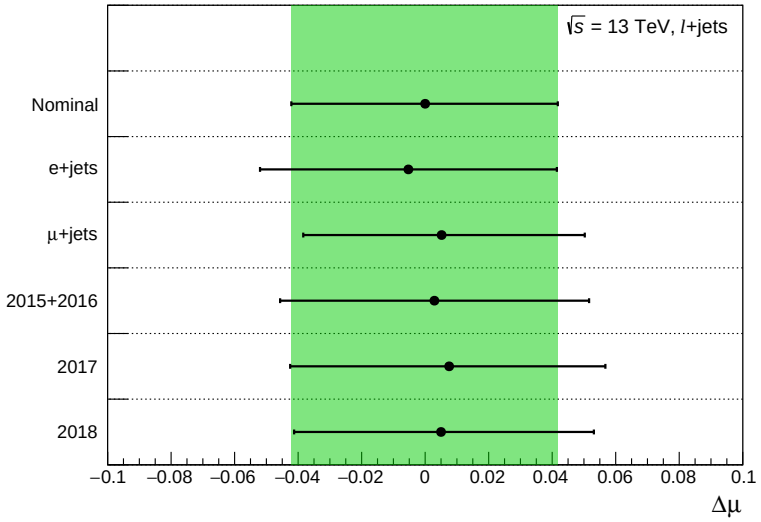

Figure 7.10.: Summary of the performed consistency tests for the measured signal strength μ. Individual data periods and lepton channels are fitted separately. The difference $\Delta\mu = \mu - \mu_{\text{nominal}}$ between the results is shown, where the nominal result is referring to the Run II fit where both lepton channels are combined. The black lines show the total uncertainty in each fit, while the green band represents the uncertainty in the nominal fit.

7.4. Comparisons

A comparison between several LHC $t\bar{t}$ cross section measurements (including the result from Section 7.2) and the NNLO+NNLL theory prediction (see Section 2.5.4) is presented in Figure 7.11. The parametrisation proposed in Ref. [124] was used to determine the predicted cross section for different values of $\sqrt{s}$. PDF+α_s and QCD scale uncertainties were evaluated as described in Section 2.5.4. One can see that all measurements agree very well with the predicted SM values. Especially, the presented result $\sigma_{t\bar{t}} = 829.7^{+35.3}_{-34.5}$ pb, obtained by analysing 139 fb^{-1} of ATLAS data, is in good agreement with the predicted value

of 831.76 pb. The relative difference is only 0.2%. The achieved precision of 4.3% is comparable to the CMS dilepton result $\sigma_{t\bar{t}} = 803 \pm 2$ (stat.) ± 25 (syst.) ± 20 (lumi.) pb [125], measured in 35.9 fb^{-1} of data, which provides a precision of 4.0%. Still, the preliminary ATLAS $e\mu$ result $\sigma_{t\bar{t}} = 826.4 \pm 3.6$ (stat.) ± 11.8 (syst.) ± 15.7 (lumi.) pb [126] achieves an even higher precision of 2.4% by analysing 36.1 fb^{-1} of data. However, comparing to the last ATLAS ℓ+jets measurement $\sigma_{t\bar{t}} = 817 \pm 13$ (stat.) ± 103 (syst.) ± 88 (lumi.) pb [45], the result presented in this thesis currently provides the highest precision for this channel within the ATLAS collaboration.

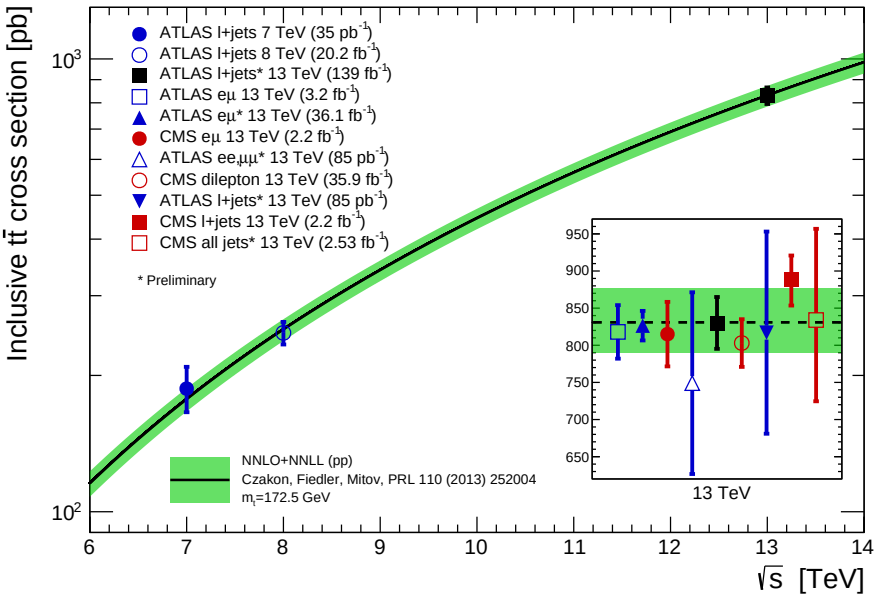

Figure 7.11.: Summary of a selection of ATLAS and CMS $pp \to t\bar{t}$ cross section measurements at different centre-of-mass energies, including the result presented in this thesis (coloured in black). The other results are taken from Refs. [39, 44–47, 125–128]. Measurements are compared to theory predictions calculated at NNLO in QCD including resummation of NNLL soft gluon terms with `Top++` (v2.0). Theory uncertainties, illustrated as the green band, include QCD scale as well as PDF+α_s uncertainties. Measurements and predictions assume $m_t = 172.5$ GeV.

7.5. Mass Dependence

The cross section measurement in this thesis assumes a top-quark mass of $m_t = 172.5$ GeV. Alternative $t\bar{t}$ samples with varied top-quark masses ($m_t = 171, 172, 173, 174$ GeV) are used in the fit to quantify the impact of the mass dependence on the measured cross

section. The reasons for the dependence are acceptance effects but also potential effects on the shape of the used distributions leading to different pulls of nuisance parameters which might affect the measured value. The events in the different mass samples are normalised to their proper cross sections $\sigma_{t\bar{t}}^{\mathrm{SM}}(m_t)$ which are summarised in Table 7.3. Due to this dependence, the measured cross section can in principle be used to extract the top-quark mass.

$\boldsymbol{m_t}$ **[GeV]**	171	172	172.5	173	174
$\boldsymbol{\sigma_{t\bar{t}}^{\mathrm{SM}}}$ **[pb]**	866.81	843.25	831.76	820.44	798.34

Table 7.3.: The predicted NNLO+NNLL $t\bar{t}$ cross section at $\sqrt{s} = 13$ TeV as a function of the assumed top-quark mass. The values are determined as described in Section 2.5.4 and by using the mass parametrisation proposed in Ref. [53].

Since the alternative samples are only produced with fast detector simulation, one cannot simply replace the distributions for the fit. Instead, the alternative mass distributions are compared to the corresponding fast simulation distributions for $m_t = 172.5$ GeV. The respective relative differences are then propagated to the nominal full simulation sample (as it is done for $t\bar{t}$ modelling uncertainties). The obtained distributions are further smoothed in order to account for statistical fluctuations but no symmetrisation is applied. Technically, all of this is done by adding two additional nuisance parameters to the fit configuration. One nuisance parameter represents the variation $\Delta m_t = \pm 0.5$ GeV, the other one $\Delta m_t = \pm 1.5$ GeV. The effects of the mass variations in each signal region are shown in Figure 7.12. When the actual fit is performed, the NPs are fixed to either 0 or ± 1. This allows an easy switching of the assumed top-quark mass in the $t\bar{t}$ prediction without introducing a bias from fast detector simulation. However, this procedure assumes that $t\bar{t}$ modelling uncertainties, evaluated for $m_t = 172.5$ GeV, are independent of the top-quark mass, which is not necessarily correct. Since samples for alternative $t\bar{t}$ generators are only available with the default mass setting, this approximation cannot be avoided. The results of the fits to the observed data when assuming different top-quark masses in the fit configuration are shown in Figure 7.13 together with a linear fit to the obtained values. As one can see, the mass dependence of the extracted cross section only approximately follows a linear dependence. The slope corresponds to 11 pb/GeV which is in the order of 1.3% (with respect to the central value of 829.7 pb). Unfortunately, this (relatively) large dependence makes it impossible to use this measurement for a precise top-quark mass extraction.

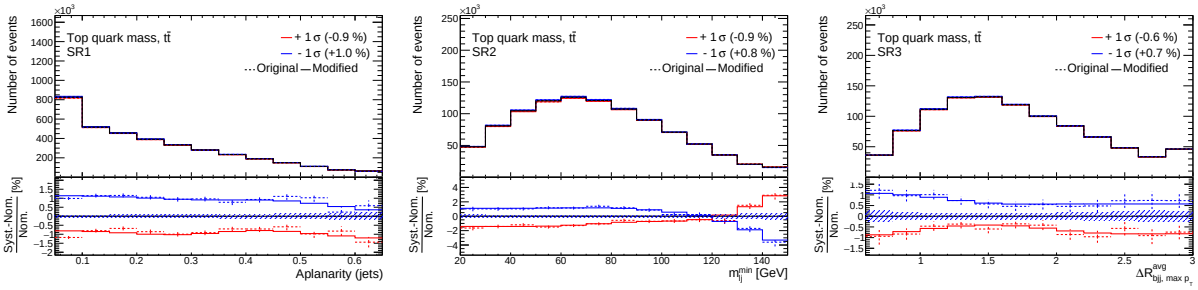

(a) SR1, $\Delta m_t = 0.5$ GeV

(b) SR2, $\Delta m_t = 0.5$ GeV

(c) SR3, $\Delta m_t = 0.5$ GeV

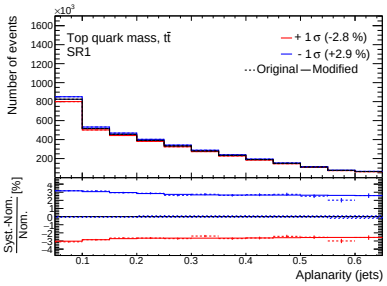

(d) SR1, $\Delta m_t = 1.5$ GeV

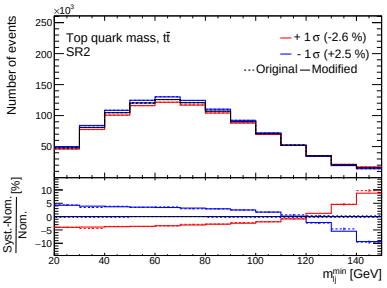

(e) SR2, $\Delta m_t = 1.5$ GeV

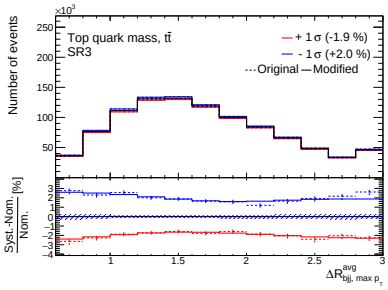

(f) SR3, $\Delta m_t = 1.5$ GeV

Figure 7.12.: The effects of the top-quark mass variations on the $t\bar{t}$ prediction in each signal region. The dotted/solid lines show the effects before/after smoothing. The hashed bands represent the MC statistical uncertainties. The $\pm 1\sigma$ distributions show the effects of the up/down variation of the assumed top-quark mass (top: ± 0.5 GeV, bottom: ± 1.5 GeV). The nominal setting is $m_t = 172.5$ GeV.

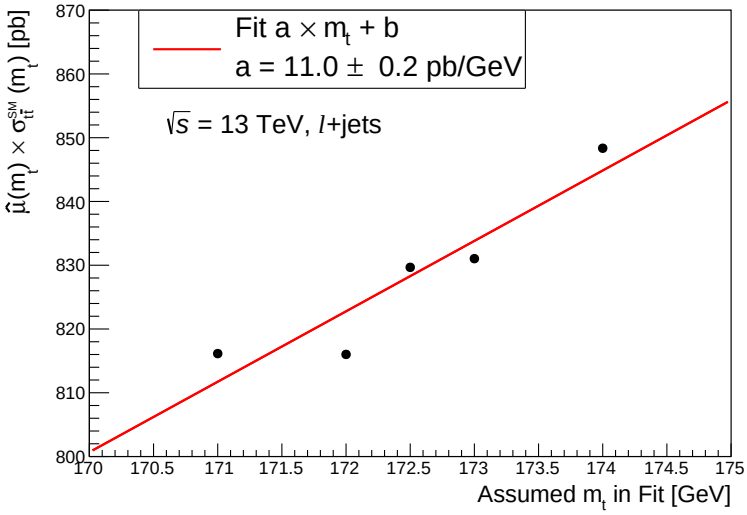

Figure 7.13.: Extracted $t\bar{t}$ cross sections from the fit to observed data when assuming different top-quark masses in the fit configuration. The shown uncertainties include only statistical uncertainties. A linear fit to the central values is also shown.

7.6. Fiducial Cross Section

For the inclusive cross section measurement, the signal strength but also the constraints on $t\bar{t}$ modelling uncertainties, measured in a small experimentally accessible phase space, are extrapolated to the full phase space. However, it is not always clear whether this is a valid approach. Potential problems of the extrapolation can be avoided by measuring the cross section in a fiducial region. This region is defined using particle-level objects which can be understood as the collection of generated stable particles (mean lifetime greater than 0.3×10^{-10} s) without the simulation of the detector response. This means that only the MC generator event information on truth-level is utilised. Leptons are defined as electrons, muons, and neutrinos originating from W or Z boson decays, including subsequent decays of tau leptons. Electrons and muons are combined with photons within $\Delta R < 0.1$ and are finally required to have $p_{\mathrm{T}} > 25$ GeV and $|\eta| < 2.5$. Particle-level jets are reconstructed with the anti-k_t algorithm with a radius parameter of $R = 0.4$ and are required to have $p_{\mathrm{T}} > 25$ GeV and $|\eta| < 2.5$. All stable particles (except for the electrons, muons, photons, and neutrinos used in the lepton definition) are used for jet clustering. Furthermore, jets can be identified as b-jets via ghost matching [129]. Finally, the fiducial region is defined to be very similar to the three signal regions used in the analysis. Events are required to have at least four jets, exactly one electron or muon, and either one or two ghost-hadron b-tags. Whenever there is an overlap between a jet and a charged lepton (i.e. $\Delta R(\mathrm{jet}, e/\mu) < 0.4$), the whole event is discarded.

To measure the fiducial cross section, the fit configuration has to be slightly adapted. In a simple counting experiment, the inclusive cross section is determined as

$$\sigma_{\mathrm{inc}} = \frac{N_{\mathrm{data}} - N_{\mathrm{bkg}}}{L_{\mathrm{int}} \times A_{\mathrm{fid}} \times C}\,, \tag{7.3}$$

where $A_{\mathrm{fid}} = \frac{N_{\mathrm{fid}}}{N_{\mathrm{tot}}}$ is the fiducial acceptance with N_{fid} being the number of events in the fiducial region and N_{tot} the total number of generated events. The correction factor is defined as $C = \frac{N_{\mathrm{reco}}}{N_{\mathrm{fid}}}$, where N_{reco} is the number of reconstructed $t\bar{t}$ events in all signal regions. L_{int} is the integrated luminosity of the analysed dataset. Absorbing the fiducial acceptance into the inclusive cross section in Equation 7.3, one obtains an expression for the fiducial cross section:

$$\sigma_{\mathrm{fid}} = A_{\mathrm{fid}} \times \sigma_{\mathrm{inc}} = \frac{N_{\mathrm{data}} - N_{\mathrm{bkg}}}{L_{\mathrm{int}} \times C}\,. \tag{7.4}$$

Since the right side in Equation 7.4 no longer depends on the fiducial acceptance, only $t\bar{t}$ modelling uncertainties on the correction factor C will be relevant in the measurement.

Thus, modelling uncertainties are expected to have a smaller impact compared to the inclusive cross section measurement, leading to a more precise result. The acceptance on particle-level is determined to be $A = 24.7\%$ (see Table 7.4). This value is calculated in $t\bar{t}$ samples with at least one leptonic W boson decay. Therefore, the branching ratio $BR = 54.6\%$ [18] of the considered decay channels has to be taken into account, i.e. $A_{\text{fid}} = A \times BR$. Since the value $\sigma_{\text{inc}}^{\text{ref}} = 831.76$ pb is used as a reference value for the inclusive cross section (i.e. all $t\bar{t}$ distributions are normalised to this value before the fit), the reference value for the fiducial cross section is $\sigma_{\text{fid}}^{\text{ref}} = A \times BR \times \sigma_{\text{inc}}^{\text{ref}} = 112.2$ pb.

In the inclusive cross section measurement, all alternative $t\bar{t}$ distributions, used to estimate the modelling uncertainties, are scaled to the same inclusive cross section. To measure the fiducial cross section, the $t\bar{t}$ modelling uncertainties have to be rescaled such that the normalisation effects correspond to the respective uncertainties on the correction factors. Uncertainties related to the detector or to the background modelling remain unaltered. Because of the usage of multiple signal regions, correction factors are defined for each region i as $C^i = \frac{N^i_{\text{reco}}}{N_{\text{fid}}}$. For the fiducial cross section measurement, each alternative $t\bar{t}$ distribution is scaled to the fiducial acceptance of the sample it is compared to (comparisons similar as described in Section 6.2). This rescaling ensures that the normalisation uncertainties originating from $t\bar{t}$ modelling correspond to the uncertainties on C^i:

$$\frac{\frac{N_{\text{fid, nom}}}{N_{\text{fid, alt}}} \times N^i_{\text{reco, alt}} - N^i_{\text{reco, nom}}}{N^i_{\text{reco, nom}}} = \frac{\frac{N^i_{\text{reco, alt}}}{N_{\text{fid, alt}}} - \frac{N^i_{\text{reco, nom}}}{N_{\text{fid, nom}}}}{\frac{N^i_{\text{reco, nom}}}{N_{\text{fid, nom}}}} = \frac{C^i_{\text{alt}} - C^i_{\text{nom}}}{C^i_{\text{nom}}} \,. \tag{7.5}$$

Here, $N_{\text{fid/reco, nom/alt}}$ is the number of fiducial/reconstructed events in the nominal/alternative $t\bar{t}$ sample. As in the inclusive measurement (see Section 6.2.1), all alternative $t\bar{t}$ samples are reweighted to the same NNLO QCD + NLO EW top-quark p_{T} distribution (on MC truth-level) in order to avoid double counting of uncertainties related to the top-quark p_{T}. Therefore, their distributions are scaled to the fiducial acceptance evaluated in the nominal Powheg-Box + Pythia 8 $t\bar{t}$ sample which is reweighted to the same p_{T} distribution. For the PDF uncertainties, all considered `PDF4LHC15` variations (also reweighted to the NNLO top-quark p_{T}) are scaled to the fiducial acceptance evaluated for the central `PDF4LHC15` prediction (also reweighted). In contrast to this, the distributions from the reweighted Powheg-Box + Pythia 8 sample are scaled to the fiducial acceptance evaluated in the non-reweighted sample. This procedure, which was similarly used in the inclusive measurement, ensures that all uncertainties are properly estimated and double counting is avoided. The comparisons are summarised in Table 7.4 including the particle-level acceptances and the scale factors that are applied on alternative $t\bar{t}$ distributions.

Sample	$\boldsymbol{A}$ [%]	$\frac{\boldsymbol{A}_{\text{alt}}-\boldsymbol{A}_{\text{nom}}}{\boldsymbol{A}_{\text{nom}}}$ [%]	$\frac{\boldsymbol{A}_{\text{nom}}}{\boldsymbol{A}_{\text{alt}}}$	C^1	C^2	C^3
Powheg-Box + Pythia 8	24.73	—	—	0.232	0.064	0.063
Powheg-Box + Pythia 8 (NNLO Rew.)	24.55	-0.75	1.008	0.231	0.064	0.063
Powheg-Box + Pythia 8 (NNLO Rew.)	24.55	—	—	0.231	0.064	0.063
PP8 $\mu_{\text{R}}^{\text{FSR}} \times 2$ (NNLO Rew.)	24.86	1.29	0.987	0.230	0.066	0.064
PP8 $\mu_{\text{R}}^{\text{FSR}} \times 0.5$ (NNLO Rew.)	23.84	-2.86	1.029	0.232	0.062	0.060
PP8 $\mu_{\text{R}} \times 2$ (NNLO Rew.)	24.49	-0.25	1.003	0.231	0.065	0.062
PP8 $\mu_{\text{R}} \times 0.5$ (NNLO Rew.)	24.64	0.38	0.996	0.231	0.064	0.063
PP8 $\mu_{\text{F}} \times 2$ (NNLO Rew.)	24.51	-0.15	1.001	0.231	0.065	0.062
PP8 $\mu_{\text{F}} \times 0.5$ (NNLO Rew.)	24.59	0.17	0.998	0.232	0.064	0.063
PP8 `Var3cUp` (NNLO Rew.)	24.65	0.41	0.996	0.232	0.064	0.063
PP8 `Var3cDown` (NNLO Rew.)	24.45	-0.38	1.004	0.231	0.065	0.062
Powheg-Box + Herwig 7 (NNLO Rew.)	24.62	0.31	0.997	0.239	0.061	0.065
PP8 `PDF4LHC15` Central (NNLO Rew.)	24.51	—	—	0.248	0.070	0.069
PP8 `PDF4LHC15` NP0 (NNLO Rew.)	24.53	0.10	0.999	0.248	0.070	0.069
PP8 `PDF4LHC15` NP1 (NNLO Rew.)	24.52	0.06	0.999	0.248	0.070	0.069
PP8 `PDF4LHC15` NP2 (NNLO Rew.)	24.52	0.03	1.000	0.248	0.070	0.069
PP8 `PDF4LHC15` NP3 (NNLO Rew.)	24.49	-0.08	1.001	0.248	0.070	0.069
PP8 `PDF4LHC15` NP4 (NNLO Rew.)	24.55	0.19	0.998	0.247	0.070	0.069
PP8 `PDF4LHC15` NP5 (NNLO Rew.)	24.54	0.12	0.999	0.248	0.070	0.069
PP8 `PDF4LHC15` NP6 (NNLO Rew.)	24.51	-0.01	1.000	0.248	0.070	0.069
PP8 `PDF4LHC15` NP7 (NNLO Rew.)	24.53	0.11	0.999	0.248	0.070	0.069
PP8 `PDF4LHC15` NP8 (NNLO Rew.)	24.51	0.00	1.000	0.248	0.070	0.069
PP8 `PDF4LHC15` NP9 (NNLO Rew.)	24.52	0.06	0.999	0.248	0.070	0.069
PP8 `PDF4LHC15` NP10 (NNLO Rew.)	24.52	0.04	1.000	0.248	0.070	0.069
PP8 `PDF4LHC15` NP11 (NNLO Rew.)	24.52	0.06	0.999	0.248	0.070	0.069
PP8 `PDF4LHC15` NP12 (NNLO Rew.)	24.50	-0.01	1.000	0.248	0.070	0.069
PP8 `PDF4LHC15` NP13 (NNLO Rew.)	24.51	0.00	1.000	0.248	0.070	0.069
PP8 `PDF4LHC15` NP14 (NNLO Rew.)	24.50	-0.02	1.000	0.248	0.070	0.069
PP8 `PDF4LHC15` NP15 (NNLO Rew.)	24.50	-0.04	1.000	0.248	0.070	0.069
PP8 `PDF4LHC15` NP16 (NNLO Rew.)	24.52	0.05	1.000	0.248	0.070	0.069
PP8 `PDF4LHC15` NP17 (NNLO Rew.)	24.49	-0.05	1.001	0.248	0.070	0.069
PP8 `PDF4LHC15` NP18 (NNLO Rew.)	24.52	0.06	0.999	0.248	0.070	0.069
PP8 `PDF4LHC15` NP19 (NNLO Rew.)	24.49	-0.05	1.000	0.248	0.070	0.069
PP8 `PDF4LHC15` NP20 (NNLO Rew.)	24.51	0.02	1.000	0.248	0.070	0.069
PP8 `PDF4LHC15` NP21 (NNLO Rew.)	24.43	-0.30	1.003	0.248	0.070	0.069
PP8 `PDF4LHC15` NP22 (NNLO Rew.)	24.51	-0.00	1.000	0.248	0.070	0.069
PP8 `PDF4LHC15` NP23 (NNLO Rew.)	24.51	0.00	1.000	0.248	0.070	0.069
PP8 `PDF4LHC15` NP24 (NNLO Rew.)	24.51	-0.01	1.000	0.248	0.070	0.069
PP8 `PDF4LHC15` NP25 (NNLO Rew.)	24.52	0.05	1.000	0.248	0.070	0.069
PP8 `PDF4LHC15` NP26 (NNLO Rew.)	24.51	0.03	1.000	0.248	0.070	0.069
PP8 `PDF4LHC15` NP27 (NNLO Rew.)	24.54	0.15	0.999	0.248	0.070	0.069
PP8 `PDF4LHC15` NP28 (NNLO Rew.)	24.51	-0.00	1.000	0.248	0.070	0.069
PP8 `PDF4LHC15` NP29 (NNLO Rew.)	24.51	-0.00	1.000	0.248	0.070	0.069

Table 7.4.: Overview of particle-level acceptances and correction factors C^i in each of the three signal regions for different $t\bar{t}$ samples. The first listed sample in each section is considered as the nominal setting. As in the inclusive cross section fit, all alternative samples (including the PDF variations) are reweighted to the same NNLO QCD + NLO EW top-quark p_{T} distribution. The ratios of the acceptances $\frac{A_{\text{nom}}}{A_{\text{alt}}}$ are used to rescale the alternative $t\bar{t}$ distributions in order to ensure a proper estimation of modelling uncertainties in the fiducial cross section measurement.

Finally, the fit described in Section 7.2 is repeated with the adjusted $t\bar{t}$ modelling uncertainties. It turns out that the pulls and constraints of all nuisance parameters are exactly the same as in the inclusive measurement. This is not surprising because they mainly originate from shape variations which are not changed in the fiducial cross section measurement. The measured signal strength is

$$\mu_{\text{fid}} = 0.9845^{+0.0383}_{-0.0376}\,. \tag{7.6}$$

Multiplying this value with the reference cross section of 112.2 pb, the measured fiducial cross section is determined to be

$$\sigma_{\text{fid}} = 110.5^{+4.3}_{-4.2}\ \text{pb}\,, \tag{7.7}$$

where the total uncertainty corresponds to a precision of 3.9%. As expected, this measurement achieves a higher precision than the inclusive cross section measurement (4.3%). The reduction of the uncertainty is mainly due to the reduced impact of the parton shower and hadronisation modelling uncertainty on the acceptance (1.8% vs. 2.1%). The breakdown of systematic uncertainties is given in Table 7.5. To simplify the comparison, the corresponding impacts in the inclusive cross section measurement (see Table 7.2) are also shown here. One can see that, compared to the inclusive measurement, the contributions from $t\bar{t}$ modelling uncertainties are significantly reduced. The impacts of other uncertainties, e.g. related to detector modelling, are of a similar order of magnitude. This is expected because only the $t\bar{t}$ modelling uncertainties are modified for the fiducial measurement. The small differences between these impacts in both measurements can be explained by the fact that the breakdown of uncertainties (obtained by subtracting uncertainties in quadrature) only provides an approximation of the various contributions.

Category	$\frac{\Delta\sigma_{\text{fid}}}{\sigma_{\text{fid}}}$ [%]		$\frac{\Delta\sigma_{\text{inc}}}{\sigma_{\text{inc}}}$ [%]	
Signal modelling				
$t\bar{t}$ shower/hadronisation	+2.0	−1.9	+3.1	−2.8
$t\bar{t}$ scale and PDF variations	+1.4	−1.3	+2.0	−1.8
Background modelling				
MC background modelling	+1.3	−1.5	+1.5	−1.4
Multijet background	+0.5	−0.7	+0.8	−0.8
Detector modelling				
Jet reconstruction	+2.0	−2.1	+1.9	−1.9
Luminosity	+1.8	−1.7	+1.9	−1.7
Flavour tagging	+1.3	−1.4	+1.2	−1.4
E_T^{miss} + pile-up	+0.4	−0.2	+0.5	−0.4
Muon reconstruction	+0.4	−0.4	+0.5	−0.3
Electron reconstruction	+0.3	−0.3	+0.2	−0.4
Simulation stat. uncertainty	+0.6	−0.6	+0.8	−0.6
Total systematic uncertainty	+3.9	−3.8	+4.3	−4.2
Data stat. uncertainty	+0.05	−0.05	+0.05	−0.05
Total uncertainty	+3.9	−3.8	+4.3	−4.2

Table 7.5.: The contributions of systematic uncertainties, grouped into categories, to the uncertainties on the measured fiducial and inclusive cross sections. The impact of each category is evaluated by performing the fit while all NPs in the respective category are fixed to their post-fit values. The uncertainty in this fit is then subtracted in quadrature from the total uncertainty in order to estimate the contribution.

8. Summary and Outlook

This thesis presented a first measurement of the inclusive and fiducial $t\bar{t}$ production cross section in the lepton+jets channel using proton-proton collision data recorded with the ATLAS detector at $\sqrt{s} = 13$ TeV, corresponding to an integrated luminosity of 139 fb^{-1}. Events with exactly one charged lepton (e or μ), missing transverse energy, and at least four jets with either one or two b-tags were analysed, while events with more than two b-tags were discarded due to their small contribution and the large mismodelling of $t\bar{t}$+heavy-flavour jets production. The selected events were split into three orthogonal signal regions according to their jet and b-tag multiplicities. In each region, a unique variable was selected which provides separation power from backgrounds and at the same time is less sensitive to modelling uncertainties. Finally, a profile likelihood technique was used for a simultaneous fit of these three regions, which allowed to incorporate systematic uncertainties as nuisance parameters directly into the likelihood function. This method helped to constrain systematic uncertainties but especially to exploit the correlations between them, resulting in a significant reduction of the uncertainty on the cross section. The fit to data yields

$$\sigma_{\text{inc}}(t\bar{t}) = 829.7^{+35.3}_{-34.5}\ \text{pb}\,, \tag{8.1}$$

assuming a top-quark mass of $m_t = 172.5$ GeV. The uncertainty corresponds to a precision of 4.3% and the result is in very good agreement with the NNLO+NNLL prediction of 831.76 pb. The dependence on the assumed top-quark mass in the fit configuration is found to be in the order of 1.3%/GeV. The measurement of the cross section in the fiducial region defined in Section 7.6 yields

$$\sigma_{\text{fid}}(t\bar{t}) = 110.5^{+4.3}_{-4.2}\ \text{pb} \tag{8.2}$$

with an uncertainty of 3.9%. The decrease of the uncertainty is due to the smaller impact of modelling, especially of the parton shower uncertainty on the acceptance.

Several problems related to $t\bar{t}$ modelling uncertainties were faced during the development of this analysis. In the initial stage, recommended prescriptions were used to

evaluate the modelling uncertainties but they resulted in too large constraints. The main reason for this issue was the usage of so-called two-point systematics (i.e. uncertainties which are estimated by simply comparing two models) which are not well-suited for being used in a profile likelihood fit. Therefore, constraints on such uncertainties are not surprising and occur because several parameters are changed at the same time leading to large effects on the distributions exploited in the fit. Also, the interpolation of these effects, which is needed in a profile likelihood fit, is not necessarily validated. The constraints were relaxed by making the fit configuration much more flexible. The original prescriptions were adjusted and uncertainties were split into several components (e.g. variation of the renormalisation scale). This procedure was well-motivated because nuisance parameters in a likelihood function are supposed to reflect the variation of a certain parameter. However, such a splitting was not possible for the parton shower uncertainty, estimated by the comparison of the distributions obtained with the Powheg-Box + Pythia 8 and the Powheg-Box + Herwig 7 sample. In this comparison, several parameters are changed at the same time resulting in large effects. Finally, the large constraints were mitigated by splitting this uncertainty into five components: Decorrelated shape effects in each region, migration of events between the regions, and the pure acceptance difference between both samples. Especially, the splitting of the normalisation effect into a migration and an acceptance component was needed to avoid the propagation of the large constraint on the event migration to the acceptance effect.

Since the profile likelihood technique is now used in several Atlas analyses, and will presumably become the standard fit method, the prescriptions for estimating modelling uncertainties have to be modified and new procedures have to be developed. This is much-needed to ensure a reasonable and validated treatment in profile likelihood fits. In the future, modelling uncertainties should be evaluated by varying only one parameter at the same time, which would allow the variations to be used in profiling. Ideally, this should be done by reweighting the nominal MC sample (as it is already done here, apart from the parton shower uncertainty). In this measurement, the parton shower and hadronisation uncertainty was split into five components, which probably results in too conservative uncertainties, especially because it dominates the uncertainty on the extracted cross section. Therefore, once new validated prescriptions are available for modelling uncertainties in profile likelihood fits, a reduction of the cross section uncertainty can be expected in future measurements at $\sqrt{s} = 13$ TeV and hopefully soon at 14 TeV.

A. Sample List

This appendix contains a list of all the samples used for the analysis. All MC samples are available in three different campaigns (`mc16a`, `mc16d`, `mc16e`) which are not listed separately here.

Data

data15_13TeV.AllYear.physics_Main.PhysCont.DAOD_TOPQ1.grp15
data16_13TeV.AllYear.physics_Main.PhysCont.DAOD_TOPQ1.grp16
data17_13TeV.AllYear.physics_Main.PhysCont.DAOD_TOPQ1.grp17
data18_13TeV.AllYear.physics_Main.PhysCont.DAOD_TOPQ1.grp18

$t\bar{t}$ Powheg-Box + Pythia 8

mc16_13TeV.410470.PhPy8EG_A14_ttbar_hdamp258p75_nonallhad.deriv.DAOD_TOPQ1

$t\bar{t}$ Powheg-Box + Herwig 7

mc16_13TeV.410557.PowhegHerwig7EvtGen_H7UE_tt_hdamp258p75_704_SingleLep.deriv.DAOD_TOPQ1
mc16_13TeV.410558.PowhegHerwig7EvtGen_H7UE_tt_hdamp258p75_704_dil.deriv.DAOD_TOPQ1

$t\bar{t}$ Powheg-Box + Pythia 8 (alternative top-quark masses)

mc16_13TeV.411045.PowhegPythia8EvtGen_ttbar_171p00_SingleLep.deriv.DAOD_TOPQ1
mc16_13TeV.411046.PowhegPythia8EvtGen_ttbar_172p00_SingleLep.deriv.DAOD_TOPQ1
mc16_13TeV.411049.PowhegPythia8EvtGen_ttbar_173p00_SingleLep.deriv.DAOD_TOPQ1
mc16_13TeV.411050.PowhegPythia8EvtGen_ttbar_174p00_SingleLep.deriv.DAOD_TOPQ1
mc16_13TeV.411053.PowhegPythia8EvtGen_ttbar_171p00_dilep.deriv.DAOD_TOPQ1
mc16_13TeV.411054.PowhegPythia8EvtGen_ttbar_172p00_dilep.deriv.DAOD_TOPQ1
mc16_13TeV.411057.PowhegPythia8EvtGen_ttbar_173p00_dilep.deriv.DAOD_TOPQ1
mc16_13TeV.411058.PowhegPythia8EvtGen_ttbar_174p00_dilep.deriv.DAOD_TOPQ1

Single top Powheg-Box + Pythia 8

mc16_13TeV.410644.PowhegPythia8EvtGen_A14_singletop_schan_lept_top.deriv.DAOD_TOPQ1
mc16_13TeV.410645.PowhegPythia8EvtGen_A14_singletop_schan_lept_antitop.deriv.DAOD_TOPQ1
mc16_13TeV.410646.PowhegPythia8EvtGen_A14_Wt_DR_inclusive_top.deriv.DAOD_TOPQ1
mc16_13TeV.410647.PowhegPythia8EvtGen_A14_Wt_DR_inclusive_antitop.deriv.DAOD_TOPQ1
mc16_13TeV.410654.PowhegPythia8EvtGen_A14_Wt_DS_inclusive_top.deriv.DAOD_TOPQ1
mc16_13TeV.410655.PowhegPythia8EvtGen_A14_Wt_DS_inclusive_antitop.deriv.DAOD_TOPQ1
mc16_13TeV.410658.PhPy8EG_A14_tchan_BW50_lept_top.deriv.DAOD_TOPQ1
mc16_13TeV.410659.PhPy8EG_A14_tchan_BW50_lept_antitop.deriv.DAOD_TOPQ1

Single top Powheg-Box + Herwig 7

mc16_13TeV.411032.PowhegHerwig7EvtGen_H7UE_704_tchan_lept_antitop.deriv.DAOD_TOPQ1
mc16_13TeV.411033.PowhegHerwig7EvtGen_H7UE_704_tchan_lept_top.deriv.DAOD_TOPQ1
mc16_13TeV.411034.PhHerwig7EG_H7UE_singletop_schan_lept_top.deriv.DAOD_TOPQ1

mc16_13TeV.411035.PhHerwig7EG_H7UE_singletop_schan_lept_antitop.deriv.DAOD_TOPQ1
mc16_13TeV.411036.PowhegHerwig7EvtGen_H7UE_Wt_DR_inclusive_top.deriv.DAOD_TOPQ1
mc16_13TeV.411037.PowhegHerwig7EvtGen_H7UE_Wt_DR_inclusive_antitop.deriv.DAOD_TOPQ1

$W+$ jets

mc16_13TeV.364156.Sherpa_221_NNPDF30NNLO_Wmunu_MAXHTPTV0_70_CVetoBVeto.deriv.DAOD_TOPQ1
mc16_13TeV.364157.Sherpa_221_NNPDF30NNLO_Wmunu_MAXHTPTV0_70_CFilterBVeto.deriv.DAOD_TOPQ1
mc16_13TeV.364158.Sherpa_221_NNPDF30NNLO_Wmunu_MAXHTPTV0_70_BFilter.deriv.DAOD_TOPQ1
mc16_13TeV.364159.Sherpa_221_NNPDF30NNLO_Wmunu_MAXHTPTV70_140_CVetoBVeto.deriv.DAOD_TOPQ1
mc16_13TeV.364160.Sherpa_221_NNPDF30NNLO_Wmunu_MAXHTPTV70_140_CFilterBVeto.deriv.DAOD_TOPQ1
mc16_13TeV.364161.Sherpa_221_NNPDF30NNLO_Wmunu_MAXHTPTV70_140_BFilter.deriv.DAOD_TOPQ1
mc16_13TeV.364162.Sherpa_221_NNPDF30NNLO_Wmunu_MAXHTPTV140_280_CVetoBVeto.deriv.DAOD_TOPQ1
mc16_13TeV.364163.Sherpa_221_NNPDF30NNLO_Wmunu_MAXHTPTV140_280_CFilterBVeto.deriv.DAOD_TOPQ1
mc16_13TeV.364164.Sherpa_221_NNPDF30NNLO_Wmunu_MAXHTPTV140_280_BFilter.deriv.DAOD_TOPQ1
mc16_13TeV.364165.Sherpa_221_NNPDF30NNLO_Wmunu_MAXHTPTV280_500_CVetoBVeto.deriv.DAOD_TOPQ1
mc16_13TeV.364166.Sherpa_221_NNPDF30NNLO_Wmunu_MAXHTPTV280_500_CFilterBVeto.deriv.DAOD_TOPQ1
mc16_13TeV.364167.Sherpa_221_NNPDF30NNLO_Wmunu_MAXHTPTV280_500_BFilter.deriv.DAOD_TOPQ1
mc16_13TeV.364168.Sherpa_221_NNPDF30NNLO_Wmunu_MAXHTPTV500_1000.deriv.DAOD_TOPQ1
mc16_13TeV.364169.Sherpa_221_NNPDF30NNLO_Wmunu_MAXHTPTV1000_E_CMS.deriv.DAOD_TOPQ1
mc16_13TeV.364170.Sherpa_221_NNPDF30NNLO_Wenu_MAXHTPTV0_70_CVetoBVeto.deriv.DAOD_TOPQ1
mc16_13TeV.364171.Sherpa_221_NNPDF30NNLO_Wenu_MAXHTPTV0_70_CFilterBVeto.deriv.DAOD_TOPQ1
mc16_13TeV.364172.Sherpa_221_NNPDF30NNLO_Wenu_MAXHTPTV0_70_BFilter.deriv.DAOD_TOPQ1
mc16_13TeV.364173.Sherpa_221_NNPDF30NNLO_Wenu_MAXHTPTV70_140_CVetoBVeto.deriv.DAOD_TOPQ1
mc16_13TeV.364174.Sherpa_221_NNPDF30NNLO_Wenu_MAXHTPTV70_140_CFilterBVeto.deriv.DAOD_TOPQ1
mc16_13TeV.364175.Sherpa_221_NNPDF30NNLO_Wenu_MAXHTPTV70_140_BFilter.deriv.DAOD_TOPQ1
mc16_13TeV.364176.Sherpa_221_NNPDF30NNLO_Wenu_MAXHTPTV140_280_CVetoBVeto.deriv.DAOD_TOPQ1
mc16_13TeV.364177.Sherpa_221_NNPDF30NNLO_Wenu_MAXHTPTV140_280_CFilterBVeto.deriv.DAOD_TOPQ1
mc16_13TeV.364178.Sherpa_221_NNPDF30NNLO_Wenu_MAXHTPTV140_280_BFilter.deriv.DAOD_TOPQ1
mc16_13TeV.364179.Sherpa_221_NNPDF30NNLO_Wenu_MAXHTPTV280_500_CVetoBVeto.deriv.DAOD_TOPQ1
mc16_13TeV.364180.Sherpa_221_NNPDF30NNLO_Wenu_MAXHTPTV280_500_CFilterBVeto.deriv.DAOD_TOPQ1
mc16_13TeV.364181.Sherpa_221_NNPDF30NNLO_Wenu_MAXHTPTV280_500_BFilter.deriv.DAOD_TOPQ1
mc16_13TeV.364182.Sherpa_221_NNPDF30NNLO_Wenu_MAXHTPTV500_1000.deriv.DAOD_TOPQ1
mc16_13TeV.364183.Sherpa_221_NNPDF30NNLO_Wenu_MAXHTPTV1000_E_CMS.deriv.DAOD_TOPQ1
mc16_13TeV.364184.Sherpa_221_NNPDF30NNLO_Wtaunu_MAXHTPTV0_70_CVetoBVeto.deriv.DAOD_TOPQ1
mc16_13TeV.364185.Sherpa_221_NNPDF30NNLO_Wtaunu_MAXHTPTV0_70_CFilterBVeto.deriv.DAOD_TOPQ1
mc16_13TeV.364186.Sherpa_221_NNPDF30NNLO_Wtaunu_MAXHTPTV0_70_BFilter.deriv.DAOD_TOPQ1
mc16_13TeV.364187.Sherpa_221_NNPDF30NNLO_Wtaunu_MAXHTPTV70_140_CVetoBVeto.deriv.DAOD_TOPQ1
mc16_13TeV.364188.Sherpa_221_NNPDF30NNLO_Wtaunu_MAXHTPTV70_140_CFilterBVeto.deriv.DAOD_TOPQ1
mc16_13TeV.364189.Sherpa_221_NNPDF30NNLO_Wtaunu_MAXHTPTV70_140_BFilter.deriv.DAOD_TOPQ1
mc16_13TeV.364190.Sherpa_221_NNPDF30NNLO_Wtaunu_MAXHTPTV140_280_CVetoBVeto.deriv.DAOD_TOPQ1
mc16_13TeV.364191.Sherpa_221_NNPDF30NNLO_Wtaunu_MAXHTPTV140_280_CFilterBVeto.deriv.DAOD_TOPQ1
mc16_13TeV.364192.Sherpa_221_NNPDF30NNLO_Wtaunu_MAXHTPTV140_280_BFilter.deriv.DAOD_TOPQ1
mc16_13TeV.364193.Sherpa_221_NNPDF30NNLO_Wtaunu_MAXHTPTV280_500_CVetoBVeto.deriv.DAOD_TOPQ1
mc16_13TeV.364194.Sherpa_221_NNPDF30NNLO_Wtaunu_MAXHTPTV280_500_CFilterBVeto.deriv.DAOD_TOPQ1
mc16_13TeV.364195.Sherpa_221_NNPDF30NNLO_Wtaunu_MAXHTPTV280_500_BFilter.deriv.DAOD_TOPQ1
mc16_13TeV.364196.Sherpa_221_NNPDF30NNLO_Wtaunu_MAXHTPTV500_1000.deriv.DAOD_TOPQ1
mc16_13TeV.364197.Sherpa_221_NNPDF30NNLO_Wtaunu_MAXHTPTV1000_E_CMS.deriv.DAOD_TOPQ1

$Z+$ jets

mc16_13TeV.364100.Sherpa_221_NNPDF30NNLO_Zmumu_MAXHTPTV0_70_CVetoBVeto.deriv.DAOD_TOPQ1
mc16_13TeV.364101.Sherpa_221_NNPDF30NNLO_Zmumu_MAXHTPTV0_70_CFilterBVeto.deriv.DAOD_TOPQ1
mc16_13TeV.364102.Sherpa_221_NNPDF30NNLO_Zmumu_MAXHTPTV0_70_BFilter.deriv.DAOD_TOPQ1
mc16_13TeV.364103.Sherpa_221_NNPDF30NNLO_Zmumu_MAXHTPTV70_140_CVetoBVeto.deriv.DAOD_TOPQ1
mc16_13TeV.364104.Sherpa_221_NNPDF30NNLO_Zmumu_MAXHTPTV70_140_CFilterBVeto.deriv.DAOD_TOPQ1
mc16_13TeV.364105.Sherpa_221_NNPDF30NNLO_Zmumu_MAXHTPTV70_140_BFilter.deriv.DAOD_TOPQ1
mc16_13TeV.364106.Sherpa_221_NNPDF30NNLO_Zmumu_MAXHTPTV140_280_CVetoBVeto.deriv.DAOD_TOPQ1
mc16_13TeV.364107.Sherpa_221_NNPDF30NNLO_Zmumu_MAXHTPTV140_280_CFilterBVeto.deriv.DAOD_TOPQ1
mc16_13TeV.364108.Sherpa_221_NNPDF30NNLO_Zmumu_MAXHTPTV140_280_BFilter.deriv.DAOD_TOPQ1
mc16_13TeV.364109.Sherpa_221_NNPDF30NNLO_Zmumu_MAXHTPTV280_500_CVetoBVeto.deriv.DAOD_TOPQ1
mc16_13TeV.364110.Sherpa_221_NNPDF30NNLO_Zmumu_MAXHTPTV280_500_CFilterBVeto.deriv.DAOD_TOPQ1
mc16_13TeV.364111.Sherpa_221_NNPDF30NNLO_Zmumu_MAXHTPTV280_500_BFilter.deriv.DAOD_TOPQ1
mc16_13TeV.364112.Sherpa_221_NNPDF30NNLO_Zmumu_MAXHTPTV500_1000.deriv.DAOD_TOPQ1
mc16_13TeV.364113.Sherpa_221_NNPDF30NNLO_Zmumu_MAXHTPTV1000_E_CMS.deriv.DAOD_TOPQ1
mc16_13TeV.364114.Sherpa_221_NNPDF30NNLO_Zee_MAXHTPTV0_70_CVetoBVeto.deriv.DAOD_TOPQ1
mc16_13TeV.364115.Sherpa_221_NNPDF30NNLO_Zee_MAXHTPTV0_70_CFilterBVeto.deriv.DAOD_TOPQ1
mc16_13TeV.364116.Sherpa_221_NNPDF30NNLO_Zee_MAXHTPTV0_70_BFilter.deriv.DAOD_TOPQ1
mc16_13TeV.364117.Sherpa_221_NNPDF30NNLO_Zee_MAXHTPTV70_140_CVetoBVeto.deriv.DAOD_TOPQ1
mc16_13TeV.364118.Sherpa_221_NNPDF30NNLO_Zee_MAXHTPTV70_140_CFilterBVeto.deriv.DAOD_TOPQ1
mc16_13TeV.364119.Sherpa_221_NNPDF30NNLO_Zee_MAXHTPTV70_140_BFilter.deriv.DAOD_TOPQ1
mc16_13TeV.364120.Sherpa_221_NNPDF30NNLO_Zee_MAXHTPTV140_280_CVetoBVeto.deriv.DAOD_TOPQ1
mc16_13TeV.364121.Sherpa_221_NNPDF30NNLO_Zee_MAXHTPTV140_280_CFilterBVeto.deriv.DAOD_TOPQ1
mc16_13TeV.364122.Sherpa_221_NNPDF30NNLO_Zee_MAXHTPTV140_280_BFilter.deriv.DAOD_TOPQ1
mc16_13TeV.364123.Sherpa_221_NNPDF30NNLO_Zee_MAXHTPTV280_500_CVetoBVeto.deriv.DAOD_TOPQ1
mc16_13TeV.364124.Sherpa_221_NNPDF30NNLO_Zee_MAXHTPTV280_500_CFilterBVeto.deriv.DAOD_TOPQ1
mc16_13TeV.364125.Sherpa_221_NNPDF30NNLO_Zee_MAXHTPTV280_500_BFilter.deriv.DAOD_TOPQ1
mc16_13TeV.364126.Sherpa_221_NNPDF30NNLO_Zee_MAXHTPTV500_1000.deriv.DAOD_TOPQ1
mc16_13TeV.364127.Sherpa_221_NNPDF30NNLO_Zee_MAXHTPTV1000_E_CMS.deriv.DAOD_TOPQ1
mc16_13TeV.364128.Sherpa_221_NNPDF30NNLO_Ztautau_MAXHTPTV0_70_CVetoBVeto.deriv.DAOD_TOPQ1
mc16_13TeV.364129.Sherpa_221_NNPDF30NNLO_Ztautau_MAXHTPTV0_70_CFilterBVeto.deriv.DAOD_TOPQ1
mc16_13TeV.364130.Sherpa_221_NNPDF30NNLO_Ztautau_MAXHTPTV0_70_BFilter.deriv.DAOD_TOPQ1
mc16_13TeV.364131.Sherpa_221_NNPDF30NNLO_Ztautau_MAXHTPTV70_140_CVetoBVeto.deriv.DAOD_TOPQ1
mc16_13TeV.364132.Sherpa_221_NNPDF30NNLO_Ztautau_MAXHTPTV70_140_CFilterBVeto.deriv.DAOD_TOPQ1
mc16_13TeV.364133.Sherpa_221_NNPDF30NNLO_Ztautau_MAXHTPTV70_140_BFilter.deriv.DAOD_TOPQ1
mc16_13TeV.364134.Sherpa_221_NNPDF30NNLO_Ztautau_MAXHTPTV140_280_CVetoBVeto.deriv.DAOD_TOPQ1
mc16_13TeV.364135.Sherpa_221_NNPDF30NNLO_Ztautau_MAXHTPTV140_280_CFilterBVeto.deriv.DAOD_TOPQ1
mc16_13TeV.364136.Sherpa_221_NNPDF30NNLO_Ztautau_MAXHTPTV140_280_BFilter.deriv.DAOD_TOPQ1
mc16_13TeV.364137.Sherpa_221_NNPDF30NNLO_Ztautau_MAXHTPTV280_500_CVetoBVeto.deriv.DAOD_TOPQ1
mc16_13TeV.364138.Sherpa_221_NNPDF30NNLO_Ztautau_MAXHTPTV280_500_CFilterBVeto.deriv.DAOD_TOPQ1
mc16_13TeV.364139.Sherpa_221_NNPDF30NNLO_Ztautau_MAXHTPTV280_500_BFilter.deriv.DAOD_TOPQ1
mc16_13TeV.364140.Sherpa_221_NNPDF30NNLO_Ztautau_MAXHTPTV500_1000.deriv.DAOD_TOPQ1
mc16_13TeV.364141.Sherpa_221_NNPDF30NNLO_Ztautau_MAXHTPTV1000_E_CMS.deriv.DAOD_TOPQ1

Diboson

mc16_13TeV.363356.Sherpa_221_NNPDF30NNLO_ZqqZll.deriv.DAOD_TOPQ1
mc16_13TeV.363358.Sherpa_221_NNPDF30NNLO_WqqZll.deriv.DAOD_TOPQ1
mc16_13TeV.363359.Sherpa_221_NNPDF30NNLO_WpqqWmlv.deriv.DAOD_TOPQ1
mc16_13TeV.363360.Sherpa_221_NNPDF30NNLO_WplvWmqq.deriv.DAOD_TOPQ1
mc16_13TeV.363489.Sherpa_221_NNPDF30NNLO_WlvZqq.deriv.DAOD_TOPQ1
mc16_13TeV.364250.Sherpa_222_NNPDF30NNLO_llll.deriv.DAOD_TOPQ1
mc16_13TeV.364253.Sherpa_222_NNPDF30NNLO_lllv.deriv.DAOD_TOPQ1
mc16_13TeV.364254.Sherpa_222_NNPDF30NNLO_llvv.deriv.DAOD_TOPQ1
mc16_13TeV.364255.Sherpa_222_NNPDF30NNLO_lvvv.deriv.DAOD_TOPQ1

$t\bar{t}V$ ($V = W, Z$)

mc16_13TeV.410155.aMcAtNloPythia8EvtGen_MEN30NLO_A14N23LO_ttW.deriv.DAOD_TOPQ1
mc16_13TeV.410156.aMcAtNloPythia8EvtGen_MEN30NLO_A14N23LO_ttZnunu.deriv.DAOD_TOPQ1
mc16_13TeV.410157.aMcAtNloPythia8EvtGen_MEN30NLO_A14N23LO_ttZqq.deriv.DAOD_TOPQ1
mc16_13TeV.410218.aMcAtNloPythia8EvtGen_MEN30NLO_A14N23LO_ttee.deriv.DAOD_TOPQ1
mc16_13TeV.410219.aMcAtNloPythia8EvtGen_MEN30NLO_A14N23LO_ttmumu.deriv.DAOD_TOPQ1
mc16_13TeV.410220.aMcAtNloPythia8EvtGen_MEN30NLO_A14N23LO_tttautau.deriv.DAOD_TOPQ1

$t\bar{t}H$

mc16_13TeV.346343.PhPy8EG_A14NNPDF23_NNPDF30ME_ttH125_allhad.deriv.DAOD_TOPQ1
mc16_13TeV.346344.PhPy8EG_A14NNPDF23_NNPDF30ME_ttH125_semilep.deriv.DAOD_TOPQ1
mc16_13TeV.346345.PhPy8EG_A14NNPDF23_NNPDF30ME_ttH125_dilep.deriv.DAOD_TOPQ1

B. Top-Quark p_{T} Reweighting

This section presents plots which show the effect of the top-quark p_{T} reweighting when it is applied to $t\bar{t}$ events simulated with Powheg-Box + Pythia 8. The MC truth event information is used in order to reweight the top-quark p_{T} distribution in the MC to the NNLO QCD + NLO EW theory calculation [108] (in the full phase space). The distributions of the variables used in the fit (before and after reweighting) are shown in Figure B.1. As can be seen, the selected variables are not sensitive to the p_{T} mismodelling. The effect of the reweighting on selected p_{T} distributions is shown in Figure B.2. The reweighting can indeed improve the agreement between prediction and data but cannot fix the p_{T} mismodelling completely. Due to these observations, the reweighting effect is considered as a systematic uncertainty in the fit.

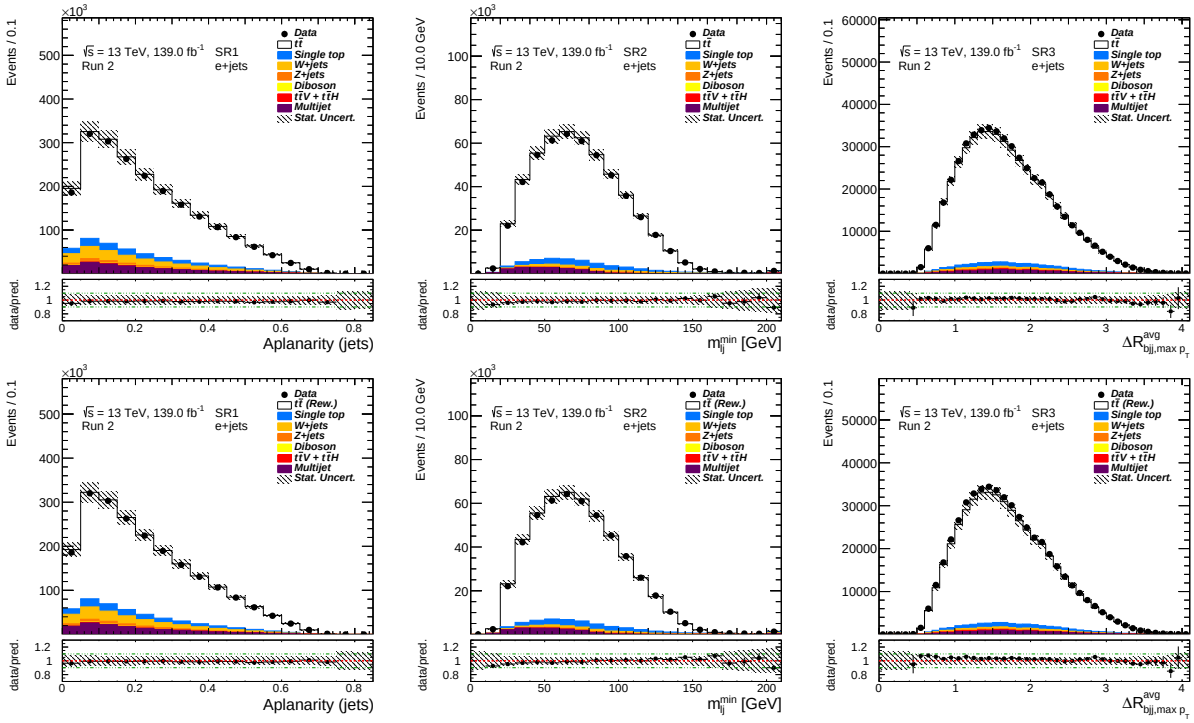

(a) e+jets: before (top) and after reweighting (bottom)

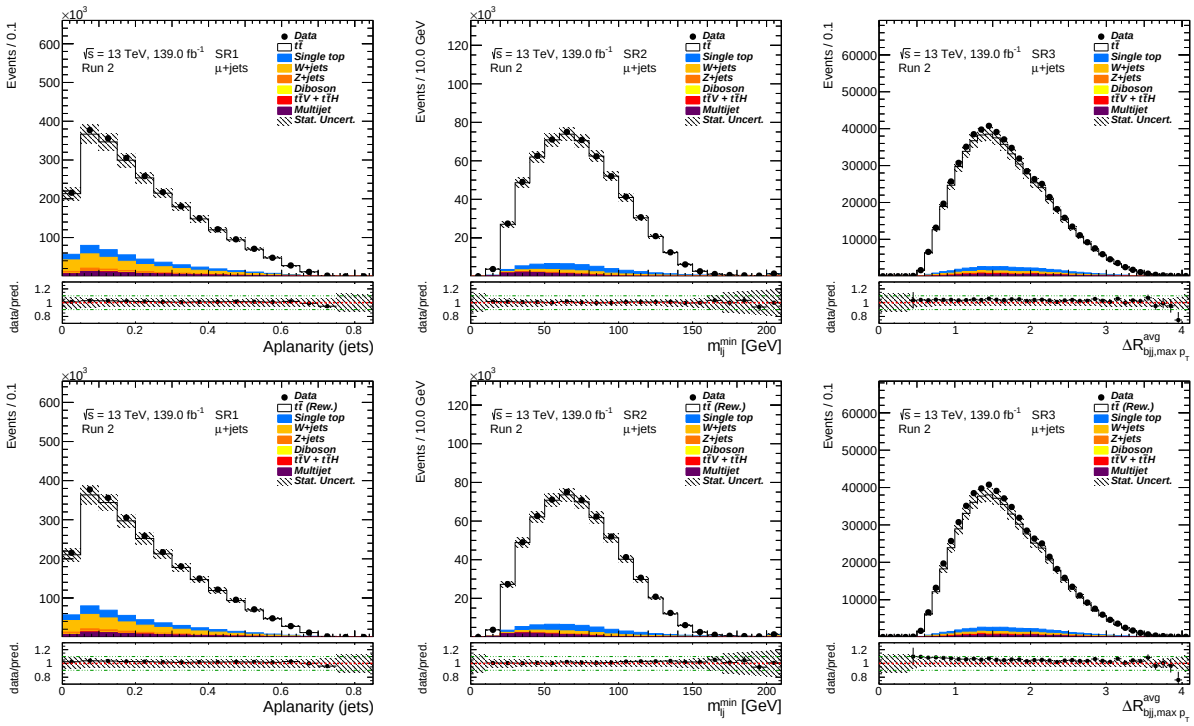

(b) μ+jets: before (top) and after reweighting (bottom)

Figure B.1.: Data/prediction agreement for the selected variables for the fit in the e+jets (a) and the μ+jets channel (b), before and after the top-quark p_{T} reweighting. The hashed bands show the statistical and normalisation uncertainty on each signal and background source. The first and last bin contain underflow and overflow events, respectively.

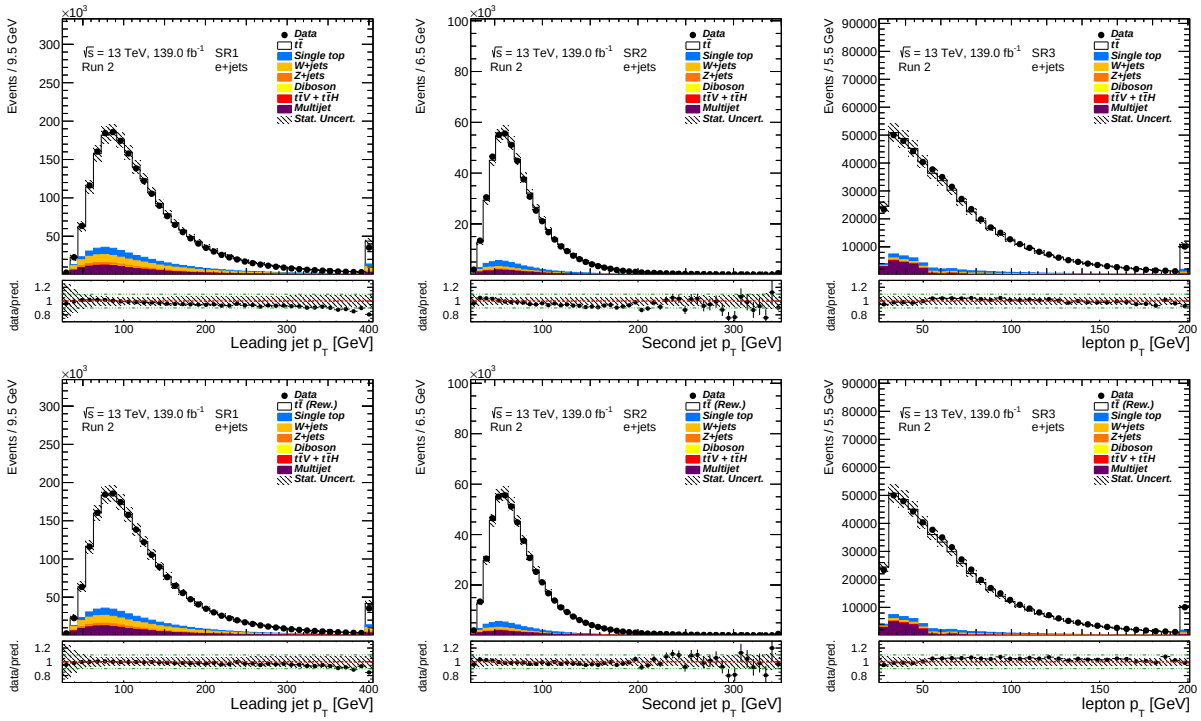

(a) e+jets: before (top) and after reweighting (bottom)

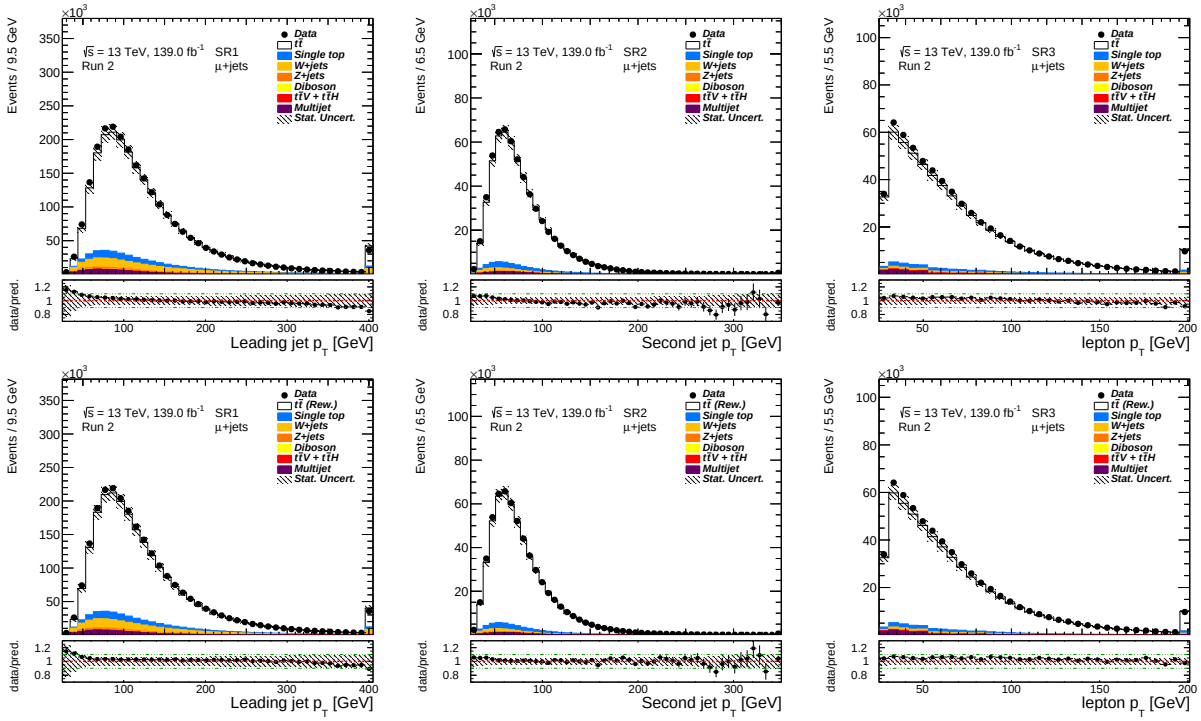

(b) μ+jets: before (top) and after reweighting (bottom)

Figure B.2.: Data/prediction agreement for p_{T} distributions in the e+jets (a) and the μ+jets channel (b), before and after the top-quark p_{T} reweighting in SR1, SR2, and SR3 (from left to right). The hashed bands show the statistical and normalisation uncertainty on each signal and background source. The first and last bin contain underflow and overflow events, respectively.

C. Considered Variables

The following table provides an overview of variables that were investigated for the possible usage in the profile likelihood fit. Variables like jet p_{T}, H_{T}, or invariant jet-pair masses are not listed here because they were excluded from the beginning due to their large $t\bar{t}$ modelling discrepancy.

Variable	**Definition**
ΔR_{jj}, ΔR_{bb}, ΔR_{ll}	ΔR between two jets/b-jets/untagged jets
ΔR_{j-lep}, ΔR_{b-lep}	ΔR between a jet/b-jet and the lepton
$\Delta R_{b70/77/85-lep}$	ΔR between the lepton and a b-jet (70, 77, or 85% WP)
ΔR_{b1-b2}	ΔR between the two jets with the highest b-tag scores
ΔR_{bj}, ΔR_{bl}	ΔR between a b-jet and another jet/untagged jet
$\Delta R_{j_1j_2}$, $\Delta R_{j_1j_3}$, $\Delta R_{j_2j_3}$	ΔR between two jets (first, second, and third leading jet)
$\Delta R^{\mathrm{max}}_{j3-b}$	Max. ΔR between a b-jet and the third leading jet
$\Delta R^{\mathrm{min}}_{b-ll}$	Min. ΔR between a b-jet and the four-vector calculated as the sum of the two leading untagged jets
$\Delta R^{\mathrm{min/max/avg}}_{bjj,\mathrm{max}\ p_{\mathrm{T}}}$	Min./max./average ΔR between the jets in the subsystem consisting of a b-jet and two other jets with maximum p_{T} (vector sum)
$m_{lb}^{\mathrm{min}\Delta R}$, $m_{lb70/77/85}^{\mathrm{min}\Delta R}$	Inv. mass of the lepton and the closest b-jet (60, 70, 77, or 85% WP)
m_{lj}	Inv. mass of the lepton and a jet
$m^{\mathrm{min}}_{lj,2}$	Second smallest lepton-jet mass
TWB 2	Second highest b-tag score among all jets
1. u-jet TWB	b-tag score of the leading untagged jet
$\lvert\eta\rvert_{\mathrm{max}}$ of u-jets	Max. absolute η value of untagged jets
$p_{\mathrm{T}}^{j2}/p_{\mathrm{T}}^{j1}$, $p_{\mathrm{T}}^{j3}/p_{\mathrm{T}}^{j2}$, $p_{\mathrm{T}}^{j4}/p_{\mathrm{T}}^{j3}$	Ratios between p_{T} of jets (first, second, third, and fourth leading jet)
$p_{\mathrm{T}}^{j4}/H_{\mathrm{T}}^{j1-j4}$	Ratio between p_{T} of fourth jet and scalar sum of p_{T} of first four jets
Sphericity, Aplanarity	Sphericity tensor (sum over all jets or jets and lepton): $S^{\alpha\beta} = \frac{\sum_i p_i^\alpha p_i^\beta}{\sum_i \lvert p_i\rvert^2}$ with smallest eigenvalues $\lambda_{2/3}$ Sphericity$=\frac{3}{2}(\lambda_2+\lambda_3)$ Aplanarity$=\frac{3}{2}\lambda_3$

Table C.1.: Definitions of all variables considered for the studies. The default b-tagging efficiency WP is 60%. Variables can also come along with suffixes (min., max., average, max. p_{T}) in case they are defined for several permutations of objects.

D. Additional Plots for the Fit

This appendix presents additional relevant plots regarding the profile likelihood fit. The effects of modelling uncertainties on the $t\bar{t}$ distributions in all three signal regions are shown in Figure D.1 (top quark p_{T} reweighting and parton shower uncertainties) and in Figure D.2 (ISR and FSR effects). The correlation matrices of the nuisance parameters, determined in the profile likelihood fit, are presented in Figure D.3 for the Asimov fit and in Figure D.4 for the fit to observed data.

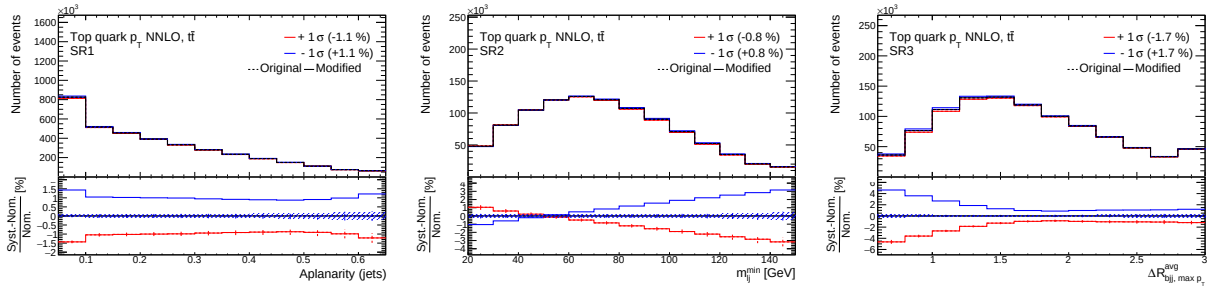

(a) Top-quark p_{T} reweighting

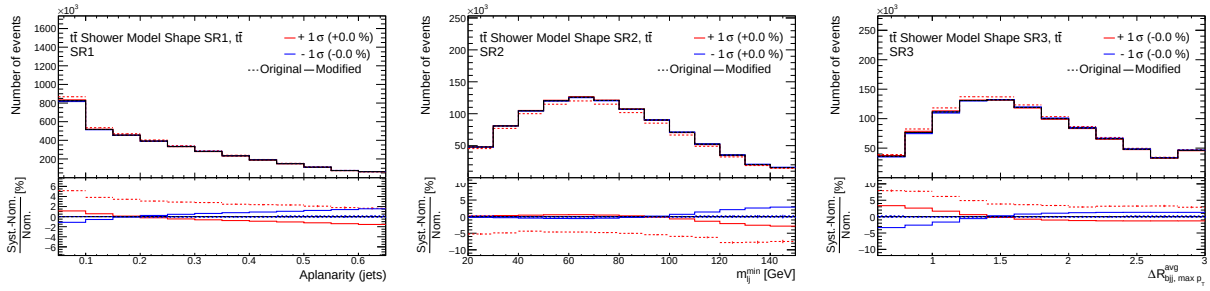

(b) $t\bar{t}$ parton shower/hadronisation: shape uncertainty

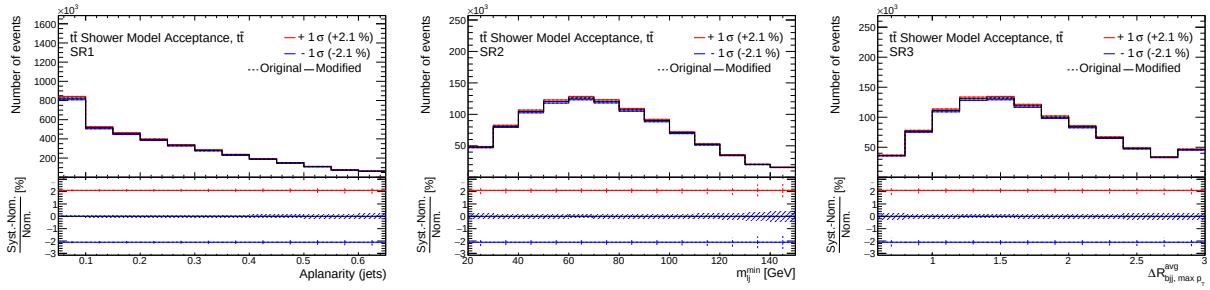

(c) $t\bar{t}$ parton shower/hadronisation: acceptance uncertainty

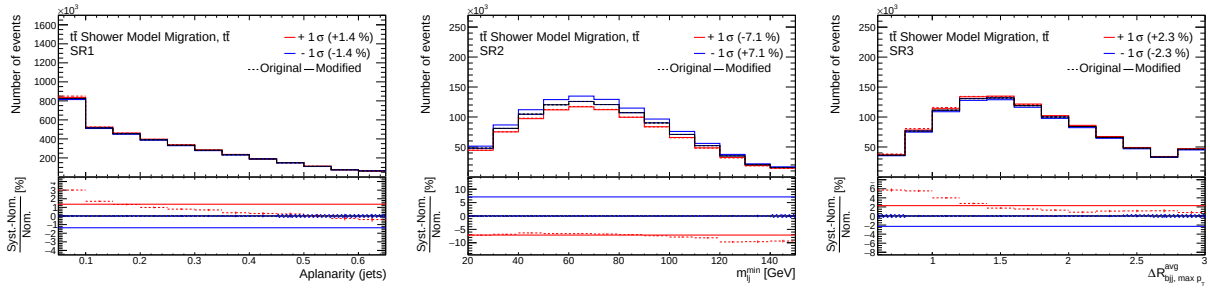

(d) $t\bar{t}$ parton shower/hadronisation: event migration

Figure D.1.: The effects of modelling uncertainties on the $t\bar{t}$ distributions in SR1, SR2, and SR3 (from left to right). Here, lines coloured in red/blue present the $\pm 1\sigma$ effect. The dotted/solid lines show the effect before/after smoothing (only for shower uncertainties), symmetrisation, and the removal of the normalisation or shape effect (only for pure shape or normalisation uncertainties). The dotted lines in Figure D.1d show, in contrast to Figure D.1b, the (reweighted) POWHEG-BOX + HERWIG 7 distributions which are scaled to the acceptance of the (reweighted) POWHEG-BOX + PYTHIA 8 sample for a proper description of the event migrations. The hashed bands represent the MC statistical uncertainties.

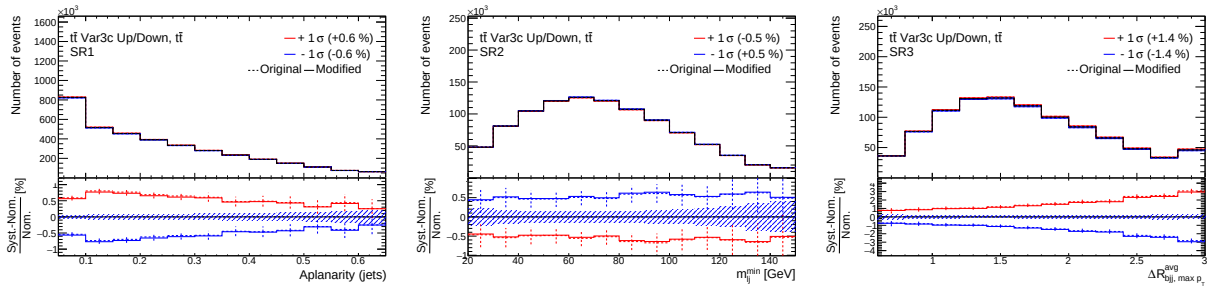

(a) $t\bar{t}$ `Var3c` variation

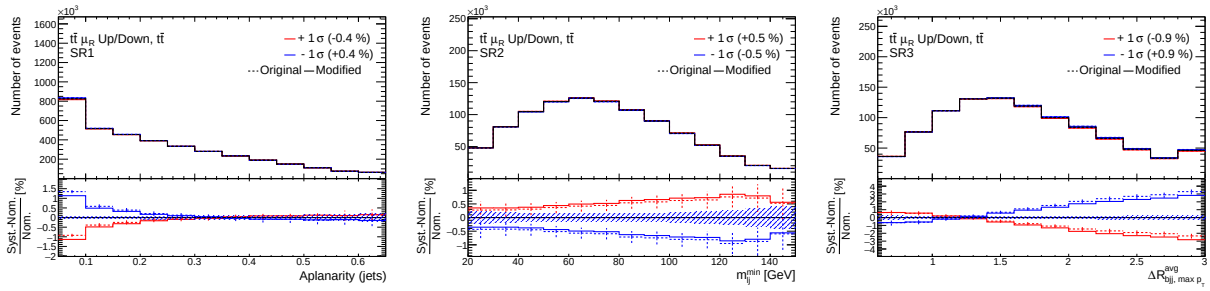

(b) $t\bar{t}$ μ_{R} variation

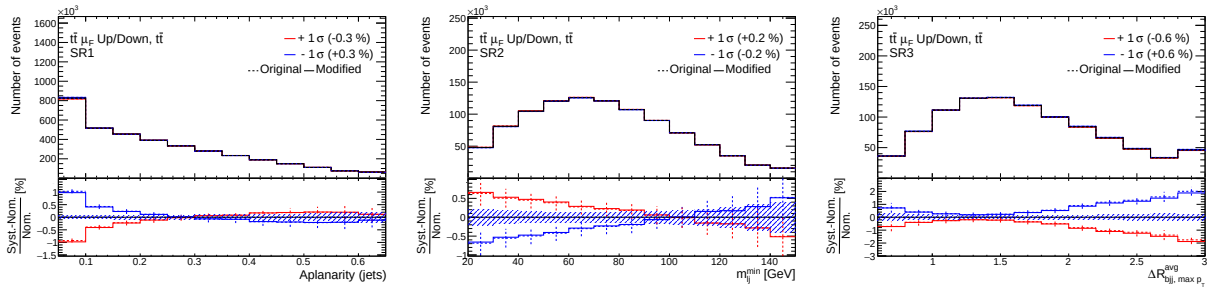

(c) $t\bar{t}$ μ_{F} variation

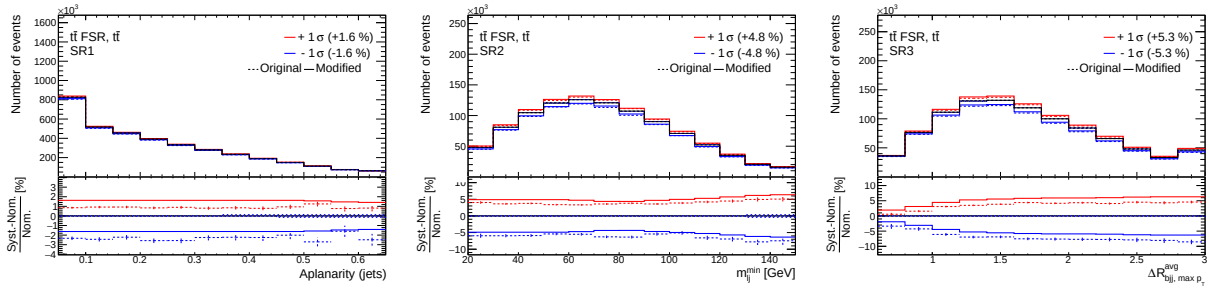

(d) $t\bar{t}$ FSR uncertainty

Figure D.2.: The effects of modelling uncertainties on the $t\bar{t}$ distributions in SR1, SR2, and SR3 (from left to right). Here, lines coloured in red/blue present the $\pm 1\sigma$ effect. The dotted/solid lines show the effect before/after smoothing (only for FSR uncertainties) and symmetrisation. The hashed bands represent the MC statistical uncertainties.

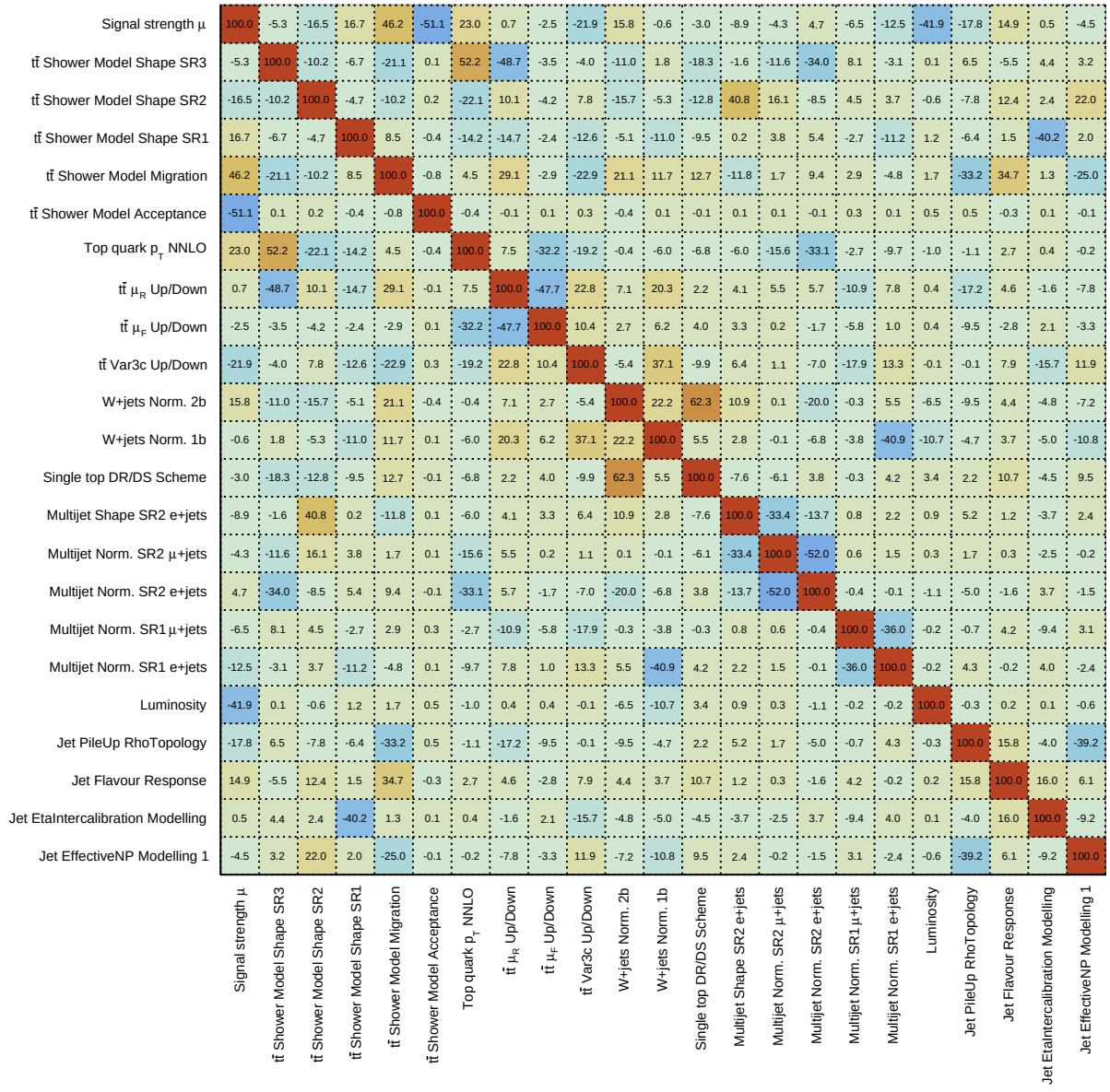

Figure D.3.: Correlations between all nuisance parameters and the signal strength μ obtained from the profile likelihood fit to Asimov data. Only NPs with at least one correlation larger than 30% are shown.

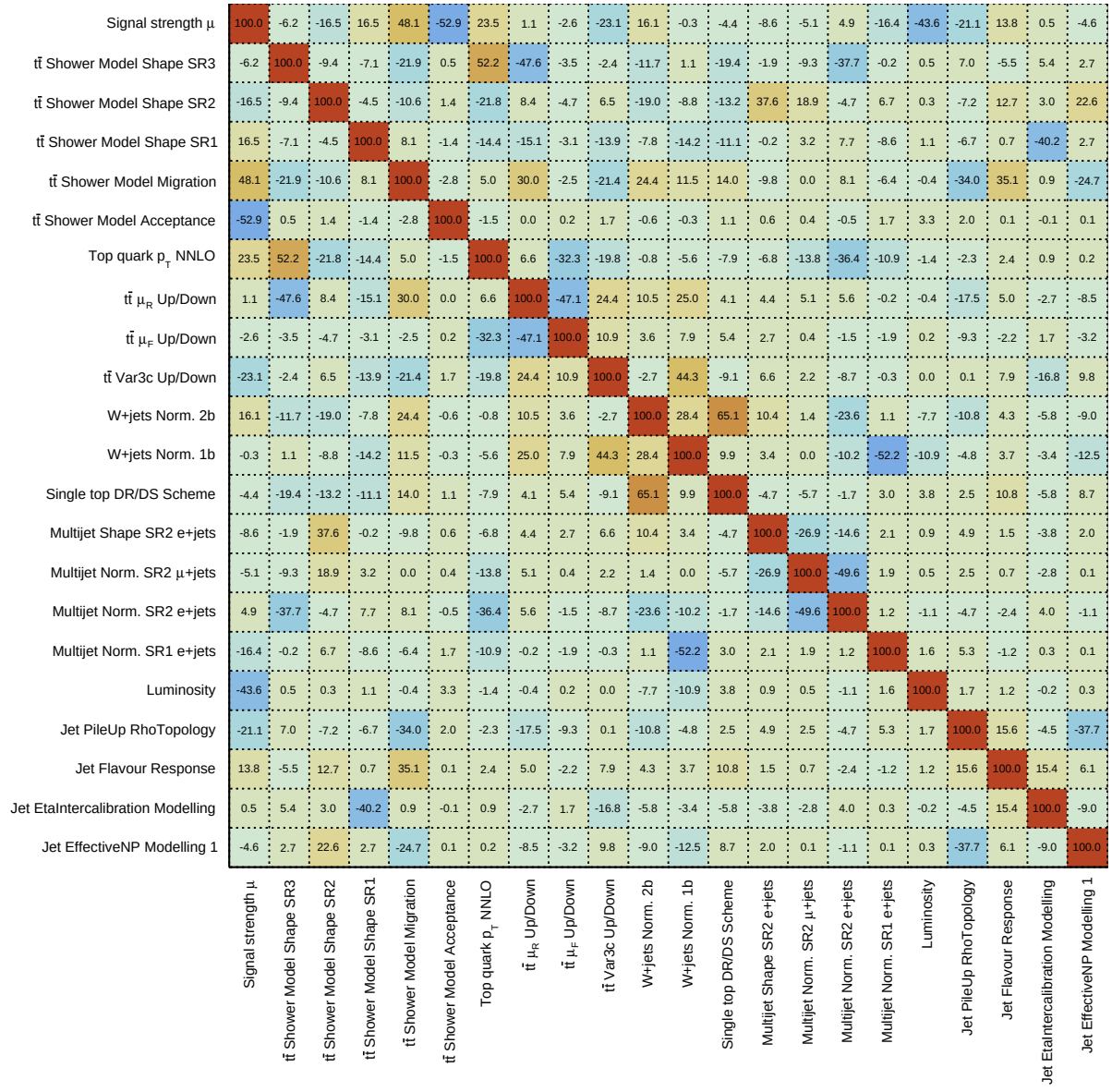

Figure D.4.: Correlations between all nuisance parameters and the signal strength μ obtained from the profile likelihood fit to observed data. Only NPs with at least one correlation larger than 30% are shown.

Bibliography

[1] A. Salam, J. C. Ward, *Electromagnetic and weak interactions*, Phys. Lett. **13**, 168 (1964)

[2] S. L. Glashow, *Partial Symmetries of Weak Interactions*, Nucl. Phys. **22**, 579 (1961)

[3] S. Weinberg, *A Model of Leptons*, Phys. Rev. Lett. **19**, 1264 (1967)

[4] S. L. Glashow, J. Iliopoulos, L. Maiani, *Weak Interactions with Lepton-Hadron Symmetry*, Phys. Rev. D **2**, 1285 (1970)

[5] D. J. Gross, F. Wilczek, *Ultraviolet Behavior of Nonabelian Gauge Theories*, Phys. Rev. Lett. **30**, 1343 (1973)

[6] H. D. Politzer, *Reliable Perturbative Results for Strong Interactions?*, Phys. Rev. Lett. **30**, 1346 (1973)

[7] H. D. Politzer, *Asymptotic Freedom: An Approach to Strong Interactions*, Phys. Rept. **14**, 129 (1974)

[8] F. Englert, R. Brout, *Broken Symmetry and the Mass of Gauge Vector Mesons*, Phys. Rev. Lett. **13**, 321 (1964)

[9] P. W. Higgs, *Broken symmetries, massless particles and gauge fields*, Phys. Lett. **12**, 132 (1964)

[10] P. W. Higgs, *Broken Symmetries and the Masses of Gauge Bosons*, Phys. Rev. Lett. **13**, 508 (1964)

[11] Atlas Collaboration, *Observation of a new particle in the search for the Standard Model Higgs boson with the ATLAS detector at the LHC*, Phys. Lett. B **716**, 1 (2012)

[12] Cms Collaboration, *Observation of a New Boson at a Mass of 125 GeV with the CMS Experiment at the LHC*, Phys. Lett. B **716**, 30 (2012)

[13] Y. Fukuda, et al. (Super-Kamiokande Collaboration), *Evidence for oscillation of atmospheric neutrinos*, Phys. Rev. Lett. **81**, 1562 (1998)

[14] Q. R. Ahmad, et al. (SNO Collaboration), *Measurement of the rate of* $\nu_e + d \rightarrow p + p + e^-$ *interactions produced by* ^8B *solar neutrinos at the Sudbury Neutrino Observatory*, Phys. Rev. Lett. **87**, 071301 (2001)

[15] Q. R. Ahmad, et al. (SNO Collaboration), *Direct evidence for neutrino flavor transformation from neutral current interactions in the Sudbury Neutrino Observatory*, Phys. Rev. Lett. **89**, 011301 (2002)

[16] S. Abachi, et al. (DØ Collaboration), *Observation of the top quark*, Phys. Rev. Lett. **74**, 2632 (1995)

[17] F. Abe, et al. (CDF Collaboration), *Observation of top quark production in* $\bar{p}p$ *collisions*, Phys. Rev. Lett. **74**, 2626 (1995)

[18] M. Tanabashi, et al. (Particle Data Group), Phys. Rev. D **98**, 0300001, (2018) and 2019 update

[19] C. Kraus, et al., *Final results from phase II of the Mainz neutrino mass search in tritium beta decay*, Eur. Phys. J. C **40**, 447 (2005)

[20] V. N. Aseev, et al. (Troitsk Collaboration), *An upper limit on electron antineutrino mass from Troitsk experiment*, Phys. Rev. D **84**, 112003 (2011)

[21] N. Cabibbo, *Unitary Symmetry and Leptonic Decays*, Phys. Rev. Lett. **10**, 531 (1963)

[22] M. Kobayashi, T. Maskawa, *CP Violation in the Renormalizable Theory of Weak Interaction*, Prog. Theor. Phys. **49**, 652 (1973)

[23] F. Halzen, A. Martin, *Quarks and Leptons: An introductory course in modern particle physics*, Wiley (1984)

[24] S. W. Herb, et al., *Observation of a Dimuon Resonance at 9.5 GeV in 400 GeV Proton-Nucleus Collisions*, Phys. Rev. Lett. **39**, 252 (1977)

[25] Atlas, Cms, DØ and CDF Collaborations, *First combination of Tevatron and LHC measurements of the top-quark mass*, Technical Report ATLAS-CONF-2014-008. CDF-NOTE-11071. CMS-PAS-TOP-13-014. D0-NOTE-6416, CERN, Geneva (2014), URL `https://cds.cern.ch/record/1669819`

[26] M. Jeżabek, J. Kühn, *QCD corrections to semileptonic decays of heavy quarks*, Nucl. Phys. B **314(1)**, 1 (1989)

[27] Atlas Collaboration, *Direct top-quark decay width measurement in the $t\bar{t}$ lepton+jets channel at $\sqrt{s}$ = 8 TeV with the ATLAS experiment*, Eur. Phys. J. C **78(2)**, 129 (2018)

[28] I. I. Y. Bigi, et al., *Production and decay properties of ultraheavy quarks*, Phys. Lett. B **181**, 157 (1986)

[29] Atlas Collaboration, *Measurement of the top quark charge in pp collisions at $\sqrt{s}$ = 7 TeV with the ATLAS detector*, JHEP **11**, 031 (2013)

[30] R. D. Ball, et al., *Parton distributions from high-precision collider data*, Eur. Phys. J. C **77(10)**, 663 (2017)

[31] J. C. Collins, D. E. Soper, G. F. Sterman, *Factorization of Hard Processes in QCD*, Adv. Ser. Direct. High Energy Phys. **5**, 1 (1989)

[32] T. A. Aaltonen, et al. (CDF and DØ Collaborations), *Tevatron Combination of Single-Top-Quark Cross Sections and Determination of the Magnitude of the Cabibbo-Kobayashi-Maskawa Matrix Element V_{tb}*, Phys. Rev. Lett. **115(15)**, 152003 (2015)

[33] Atlas and Cms Collaborations, *Combination of cross-section measurements for associated production of a single top-quark and a W boson at $\sqrt{s}$ = 8 TeV with the ATLAS and CMS experiments*, Technical Report ATLAS-CONF-2016-023, CERN, Geneva (2016), URL `http://cds.cern.ch/record/2153385`

[34] *LHCTopWG Summary Plots*, URL `https://twiki.cern.ch/twiki/bin/view/LHCPhysics/LHCTopWGSummaryPlots`, as of 21.08.2019

[35] V. M. Abazov, et al. (DØ Collaboration), *$t\bar{t}$ production cross section in $p\bar{p}$ collisions at $\sqrt{s}$ = 1.8 TeV*, Phys. Rev. D **67**, 012004 (2003)

[36] T. Affolder, et al. (CDF Collaboration), *Measurement of the $t\bar{t}$ production cross section in $p\bar{p}$ collisions at $\sqrt{s}$ = 1.8 TeV*, Phys. Rev. D **64**, 032002 (2001)

[37] T. Aaltonen, et al. (CDF and DØ Collaborations), *Combination of measurements of the top-quark pair production cross section from the Tevatron Collider*, Phys. Rev. D **89**, 072001 (2014)

[38] ATLAS and CMS Collaborations, *Combination of ATLAS and CMS top-quark pair cross section measurements using up to 1.1 fb^{-1} of data at 7 TeV*, Technical Report ATLAS-CONF-2012-134, CERN, Geneva (2012), URL `http://cds.cern.ch/record/1478422`

[39] ATLAS Collaboration, *Measurement of the inclusive and fiducial $t\bar{t}$ production cross-sections in the lepton+jets channel in pp collisions at $\sqrt{s}$ = 8 TeV with the ATLAS detector*, Eur. Phys. J. C **78**, 487 (2018)

[40] ATLAS Collaboration, *Measurement of the $t\bar{t}$ production cross-section using $e\mu$ events with b-tagged jets in pp collisions at $\sqrt{s}$ = 7 and 8 TeV with the ATLAS detector*, Eur. Phys. J. C **74(10)**, 3109 (2014)

[41] CMS Collaboration, *Measurement of the $t\bar{t}$ production cross section in the all-jets final state in pp collisions at $\sqrt{s}$ = 8 TeV*, Eur. Phys. J. C **76(3)**, 128 (2016)

[42] ATLAS Collaboration, *Measurement of the $t\bar{t}$ production cross section in the τ+jets final state in pp collisions at $\sqrt{s}$ = 8 TeV using the ATLAS detector*, Phys. Rev. D **95**, 072003 (2017)

[43] ATLAS and CMS Collaborations, *Combination of ATLAS and CMS top quark pair cross section measurements in the $e\mu$ final state using proton-proton collisions at $\sqrt{s}$ = 8 TeV*, Technical Report ATLAS-CONF-2014-054, CERN, Geneva (2014), URL `https://cds.cern.ch/record/1951322`

[44] ATLAS Collaboration, *Measurement of the $t\bar{t}$ production cross-section using $e\mu$ events with b-tagged jets in pp collisions at $\sqrt{s}$ = 13 TeV with the ATLAS detector*, Phys. Lett. B **761**, 136 (2016)

[45] ATLAS Collaboration, *Measurements of the $t\bar{t}$ production cross-section in the dilepton and lepton-plus-jets channels and of the ratio of the $t\bar{t}$ and Z boson cross-sections in pp collisions at $\sqrt{s}$ = 13 TeV with the ATLAS detector*, Technical Report ATLAS-CONF-2015-049, CERN, Geneva (2015), URL `https://cds.cern.ch/record/2052605`

[46] CMS Collaboration, *Measurement of the $t\bar{t}$ production cross section using events in the $e\mu$ final state in pp collisions at $\sqrt{s}$ = 13 TeV*, Eur. Phys. J. C **77**, 172 (2017)

[47] CMS Collaboration, *Measurement of the $t\bar{t}$ production cross section using events with one lepton and at least one jet in pp collisions at $\sqrt{s}$ = 13 TeV*, JHEP **09**, 051 (2017)

[48] M. Beneke, et al., *Hadronic top-quark pair production with NNLL threshold resummation*, Nucl. Phys. B **855**, 695 (2012)

[49] M. Cacciari, et al., *Top-pair production at hadron colliders with next-to-next-to-leading logarithmic soft-gluon resummation*, Phys. Lett. B **710(4)**, 612 (2012)

[50] P. Bärnreuther, M. Czakon, A. Mitov, *Percent Level Precision Physics at the Tevatron: First Genuine NNLO QCD Corrections to $q\bar{q} \to t\bar{t}+X$*, Phys. Rev. Lett. **109**, 132001 (2012)

[51] M. Czakon, A. Mitov, *NNLO corrections to top-pair production at hadron colliders: the all-fermionic scattering channels*, JHEP **12**, 054 (2012)

[52] M. Czakon, A. Mitov, *NNLO corrections to top pair production at hadron colliders: the quark-gluon reaction*, JHEP **01**, 080 (2013)

[53] M. Czakon, P. Fiedler, A. Mitov, *Total Top-Quark Pair-Production Cross Section at Hadron Colliders Through $O(\alpha_s^4)$*, Phys. Rev. Lett. **110**, 252004 (2013)

[54] M. Czakon, A. Mitov, *Top++: A Program for the Calculation of the Top-Pair Cross-Section at Hadron Colliders*, Comput. Phys. Commun. **185**, 2930 (2014)

[55] M. Botje, et al., *The PDF4LHC Working Group Interim Recommendations* (2011), `arXiv:1101.0538 [hep-ph]`

[56] A. D. Martin, et al., *Parton distributions for the LHC*, Eur. Phys. J. C **63**, 189 (2009)

[57] A. D. Martin, et al., *Uncertainties on α_s in global PDF analyses and implications for predicted hadronic cross sections*, Eur. Phys. J. **64(4)**, 653 (2009)

[58] H.-L. Lai, et al., *New parton distributions for collider physics*, Phys. Rev. D **82**, 074024 (2010)

[59] J. Gao, et al., *CT10 next-to-next-to-leading order global analysis of QCD*, Phys. Rev. D **89(3)**, 033009 (2014)

[60] R. D. Ball, et al., *Parton distributions with LHC data*, Nucl. Phys. B **867**, 244 (2013)

[61] O. S. Brüning, et al., *LHC Design Report*, CERN, Geneva (2004), URL `https://cds.cern.ch/record/782076`

[62] Atlas Collaboration, *The ATLAS Experiment at the CERN Large Hadron Collider*, JINST **3**, S08003 (2008)

[63] Cms Collaboration, *The CMS Experiment at the CERN LHC*, JINST **3**, S08004 (2008)

[64] A. A. Alves, Jr., et al. (LHCb Collaboration), *The LHCb Detector at the LHC*, JINST **3**, S08005 (2008)

[65] K. Aamodt, et al. (Alice Collaboration), *The ALICE experiment at the CERN LHC*, JINST **3**, S08002 (2008)

[66] V. Berardi, et al. (TOTEM Collaboration), *Total cross-section, elastic scattering and diffraction dissociation at the Large Hadron Collider at CERN: TOTEM Technical Design Report*, Technical report, Geneva (2004), URL `http://cds.cern.ch/record/704349`

[67] J. Pinfold, et al. (MoEDAL Collaboration), *Technical Design Report of the MoEDAL Experiment*, Technical Report CERN-LHCC-2009-006. MoEDAL-TDR-001 (2009), URL `http://cds.cern.ch/record/1181486`

[68] O. Adriani, et al. (LHCf Collaboration), *Technical design report of the LHCf experiment: Measurement of photons and neutral pions in the very forward region of LHC*, Technical report, Geneva (2006), URL `http://cds.cern.ch/record/926196`

[69] M. Capeans, et al., *ATLAS Insertable B-Layer Technical Design Report*, Technical Report CERN-LHCC-2010-013. ATLAS-TDR-19 (2010), URL `https://cds.cern.ch/record/1291633`

[70] A. Ruiz-Martinez, Atlas Collaboration, *The Run-2 ATLAS Trigger System*, Technical Report ATL-DAQ-PROC-2016-003, CERN, Geneva (2016), URL `https://cds.cern.ch/record/2133909`

[71] Atlas Collaboration, *Electron efficiency measurements with the ATLAS detector using 2012 LHC proton-proton collision data*, Eur. Phys. J. C **77(3)**, 195 (2017)

[72] Atlas Collaboration, *Electron reconstruction and identification in the ATLAS experiment using the 2015 and 2016 LHC proton-proton collision data at* $\sqrt{s} = 13$ *TeV*, Eur. Phys. J. C **79(8)**, 639 (2019)

[73] Atlas Collaboration, *Muon reconstruction performance of the ATLAS detector in proton-proton collision data at* $\sqrt{s} = 13$ *TeV*, Eur. Phys. J. C **76(5)**, 292 (2016)

[74] W. Lampl, et al., *Calorimeter Clustering Algorithms: Description and Performance*, Technical Report ATL-LARG-PUB-2008-002. ATL-COM-LARG-2008-003, CERN, Geneva (2008), URL `http://cds.cern.ch/record/1099735`

[75] M. Cacciari, G. P. Salam, G. Soyez, *The anti-k_t jet clustering algorithm*, JHEP **04**, 063 (2008)

[76] Atlas Collaboration, *Jet energy scale measurements and their systematic uncertainties in proton-proton collisions at $\sqrt{s}$ = 13 TeV with the ATLAS detector*, Phys. Rev. D **96(7)**, 072002 (2017)

[77] Atlas Collaboration, *Performance of pile-up mitigation techniques for jets in pp collisions at $\sqrt{s}$ = 8 TeV using the ATLAS detector*, Eur. Phys. J. C **76(11)**, 581 (2016)

[78] Atlas Collaboration, *Expected performance of the ATLAS b-tagging algorithms in Run-2*, Technical Report ATL-PHYS-PUB-2015-022, CERN, Geneva (2015), URL `https://cds.cern.ch/record/2037697`

[79] Atlas Collaboration, *Performance of missing transverse momentum reconstruction with the ATLAS detector using proton-proton collisions at $\sqrt{s}$ = 13 TeV*, Eur. Phys. J. C **78(11)**, 903 (2018)

[80] D. Adams, et al., *Recommendations of the Physics Objects and Analysis Harmonisation Study Groups 2014*, Technical Report ATL-PHYS-INT-2014-018, CERN, Geneva (2014), URL `https://cds.cern.ch/record/1743654`

[81] T. Gleisberg, et al., *Event generation with SHERPA 1.1*, JHEP **02**, 007 (2009)

[82] D. J. Lange, *The EvtGen particle decay simulation package*, Nucl. Instrum. Meth. A **462**, 152 (2001)

[83] Atlas Collaboration, *The ATLAS Simulation Infrastructure*, Eur. Phys. J. C **70**, 823 (2010)

[84] S. Agostinelli, et al., *GEANT4: A Simulation toolkit*, Nucl. Instrum. Meth. A **506**, 250 (2003)

[85] W. Lukas, *Fast Simulation for ATLAS: Atlfast-II and ISF*, Technical Report ATL-SOFT-PROC-2012-065, CERN, Geneva (2012), URL `http://cds.cern.ch/record/1458503`

[86] T. Sjöstrand, et al., *An Introduction to PYTHIA 8.2*, Comput. Phys. Commun. **191**, 159 (2015)

[87] S. Alioli, et al., *A general framework for implementing NLO calculations in shower Monte Carlo programs: the POWHEG BOX*, JHEP **06**, 043 (2010)

[88] R. D. Ball, et al., *Parton distributions for the LHC Run II*, JHEP **04**, 040 (2015)

[89] Atlas Collaboration, *ATLAS Run 1 Pythia8 tunes*, Technical Report ATL-PHYS-PUB-2014-021, CERN, Geneva (2014), URL `https://cds.cern.ch/record/1966419`

[90] M. Bahr, et al., *Herwig++ Physics and Manual*, Eur. Phys. J. C **58**, 639 (2008)

[91] J. Bellm, et al., *Herwig 7.0/Herwig++ 3.0 release note*, Eur. Phys. J. C **76(4)**, 196 (2016)

[92] E. Re, *Single-top Wt-channel production matched with parton showers using the POWHEG method*, Eur. Phys. J. C **71**, 1547 (2011)

[93] P. Kant, et al., *HatHor for single top-quark production: Updated predictions and uncertainty estimates for single top-quark production in hadronic collisions*, Comput. Phys. Commun. **191**, 74 (2015)

[94] M. Aliev, et al., *HATHOR: HAdronic Top and Heavy quarks crOss section calculatoR*, Comput. Phys. Commun. **182**, 1034 (2011)

[95] N. Kidonakis, *Two-loop soft anomalous dimensions for single top quark associated production with a W^- or H^-*, Phys. Rev. D **82**, 054018 (2010)

[96] K. Melnikov, F. Petriello, *Electroweak gauge boson production at hadron colliders through $O(\alpha_s^2)$*, Phys. Rev. D **74**, 114017 (2006)

[97] J. M. Campbell, R. K. Ellis, *An Update on vector boson pair production at hadron colliders*, Phys. Rev. D **60**, 113006 (1999)

[98] J. Alwall, et al., *The automated computation of tree-level and next-to-leading order differential cross sections, and their matching to parton shower simulations*, JHEP **07**, 079 (2014)

[99] D. de Florian, et al. (LHC Higgs Cross Section Working Group), *Handbook of LHC Higgs Cross Sections: 4. Deciphering the Nature of the Higgs Sector* (2016), `arXiv:1610.07922 [hep-ph]`

[100] V. M. Abazov, et al. (DØ Collaboration), *Measurement of the $t\bar{t}$ production cross section in $p\bar{p}$ collisions at $\sqrt{s}$ = 1.96 TeV using kinematic characteristics of lepton + jets events*, Phys. Rev. D **76**, 092007 (2007)

[101] F. Derue, *Estimation of fake lepton background for top analyses using the Matrix Method with the 2015 dataset at $\sqrt{s}$ = 13 TeV with AnalysisTop-2.3.41*, Technical Report ATL-COM-PHYS-2016-198, CERN, Geneva (2016), URL `https://cds.cern.ch/record/2135116`

[102] G. Avoni, et al., *The new LUCID-2 detector for luminosity measurement and monitoring in ATLAS*, JINST **13(07)**, P07017 (2018)

[103] *AnalysisTop21 software*, URL `https://twiki.cern.ch/twiki/bin/view/AtlasProtected/AnalysisTop21`, as of 27.09.2019

[104] B. Achkar, T. Dado, K. Moor, C. Nellist, A. Quadt, E. Shabalina, *Measurement of the inclusive $t\bar{t}$ production cross section using the full Run 2 data set in the lepton+jets channel at $\sqrt{s}$ = 13 TeV with the ATLAS experiment*, Technical Report ATL-COM-PHYS-2019-306, CERN, Geneva (2019), URL `https://cds.cern.ch/record/2670570`

[105] Atlas Collaboration, *Estimation of non-prompt and fake lepton backgrounds in final states with top quarks produced in proton-proton collisions at $\sqrt{s}$ = 8 TeV with the ATLAS detector*, Technical Report ATLAS-CONF-2014-058, CERN, Geneva (2014), URL `http://cds.cern.ch/record/1951336`

[106] Atlas Collaboration, *Measurements of inclusive and differential fiducial cross-sections of $t\bar{t}$ production with additional heavy-flavour jets in proton-proton collisions at $\sqrt{s}$ = 13 TeV with the ATLAS detector*, JHEP **04**, 046 (2019)

[107] Atlas Collaboration, *Measurements of top-quark pair differential cross-sections in the $e\mu$ channel in pp collisions at $\sqrt{s}$ = 13 TeV using the ATLAS detector*, Eur. Phys. J. C **77(5)**, 292 (2017)

[108] M. Czakon, et al., *Top-pair production at the LHC through NNLO QCD and NLO EW*, JHEP **10**, 186 (2017)

[109] *The TRExFitter package*, URL `https://twiki.cern.ch/twiki/bin/viewauth/AtlasProtected/TtHFitter`, as of 27.09.2019

[110] K. Cranmer, et al. (ROOT Collaboration), *HistFactory: A tool for creating statistical models for use with RooFit and RooStats*, Technical Report CERN-OPEN-2012-016, New York U., New York (2012), URL `https://cds.cern.ch/record/1456844`

[111] F. James, M. Roos, *Minuit: A System for Function Minimization and Analysis of the Parameter Errors and Correlations*, Comput. Phys. Commun. **10**, 343 (1975)

[112] ATLAS Collaboration, *Luminosity determination in pp collisions at $\sqrt{s}$ = 13 TeV using the ATLAS detector at the LHC*, Technical Report ATLAS-CONF-2019-021, CERN, Geneva (2019), URL `http://cds.cern.ch/record/2677054`

[113] Z. Marshall, *Simulation of Pile-up in the ATLAS Experiment*, Technical Report ATL-SOFT-PROC-2013-030, CERN, Geneva (2013), URL `https://cds.cern.ch/record/1616394`

[114] ATLAS Collaboration, *Data-driven determination of the energy scale and resolution of jets reconstructed in the ATLAS calorimeters using dijet and multijet events at $\sqrt{s}$ = 8 TeV*, Technical Report ATLAS-CONF-2015-017, CERN, Geneva (2015), URL `https://cds.cern.ch/record/2008678`

[115] ATLAS Collaboration, *Determination of the jet energy scale and resolution at ATLAS using Z/γ–jet events in data at $\sqrt{s}$ = 8 TeV*, Technical Report ATLAS-CONF-2015-057, CERN, Geneva (2015), URL `https://cds.cern.ch/record/2059846`

[116] ATLAS Collaboration, *Measurements of b-jet tagging efficiency with the ATLAS detector using $t\bar{t}$ events at $\sqrt{s}$ = 13 TeV*, JHEP **08**, 089 (2018)

[117] ATLAS Collaboration, *Measurement of b-tagging Efficiency of c-jets in $t\bar{t}$ Events Using a Likelihood Approach with the ATLAS Detector*, Technical Report ATLAS-CONF-2018-001, CERN, Geneva (2018), URL `https://cds.cern.ch/record/2306649`

[118] ATLAS Collaboration, *Calibration of light-flavour jet b-tagging rates on ATLAS proton-proton collision data at $\sqrt{s}$ = 13 TeV*, Technical Report ATLAS-CONF-2018-006, CERN, Geneva (2018), URL `https://cds.cern.ch/record/2314418`

[119] ATLAS Collaboration, *Electron and photon energy calibration with the ATLAS detector using 2015-2016 LHC proton-proton collision data*, JINST **14(03)**, P03017 (2019)

[120] J. Butterworth, et al., *PDF4LHC recommendations for LHC Run II*, J. Phys. G **43**, 023001 (2016)

[121] S. Frixione, et al., *Single-top hadroproduction in association with a W boson*, JHEP **07**, 029 (2008)

[122] S. Catani, et al., *QCD matrix elements + parton showers*, JHEP **11**, 063 (2001)

[123] R. Barlow, C. Beeston, *Fitting using finite Monte Carlo samples*, Comput. Phys. Commun. **77**, 219 (1993)

[124] U. Langenfeld, S. Moch, P. Uwer, *New results for $t\bar{t}$ production at hadron colliders* (2009), `arXiv:0907.2527[hep-ph]`

[125] CMS Collaboration, *Measurement of the $t\bar{t}$ production cross section, the top quark mass, and the strong coupling constant using dilepton events in pp collisions at $\sqrt{s} = 13$ TeV*, Eur. Phys. J. C **79(5)**, 368 (2019)

[126] ATLAS Collaboration, *Measurement of the $t\bar{t}$ production cross-section and lepton differential distributions in $e\mu$ dilepton events from pp collisions at $\sqrt{s} = 13$ TeV with the ATLAS detector*, Technical Report ATLAS-CONF-2019-041, CERN, Geneva (2019), URL `https://cds.cern.ch/record/2686255`

[127] ATLAS Collaboration, *Measurement of the top quark pair production cross-section with ATLAS in the single lepton channel*, Phys. Lett. B **711**, 244 (2012)

[128] CMS Collaboration, *Measurement of the $t\bar{t}$ production cross section at 13 TeV in the all-jets final state*, Technical Report CMS-PAS-TOP-16-013, CERN, Geneva (2016), URL `https://cds.cern.ch/record/2161138`

[129] M. Cacciari, G. P. Salam, G. Soyez, *The Catchment Area of Jets*, JHEP **04**, 005 (2008)

Acknowledgements

First, I would like to thank Prof. Dr. Arnulf Quadt for supervising this master's thesis and for being the first referee. Especially, I am very grateful for giving me the opportunity to work on a very interesting measurement and to collect lots of experiences in an ATLAS analysis. Unfortunately, there was not enough time to publish the paper but I am very glad that we still managed to finish the ATLAS conference note. Also, I would like to thank Prof. Dr. Ariane Frey for agreeing to be the second referee for this thesis.

I would like to thank Prof. Dr. Baida Achkar and Dr. Clara Nellist for the daily support and the good cooperation. My special thanks goes to Dr. Tomas Dado for providing me with very useful code, for always being available for lots of questions, and for all his great ideas to solve any kind of problem, whether related to physics or technical implementations. I also want to thank Dr. Elizaveta Shabalina for her extensive experience in top-quark physics and all the valuable discussions that helped to finish this analysis. Thanks a lot to Dr. Thomas Peiffer for proofreading this thesis and for all his helpful comments.

Last but not least, I would like to thank my family and friends for all their support during the last years of my studies.

Erklärung nach §17(9) der Prüfungsordnung für den Bachelor-Studiengang Physik und den Master-Studiengang Physik an der Universität Göttingen:

Hiermit erkläre ich, dass ich diese Abschlussarbeit selbständig verfasst habe, keine anderen als die angegebenen Quellen und Hilfsmittel benutzt habe und alle Stellen, die wörtlich oder sinngemäß aus veröffentlichten Schriften entnommen wurden, als solche kenntlich gemacht habe.
Darüberhinaus erkläre ich, dass diese Abschlussarbeit nicht, auch nicht auszugsweise, im Rahmen einer nichtbestandenen Prüfung an dieser oder einer anderen Hochschule eingereicht wurde.
Die digitale Version stimmt mit der schriftlichen überein.

Göttingen, den 18. November 2019

(Kevin Moor)